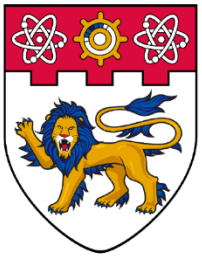

NANYANG TECHNOLOGICAL UNIVERSITY
SINGAPORE

Advancing Optical Coherence Tomography: Improving Measurement Accuracy and Introducing Novel Sensing Applications

Xu Zhengyang

School of Electrical & Electronic Engineering

A thesis submitted to the Nanyang Technological University

in partial fulfilment of the requirement for the degree of

Doctor of Philosophy

2025

Statement of Originality

I hereby certify that the work embodied in this thesis is the result of original research, is free of plagiarised materials, and has not been submitted for a higher degree to any other University or Institution.

23 Jan 2025

. . . . . .
Date

. . . . . .
Xu Zhengyang

Supervisor Declaration Statement

I have reviewed the content and presentation style of this thesis and declare it is free of plagiarism and of sufficient grammatical clarity to be examined. To the best of my knowledge, the research and writing are those of the candidate except as acknowledged in the Author Attribution Statement. I confirm that the investigations were conducted in accord with the ethics policies and integrity standards of Nanyang Technological University and that the research data are presented honestly and without prejudice.

23 Jan 2025

. . . . . .

Date

. . . . . .

Chen Yu-Cheng

Authorship Attribution Statement

This thesis contains material from 3 papers published/to be published in the following peer-reviewed journals where I was the first author.

Chapter 3 is published as Zhengyang Xu, Yukun Wang, Xi Chen, Kan Lin, and Linbo Liu, "Dual beam optical coherence tomography angiography for decoupling axial velocity gradient," Sci Rep, vol. 14, no. 1, p. 19464, Aug. 2024, doi: 10.1038/s41598-024-68924-4.

The contributions of the co-authors are as follows:

- I and Prof. Liu Linbo conceptualize the dual beam system.
- I initiated the project, designed the study, developed the optical imaging system, developed the imaging processing algorithms, conducted the image acquisition, processing and analysis, and wrote the manuscript.
- Lin Kan, Wang Yukun and Chen Xi assisted the hardware and software platform essential for executing the experiment.
- Prof. Liu Linbo revised the manuscript
- Prof. Liu Linbo supervised the overall project

Chapter 4 is published as: **Zhengyang Xu**, Yuting Gao, Xi Chen, Kan Lin, Linbo Liu, and Yu-Cheng Chen, "Axial Super-Resolution in Optical Coherence Tomography Images via Spectrum-Based Self-Supervised Training," *IEEE Trans. Comput. Imaging*, vol. 11, pp. 497–505, 2025, doi: 10.1109/tci.2025.3555134.

The contributions of the co-authors are as follows:

- I conceptualize the spectrum based self-supervised training system, initiated the project, designed the study, developed the optical imaging system, developed the imaging processing algorithms, conducted the

image processing and analysis, and wrote the manuscript.

- I and Gao Yuting conducted the image acquisition.
- Lin Kan and Chen Xi assisted the hardware and software platform essential for executing the experiment.
- Prof. Chen Yu-Cheng revised the manuscript
- Prof. Liu Linbo and Prof. Chen Yu-Cheng supervised the overall project

Chapter 5 is to be submitted for publication to ACS Analytical Chemistry as Zhengyang Xu, Guocheng Fang, Ningyuan Nie, Xi Chen, Kan Lin, Yu-Cheng Chen,

"Liquid Crystal Droplet Patch for Skin PH Sensing by Optical Coherence Tomography,"

The contributions of the co-authors are as follows:

- Fang Guocheng and Prof. Chen Yu-Cheng conceptualize the LC patch for skin pH sensing, I conceptualize the combination of OCT imaging and patch together to achieve the exact sensing.
- I, Fang Guocheng, and Nie Ningyuan designed and conducted the chemical experiments and prepared the necessary materials.
- I initiated the project, designed the study, developed the optical imaging system, developed the imaging processing algorithms, conducted the image acquisition, processing and analysis, and wrote the manuscript.
- Lin Kan and Chen Xi setup the hardware and software platform essential for executing the experiment.
- Prof. Chen Yu-Cheng and Fang Guocheng revised the manuscript
- Prof. Chen Yu-Cheng supervised the overall project

23 Jan 2025

. . . . . .
Date

. . . . . .
Xu Zhengyang

Acknowledgement

First and foremost, I would like to express my deep and heartfelt gratitude to my supervisor, Prof. Chen Yu-Cheng. His guidance and unwavering support have meant the world to me throughout my research journey and my career development. Under his mentorship, I have not only learned how to organize my work and present it with clarity, but I have also discovered new ways of seeing the world, of searching for answers, and of innovating. Prof. Chen has shown me how to believe in myself and to step forward with confidence, always encouraging me to present my best self. His patience, encouragement, and commitment have had a profound impact on my growth; he has been so much more than a supervisor-he has been a true mentor and guide in my life.

Working on Prof. Chen's project was particularly challenging for me, as it introduced elements of chemistry that lay beyond my previous experience. He believed in me when I was uncertain and gave me the courage to face unfamiliar territory. His support helped me accelerate my learning and push past my own limits. He has shown me how to recognize and leverage my strengths, teaching me how to communicate my ideas with confidence. Prof. Chen's support extended beyond my academic work—he has been a steadfast advocate for my career, opening doors to opportunities and offering invaluable advice. His willingness to spend time with me, to offer guidance regardless of his own schedule, has left a lasting mark on my life, and I am deeply, profoundly grateful for his unwavering support.

I would also like to extend my deep and heartfelt gratitude to Prof. Liu Linbo, my first supervisor during the initial steps of my PhD journey. Though he is no longer at NTU, the influence he has had on my life and development as a researcher remains significant. Prof. Liu introduced me to the field of OCT, helping me build a solid foundation and bridging essential gaps in my knowledge of mathematics and physics. As I transitioned directly from a bachelor's degree in Infocom Engineering to the complex field of OCT, Prof. Liu created a thoughtful, gradual path that allowed me to grow at a steady pace. His guidance helped me develop the skills needed to identify research gaps in a mature field where innovation is often a daunting task.

Prof. Liu was patient and understanding as I navigated the steep learning curve, offering space for mistakes and nurturing my growth from a student into an independent researcher. He was always attentive to my progress, providing both encouragement and the challenges I needed to push myself. Despite his busy schedule, he made time to mentor me, offering insights that have not only shaped my research but also my approach to life. His mentorship laid the foundation for my journey as a researcher, and his influence will remain with me always.

My sincere thanks go to my colleagues Fang Guocheng, Nie Ningyuan, Wang Yukun, and Lou Shiliang, who have shared their expertise so generously with me. Whether it was guidance in chemistry, manuscript writing, optical systems, or industry insights, their patience and willingness to teach me have been instrumental in my progress. I am also deeply grateful to Chen Xi, Lin Kan, and Gao Yuting, whose support in project preparation and execution has been invaluable. To my colleagues Tseng Po-Hao, Fu Bowen, Zhou Tian, Wang Weian, Guo Xiaoniu, Sun Xiyu, Zhu Hui, Xiong Zhongshu, Yang Hongjia, and Chen Si, I extend my heartfelt thanks for their constant support and encouragement, which have enriched my journey in so many ways.

I am profoundly grateful to my TAC members, Prof. Wang Qijie and Dr. Hu Juanjuan, for their constant support and encouragement throughout my PhD journey. They have shown genuine concern for my progress, offering invaluable advice at every step. Despite their busy schedules, they have always been generous with their time, treating me with the same care as they would their own students. Their kindness, patience, and guidance have been a source of strength and reassurance, and I am incredibly grateful to them.

To all the colleagues and friends that I have met during my years at NTU, thank you for creating a community filled with warmth, excellence, and inspiration. Together, you have made every day at NTU a joy, filling the campus with energy and spirit that lifted me up in both my work and my life. Your friendship has meant so much to me, and I am grateful for each of you.

Lastly, my deepest and most enduring gratitude is reserved for my family: my wife, my father, my stepmother, my grandparents, and all my loved ones and friends. Your selfless love and unwavering support have been the bedrock of my

life. Throughout my years in Singapore, through every triumph and every challenge, you have been by my side, offering both physical and emotional strength whenever I needed it. You have supported me in ways I can never fully repay, and your presence has been essential to my growth and maturity. I am forever grateful for your unconditional love, and I carry it with me in everything I do. Thank you for being my foundation, my strength, and my greatest source of inspiration.

Table of Contents

Summary

This thesis presents a series of advancements in Optical Coherence Tomography (OCT) technology, addressing challenges in measurement accuracy, resolution enhancement, and expanding OCT's application scope to biochemical monitoring. By developing innovative methodologies and integrating complementary technologies, this work enhances OCT's capabilities, making it a more comprehensive tool for non-invasive biomedical diagnostics.

First, a dual-beam OCT system was developed to improve the accuracy of blood flow velocity measurements in OCT angiography (OCTA) by decoupling axial velocity gradient (AVG) artifacts. which refers to flow velocity variations along the scanning beam's axis, can distort OCTA's decorrelation signals, leading to inaccuracies in blood flow measurements. Our dual-beam OCT system introduced in this thesis uses commercially available, low-cost components and only requires two simultaneous scan sessions, making it faster and less vulnerable to subject motion compared to methods that require multiple scans. Validation experiments with phantoms and in-vivo imaging of human skin vasculature demonstrated significant reductions in AVG-related artifacts, thus enhancing measurement reliability and enabling more precise blood flow analysis in clinical applications.

Second, this thesis introduces a self-supervised deep learning framework for enhancing OCT's axial resolution, critical for diagnostic accuracy. Traditional high-resolution OCT imaging requires broader spectral bandwidths, which are expensive and technically challenging. Existing image-based deep learning method fails to recover detail continuity. Our proposed spectrum-based deep learning approach leverages OCT's raw spectral data, including phase information, rather than intensity-only images. By training directly on the spectral data, this approach achieves super-resolution without needing reference high-resolution images, improving axial resolution by 50% and yielding substantial gains in Peak Signal-to-Noise Ratio (PSNR) and Structural Similarity Index Measure (SSIM) metrics. This resolution enhancement is especially valuable for visualizing fine boundary structures, such as those between the stratum corneum and stratum lucidum in skin imaging. Beyond dermatology, this

method shows potential for OCT imaging in retinal diagnostics, aiding in the early detection of conditions like age-related macular degeneration and diabetic retinopathy by resolving finer details within retinal layers and microvascular structures.

Finally, the thesis explores a novel application of OCT by integrating it with a sensing patch to enable real-time biochemical monitoring and structural imaging simultaneously. This system combines OCT's high-resolution structural imaging with the biochemical sensitivity of the sensors in patch, e.g. Liquid Crystals (LCs), which respond dynamically to changes in their environment. In this setup, LC droplets within the hydrogel patch act as pH sensors, changing their orientation and optical properties in response to pH shifts. OCT captures these changes as variations in the droplet imaging size, providing real-time insights into skin pH levels. Validated across a physiological pH range, this dual-function system allows OCT to capture both structural and biochemical data, enhancing its utility for comprehensive skin health assessment. This integration expands OCT's capabilities beyond structural diagnostics, opening new possibilities for wearable, real-time biochemical monitoring of other biomarkers, including glucose and proteins, which are relevant to broader biomedical applications.

In conclusion, this thesis contributes significantly to OCT's evolution as a versatile diagnostic tool by addressing key limitations in measurement accuracy, resolution, and biochemical monitoring. The developed dual-beam system for AVG decoupling, spectrum-based super-resolution framework, and OCT biochemical sensing system represent innovative solutions to longstanding challenges in OCT and OCTA. Collectively, these advancements enhance OCT's precision, versatility, and clinical relevance, positioning it as a powerful tool for high-precision, non-invasive diagnostics in both clinical and research settings.

Table of Figures

List of Tables

Chapter 1. : Introduction

1.1 Motivation

Optical Coherence Tomography (OCT) is a non-invasive, non-contact, label-free imaging modality that provides three-dimensional and real-time visualization of biological tissue. OCT has become the gold standard in ophthalmology for examining retinal layers and assessing microvascular structures. A functional extension, OCT Angiography (OCTA), enables high-contrast visualization of blood flow and microvasculature by analysing decorrelation between successive B-scans at the same location [1] [2] [3]. These techniques have been widely adopted for screening, diagnosis, and treatment monitoring of ocular and other tissue-related diseases.

Despite the success of OCT and OCTA, several challenges remain—particularly in measurement accuracy, resolution, and the limited scope of applications. With growing interest in wearable sensing and biochemical monitoring, OCT systems face the opportunity to evolve from purely structural imaging tools to multifunctional diagnostic platforms. This thesis addresses three critical directions to enhance OCT capabilities: improving blood flow measurement accuracy, enhancing axial resolution, and enabling biochemical sensing.

1.1.1 Improving Flow Measurement Accuracy via AVG Decoupling

One major limitation in OCTA blood flow quantification is the presence of axial velocity gradient (AVG) artifacts. AVG refers to variations in flow velocity along the axial direction that contribute to decorrelation signals, introducing ambiguity in flow measurement. Existing solutions either require numerous additional acquisitions that hinder in-vivo imaging (e.g., scan-bias techniques), or depend on custom components such as few-mode fibre couplers employing higher-mode point spread function and dark-field detection, whose feasibility for in-vivo applications remains uncertain.This thesis presents a cost-effective alternative using a dual-beam OCT configuration to decouple the AVG component directly for in-vivo imaging. By comparing decorrelation from two incident angles, this system allows a direct and low-cost extraction of true flow velocity, improving measurement accuracy without requiring complex instrumentation.

1.1.2 Enhancing Axial Resolution via Self-Supervised Deep Learning

OCT’s axial resolution is fundamentally constrained by the light source’s bandwidth. Higher

resolutions demand broader bandwidths, which are expensive and technically challenging to achieve. Deep learning offers a promising data-driven alternative. However, conventional image-based super-resolution models often fail to recover meaningful structural details. This study develops a self-supervised deep learning framework that trains directly on spectral data, enabling the enhancement of axial resolution without requiring paired high-resolution ground truths (GT). The model iteratively restores fine structural details, offering a scalable and hardware-independent pathway to high-resolution OCT imaging.

1.1.3 Extending OCT Functionality for Biochemical Sensing

OCT has traditionally been limited to structural imaging. Meanwhile, recent advances in wearable hydrogel patches have introduced real-time biochemical monitoring capabilities. These patches detect pH, glucose, or lactate levels via interactions with sweat, providing vital information for managing inflammation, infection, or skin health. However, integrating such biochemical sensing into OCT systems remains largely unexplored.

This thesis presents a novel biosensing approach by integrating a liquid crystal (LC)-based hydrogel patch with OCT. LC droplets embedded within the patch reorient in response to, e.g. pH changes. These changes manifest as measurable differences in droplet appearance in OCT images. By leveraging this polarization-sensitive property, the system enables simultaneous structural imaging and biochemical monitoring of the skin.

1.2 Objective

The primary objectives of this thesis are:

a) Develop and validate a dual-beam OCT system that enables more accurate blood flow quantification by decoupling AVG artifacts.
b) Enhance OCT axial resolution through a self-supervised deep learning framework based on spectral domain training.
c) Demonstrate the integration of OCT with an LC-based hydrogel patch for biochemical informaiont, e.g. pH, sensing and establish its feasibility for multimodal diagnostics.

1.3 Significance and Novelty

This thesis introduces novel approaches to improve OCT accuracy, resolution, and functionality, addressing key limitations in current OCT applications:

a) **Faster and more cost-Effective AVG Decoupling:** The dual-beam OCT system mitigates the effect of AVG on flow velocity with a single round of OCTA image acquisition. This approach introduces less scans compared to the scan-bias method, which requires multiple scans to accurately fit the non-linear curve. Compared with few-mode fibre coupler method which requires lab-made key component, it leverages off-the-shelf components to provide an affordable solution for decoupling AVG artifacts in OCTA. This approach reduces flow measurement uncertainty, achieving a 0.7% error in phantom studies and demonstrating reliable results in in-vivo human skin testing.
b) **Deep Learning for Super-Resolution:** By implementing a self-supervised deep learning framework that directly utilizes spectral data, this study offers a method for achieving high axial resolution in OCT images without costly hardware. This technique enhances OCT images by recovering finer structural details, such as boundary continuity, and results in significant improvements in peak signal-to-noise ratio (PSNR) and structural similarity index (SSIM).
c) **OCT with Biochemical Sensing Capability**: This study demonstrates the expanded capabilities of OCT by integrating it with a hydrogel patch for simultaneous structural and biochemical information sensing. Using an LC as a sensor embedded in the patch, this approach highlights OCT's ability to capture dynamic biochemical changes, such as pH variations, through structural alterations in the images. Validated across a physiological pH range of 6.0 to 8.0, this integration underscores OCT's potential to go beyond traditional structural imaging, enabling versatile, non-invasive assessments of both physical and chemical properties in skin health applications.

Through these innovations, this thesis significantly expands the scope of OCT in clinical diagnostics. By addressing challenges in measurement accuracy, resolution enhancement, and biochemical monitoring, these advancements position OCT as a comprehensive tool for high-precision, non-invasive diagnostics, applicable to a wide range of biomedical fields beyond its traditional role in ophthalmology.

1.4 Chapter Outline

The remainder of this thesis is structured as follows:

a) Chapter 2 provides essential background on OCT, OCTA, and relevant theories in optics and machine learning that support the proposed methodologies.
b) Chapter 3 introduces the dual-beam OCTA system for accurate AVG decoupling and

presents its validation.

c) Chapter 4 describes the development of a self-supervised deep learning framework to enhance OCT axial resolution using spectral-domain training.
d) Chapter 5 demonstrates the integration of OCT with a pH-responsive hydrogel patch containing liquid crystal droplets for real-time biochemical sensing.
e) Finally, Chapter 6 summarizes the key findings, highlights the contributions, and outlines future research directions.

Chapter 2. : Background Theories

2.1 OCT Fundamentals

2.1.1 OCT and Parameters

OCT is a non-invasive imaging technique based on low-coherence interferometry. It provides high-resolution, depth-resolved images by detecting interference between backscattered light from tissue and a reference beam. The axial resolution is determined by the coherence length of the light source, which is inversely related to its spectral bandwidth. Other key parameters include lateral resolution, imaging depth, and signal-to-noise ratio (SNR).

OCT has become a vital tool in biomedical research and clinical practice, particularly in ophthalmology. It enables real-time cross-sectional imaging without the need for tissue excision or processing, unlike conventional histopathology [4], [5]. This makes OCT highly valuable in scenarios where biopsy is impractical or risky (e.g., eye, arterial, or nerve diseases), where sampling errors are common but diagnostic accuracy is critical (e.g., gastrointestinal lesions), and where longitudinal monitoring is needed (e.g., retinal neovascularization, corneal transplantation).

OCT systems typically use a Michelson interferometer configuration, where light is split into sample and reference arms. Interference occurs only when the optical path lengths match within the coherence length, allowing depth-resolved imaging. Unlike classical laser interferometry with monochromatic light (long coherence length), OCT employs a broadband light source to achieve short coherence length and precise axial sectioning

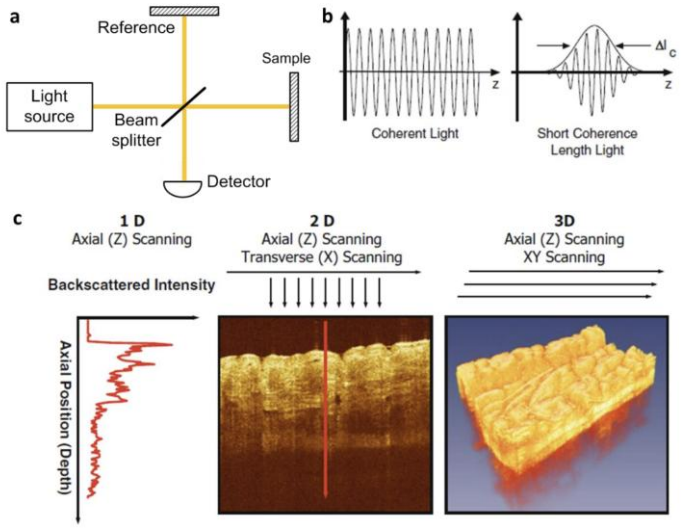

Figure 2-1. The operational principles of OCT include the following: (a) A diagram illustrating the Michelson interferometer setup used in OCT imaging. (b) A narrowband light source exhibits a longer coherence length (left), while a broadband light source results in a shorter coherence length (right). (c) The process of producing an axial scan (left), a cross-sectional image (centre), and a 3D volumetric data set (right). (This figure is adapted from reference [5]).

Interference signals from different back-scattered surfaces along the depth contribute to an axial scan, or A-scan (Figure 2-1 (c); left). By scanning the incident optical beam transversely and performing sequential analyses of A-scans, a two-dimensional, cross-sectional image can be achieved (Figure 2-1 (c); middle). When the incident optical beam is scanned in a two-dimensional pattern, sequential cross-sectional images (B-scans) are generated, and a three-dimensional volumetric dataset can be acquired through reconstruction (Figure 2-1 (c); right).

As an optical microscopy technique, the lateral resolution of an OCT system is determined by the diffraction-limited spot size of the focused optical beam. The parameters characterizing these diffraction-limited quantities, including depth of field (DOF), axial resolution, and lateral field of view (FOV), are summarized in Figure 2-2.

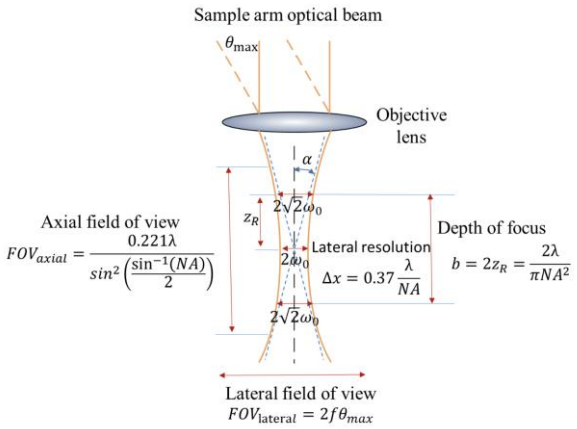

Figure 2-2. Illustration of confocal parameters in the OCT sample arm optics: The objective lens has a focal length f, and the numerical aperture (NA) indicates the effective focusing capability of the optics in the sample arm. The central wavelength of the light source spectrum is λ. The beam radius $\omega(z)$ represents the distance where the intensity falls to $1/e^2$ of its peak value along the axis. At the focus, the beam radius is ω_0, referred to as the beam waist. The Rayleigh range (z_R) is the distance from the beam waist to the point where the beam radius increases to $\sqrt{2}$ times its value at the focus ($\omega(z_R) = \sqrt{2}(\omega_0)$) and corresponds to the minimum curvature radius of the wavefront. (This figure is adapted from reference [5]).

OCT employs light sources with Gaussian-shaped spectra. The field distribution of the Gaussian beam along the propagation direction (z direction) can be expressed as:

$$E = \frac{c}{\omega(z)} \exp\left[-\frac{r^2}{\omega^2(z)}\right] \exp\left[-i\left[k\left(z + \frac{r^2}{2R(z)}\right) + \Phi(z)\right]\right]. \quad (2\text{-}1)$$

Here, c is a constant, r is the radical distance from the center axis, $R(z)$ is the radius of the curvature of the beam's wavefront, $\Phi(z)$ is the Gouy phase, $\omega(z) = \omega_0\sqrt{1 + \left(\frac{\lambda z}{\pi\omega_0^2}\right)^2}$ is the radius corresponding to the distance between the beam axis and the "edge" which is defined as when the amplitude falls to $1 / e$ of its on-axis value (or intensity drops to $1/e^2$ of its on-axis value). ω_0 is the radius of the beam at the focus ($z = 0$) which is termed as the "beam waist". The value of ω_0 could be achieved by deducing the asymptote of the beam edge so that $NA \approx \tan\alpha = \lim_{z\to\infty} \frac{d\omega(z)}{dz}$ and thus $\omega_0 \approx \frac{\lambda}{\pi NA}$. Here, λ is the centre wavelength of the light source; NA is the numerical aperture of the objective lens or, correctly, the effective numerical aperture of the focusing optics in the sample arm.

For each z position, the lateral PSF could be expressed using general Gaussian function $f(x) = a \cdot e^{-\frac{(x-b)^2}{2c^2}}$ with full width at half maximum (FWMH) $= 2\sqrt{2\ln 2}\, c$. Given the width at the $1/e^2$ of the peak power of the PSF being $2\omega_0$ at the focus, the lateral resolution which is defined as the FWHM power of the lateral PSF at the focus position could be achieved:

$$\Delta x = \sqrt{2\ln 2}\,\omega_0 = 0.37\frac{\lambda}{NA}. \quad (2\text{-}2)$$

The expression of $z_R = \frac{\pi}{\lambda}\omega_0^2$ is derived according to $\omega(z_R) = \sqrt{2}\omega_0$ and we define $2z_R$ as the DOF b:

$$b = 2z_R = 2\frac{\pi}{\lambda}\omega_0^2 = \frac{2\lambda}{\pi NA^2} \quad (2\text{-}3)$$

As revealed by Eq. (2-2), finer lateral resolution can be achieved by using an objective lens with a higher NA. However, since NA also determines the DOF b as shown in Eq. (2-3), a high NA will increase the lateral resolution but decrease the DOF (or depth of focus), resulting in a trade-off between these two parameters. This trade-off is clearly illustrated in Figure 2-3: using a high NA objective lens can achieve fine lateral resolution but at the expense of depth of focus.

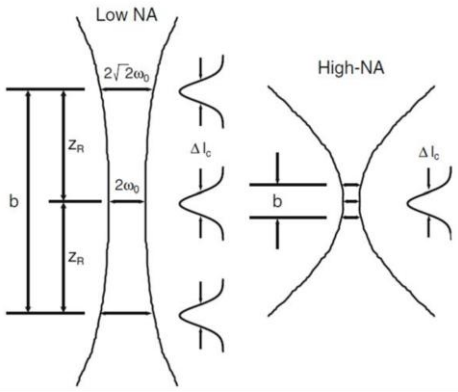

Figure 2-3. The lateral resolution and focus depth in OCT are influenced by the Gaussian beam optics at the focal point, with lateral resolution defined by the FWHM of the lateral PSF. Key parameters include the NA of the optics, the beam waist (ω_0), the Rayleigh range (z_R), and the DOF (b). The axial resolution, determined by the coherence length (Δl_c) of the light source, is calculated at the FWHM of the axial PSF for each reflector. (This figure is adapted from reference [5]).

The axial FOV (FOV_{axial}) of an OCT system is defined as the FWHM power of the confocal axial response function that the intensity drops to one-half of the peak value at the focus (Figure 2-2):

$$FOV_{axial} = \frac{0.221}{\sin^2\left(\frac{\alpha}{2}\right)} = \frac{0.221\lambda}{\sin^2\left(\frac{\sin^{-1}(NA)}{2}\right)}. \quad (2\text{-}4)$$

The lateral FOV ($FOV_{lateral}$) depends on the lateral scanning system. If the input sample arm beam is rotated by the scanning components i.e. galvo scanner to a maximum one-side scan angle θ_{max} in a lateral dimension as illustrated in Figure 2-2, the lateral FOV is given by:

$$FOV_{lateral} = 2f\theta_{max}. \quad (2\text{-}5)$$

In contrast to traditional optical microscopy, the axial resolution of the OCT system is independent of diffraction-limited spot size of the focused optical beam but is determined by the coherence length of the light source.

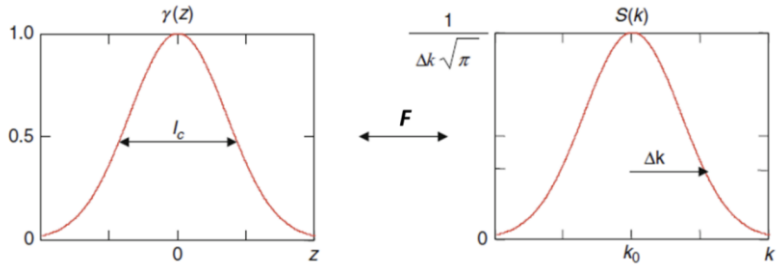

Figure 2-4. Fourier transform of a Gaussian-shaped "coherence function" (left) and the spectrum of the light source (right). l_c indicates the coherence length at the FWHM value, while Δk represents the spectral bandwidth's half-width at $1/e$ of its peak. F denotes the Fourier transform operation. (This figure is adapted from reference [5]).

OCT normally uses Gaussian-shaped spectrum light source with low-coherence length to perform "optical sectioning". We here assume the light source has a centre wavelength of λ and a wavelength bandwidth at the FWHM of its wavelength spectrum of $\Delta\lambda$. As illustrated in Figure 2-4, the corresponding Gaussian function of spectrum $S(k)$ and its Fourier transform "coherence function" $\gamma(z)$ is given by:

$$\gamma(z) = e^{-z^2\Delta k^2} \overset{F}{\leftrightarrow} S(k) = \frac{1}{\Delta k\sqrt{\pi}} e^{-\frac{(k-k_0)^2}{\Delta k^2}}. \qquad (2\text{-}6)$$

Here, F represents Fourier transform operation. The coherence length at the FWHM $l_c = \frac{2\sqrt{\ln 2}}{\Delta k}$ could be achieved from the "coherence function" $\gamma(z)$. Note $\Delta\lambda$ represents wavelength bandwidth at the FWHM of the wavelength spectrum but Δk is defined as the half-width of the spectral bandwidth at $1/e$ of its maximum here, therefore, $\Delta k = \frac{\pi}{\sqrt{\ln 2}}\frac{\Delta\lambda}{\lambda^2}$ according to the Gaussian-shaped spectrum $S(k)$. The axial resolution defined as the coherence length at the FWHM power of the axial PSF could therefore be expressed as:

$$\Delta z = \frac{2\ln 2}{\pi}\frac{\lambda^2}{\Delta\lambda}, \qquad (2\text{-}7)$$

where λ is the center wavelength of the light source, and $\Delta\lambda$ is the FWHM bandwidth of the power spectrum. Clearly shown in Figure 2-5, higher axial resolution could be achieved using light source with shorter centre wavelength and broader bandwidth light.

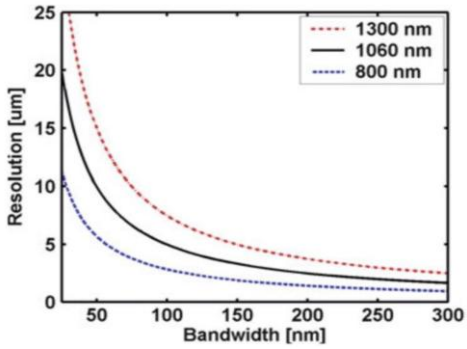

Figure 2-5. Axial resolution in OCT imaging. The relationship between axial resolution and the light source bandwidth for centre wavelengths of 800 nm, 1060 nm, and 1300 nm. (This figure is adapted from reference

[5]).

Since all experiments in this thesis utilize spectral-domain OCT (SD-OCT), the next chapter introduces the principles and key components of SD-OCT systems.

2.1.2 Working principle of Spectral Domain -OCT

Over the past decades, OCT has evolved from time-domain OCT (TD-OCT) to Fourier domain OCT (FD-OCT), which can be subdivided into SD-OCT and swept source OCT (SS-OCT), offering advances in imaging speed and sensitivity. Unlike TD-OCT, which uses an interferometer with a scanning reference arm, time-efficient SD-OCT employs an interferometer with a fixed reference arm approximately aligned with the sample arm (Figure 2-6 (a)) [1] [4] [6] [7].The spectral interference fringes are detected either in parallel (SD-OCT) or in a time-lapse manner (SS-OCT), with frequencies proportional to the optical path delay between the reference and sample reflectors (Figure 2-6 (b)). Different optical echo delays (path length differences ΔL) produce different frequency modulations (Figure 2-6 (b)), and by Fourier transforming the spectral interference signal, the echo delays can be measured (Figure 2-6 (c)).In the detection arm, a spectrometer disperses the spectral interference pattern, allowing the interference spectrum to be detected by an array detector, such as a charge-coupled detector (CCD), as a function of wavelength [4] [6] [8]. By rescaling the spectrometer output from wavelength to frequency ($k = \frac{2\pi}{\lambda}$) and using an inverse Fourier transform, an axial scan that includes the entire depth-resolved microstructures of the sample can be recovered. In summary, SD-OCT measures the cross-spectral density using a spectrometer at the output of the detection arm of the interferometer, eliminating the need for mechanical modulation of the reference arm path length as in TD-OCT, thus enabling faster image acquisition rates. In next session the analytical model of the signal is introduced.

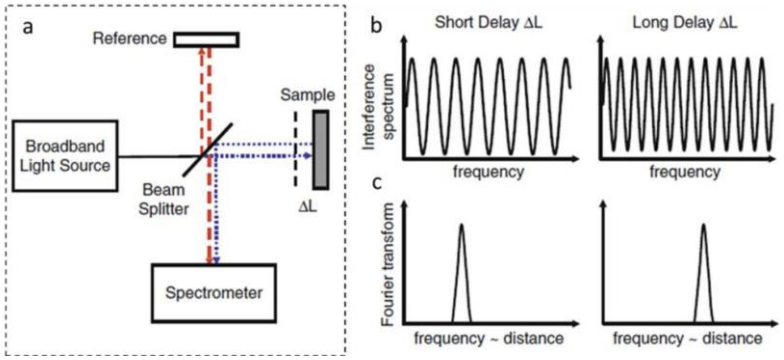

Figure 2-6 Spectral domain OCT. (a) SD-OCT employs an interferometer with a broadband light source and a stationary reference arm. A spectrometer captures the interference pattern formed by light reflected from the

reference mirror and various sample depths. (b) Optical echo delays between the two arms cause variations in frequency modulation. (c) Applying a Fourier transform to the interference spectrum provides depth information for an axial-scan. (This figure is adapted from reference [5]).

2.1.3 Theory of Spectral Low Coherence Interferometry

In OCT, the interferometer could be illuminated by a polychromatic (broad bandwidth) plane wave whose electric field could be expressed as $E_0 = s(k,\omega)e^{i(kz-\omega t)}$, where $s(k,\omega)$ is the electric field amplitude as a function of k and ω. Here, $k = \frac{2\pi}{\lambda}$ and $\omega = \frac{2\pi}{T}$ is the spatial and temporal angular frequency of each spectral component of the electric field, respectively.

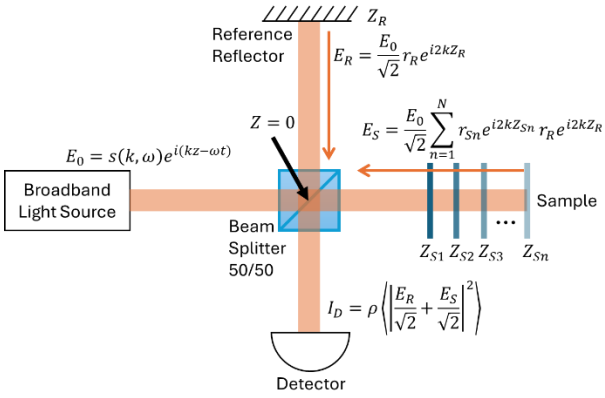

Figure 2-7 Diagram of a low-coherence interferometer utilized in SD-OCT.

As presented in Figure 2-7, we assume that the beam splitter has a wavelength-independent power splitting ratio of 0.5 (50/50). The distance between the beam splitter and the reference reflector is defined as z_R. Assuming the reference path is in air and the reference reflector have an electric field reflectivity of r_R, the field of the light incident on the beam splitter after back-reflected by the reference mirror is given by $E_R = \frac{E_0}{\sqrt{2}} r_R e^{i2kz_R}$.

Divided by the beam splitter, the other part of the incidence light propagates to the sample. For illustrative purposes, we assume a series of discrete reflectors along the depth of the sample, each with an electric field reflectivity of r_{S1}, r_{S2}, r_{S3} … and optical path length from the 50/50 beam splitter of z_{S1}, z_{S2}, z_{S3} … z_{Sn}. The field incident on the beam splitter after back-reflected/backscattered from all depths of reflectors in the sample arm is given by $E_S = \frac{E_0}{\sqrt{2}} \sum_1^N r_{Sn} e^{i2kz_{Sn}}$.

The power from both the reference arm and the sample arm is halved upon passing through the 50/50 beam splitter again and the interference signal detected at the detector is given by $I_D =$

$\rho\langle\left|\frac{E_R}{\sqrt{2}}+\frac{E_S}{\sqrt{2}}\right|^2\rangle=\frac{\rho}{2}\langle\left|(E_R+E_S)\overline{(E_R+E_S)}\right|\rangle$. Here, ρ is the responsivity of the detector, the angular brackets denote the integration over the response time of the detector, and $\overline{(E_R+E_S)}=\overline{E_R}+\overline{E_S}$ which is one of the properties of complex conjugate.

When the centre of the beam splitter is set as $z=0$, the intensity at the detector could be expressed as:

$$I_D(k,\omega)=\frac{\rho}{4}\langle\left|s(k,\omega)\tau_R e^{i(2kz_R-\omega t)}+s(k,\omega)\sum_{n=1}^{N}r_{Sn}e^{i(2kz_{Sn}-\omega t)}\right|^2\rangle. \quad (2\text{-}8)$$

Since the temporal frequency of the light wave $\mathcal{V}$ oscillates much faster than detector's response time, it is reasonable to eliminate the terms dependent on ω (where $\omega=2\pi\mathcal{V}$). Thereafter, a real result for the detector current, commonly known as "spectral interferogram", could be generated as follows:

$$\begin{aligned} I_D(k)=&\frac{\rho}{4}[S(k)(R_R+R_{S1}+E_{S2}+\cdots+R_{Sn})]\ \text{'DC term'}\\ &+\frac{\rho}{2}\left[S(k)\sum_{n=1}^{N}\sqrt{R_R R_{Sn}}\cos[2k(z_R-z_{Sn})]\right]\ \text{'Cross-correlation terms'}\\ &+\frac{\rho}{4}\left[S(k)\sum_{n\neq m=1}^{N}\sqrt{R_{Sn}\,R_{Sm}}\cos[2k(z_{Sn}-z_{Sm})]\right]\ \text{'Auto-correlation terms'} \end{aligned} \quad (2\text{-}9)$$

where $S(k)=\langle|s(k,\omega)|^2\rangle$ denotes the power spectrum depending on the light source, and $R_R=|r_R|^2$ and $R_{Sn}=|r_{Sn}|^2$ denote the power reflectivity of the reference reflector and sample reflectors, respectively. In Eq. (2-9), three distinct components are included:

(1) The "DC" component: This is a path-length independent offset to the detector current. It depends on the wave number spectrum of the light source, with an amplitude proportional to the summation of the power reflectivity of the reflectors at the reference arm and sample arm.

(2) The "cross-correlation" component: This component, desired for OCT imaging, is scaled by both the wave number spectrum $S(k)$ of the light source and the optical path length difference between the reference reflector and the sample reflectors $[(z_R-z_S)]$. The amplitude is determined by $\sqrt{R_R R_{Sn}}$, proportional to the square root of the reflectivity of the sample reflectors.

(3) An "auto-correlation" component: This component indicates the interference that occurs between sample reflectors, appearing as artifacts in typical OCT imaging systems. It depends on the reflectivity of the sample reflectors.

Beyond these intuitive understandings of intensity in OCT imaging, it is also useful to understand the effect of different source spectra and sample reflectors. Firstly, if there is a single sample reflector, the intensity is given by: $I_D(k) = \frac{\rho}{4}S(k)\left[(R_R + R_S) + 2\sqrt{R_R R_S}\cos[2k(z_R - z_S)]\right]$, which includes only the DC term and a single interferometric component. The light source spectrum $S(k)$ is modulated by one cosine function whose frequency is inversely related to the distance between the reference reflector and the sample reflector, as illustrated in Figure 2-8. Additionally, the amplitude $\sqrt{R_R R_{Sn}}$ of the "modulated" spectrum (or the visibility of the spectral fringes) is determined by the reflectivity of the sample reflector $\sqrt{R_{Sn}}$ (Figure 2-8).

In the case of multiple reflectors, which is the real-world condition in OCT imaging, the spectrum is modulated by multiple cosine functions. Each modulated spectrum has a period and an amplitude feature given by the corresponding sample reflector (Figure 2-8). Additionally, for multiple reflectors, the autocorrelation component appears, with frequency modulated by the optical delay between sample reflectors and amplitude determined by $\sqrt{R_{Sn}R_{Sm}}$. Since the sample reflectivity is usually much smaller relative to the reference reflection, the autocorrelation component is typically smaller compared to the cross-correlation component. Furthermore, as sample reflectors tend to be closely clustered relative to the distance between the sample reflector and the reference reflector, the modulation frequency of the auto-correlation term tends to be quite small.

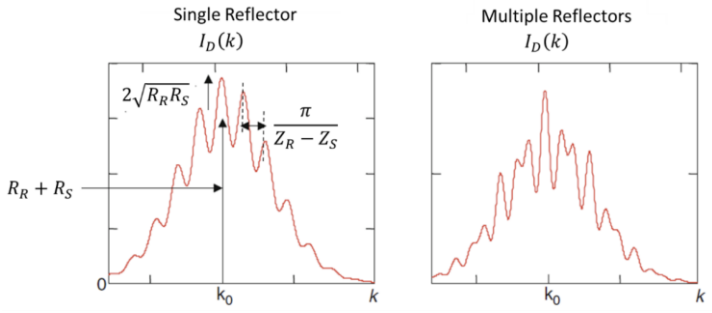

Figure 2-8. Key characteristics of the spectral interferogram in OCT. For a single sample reflector (left), the intensity is given by $I_D(k) = \frac{\rho}{4}S(k)\left[(R_R + R_S) + 2\sqrt{R_R R_S}\cos[2k(z_R - z_S)]\right]$*.. The DC term has an amplitude of* $(R_R + R_S)$*, while the cross-correlation term has an amplitude of* $2\sqrt{R_R R_S}$ *and a wave number period of* $\frac{\pi}{z_R - z_S}$ *superimposed on the DC term (factors of* $\frac{\rho}{4}S(k)$ *are omitted for simplicity). For multiple reflectors (right), the cross-correlation terms form a superposition of all cosinusoids. (This figure is adapted from reference [5]).*

In SD-OCT, all spectral components of the wave-number-dependent detector current ($I_D(k)$) are dispersed by a grating, captured by an array detector at the output of the spectrometer and finally processed using Fourier analysis. This allows for the approximation and reconstruction of the internal sample reflectivity profile $\sqrt{R_S(z_S)}$, which is the aim of low-coherence interferometry. Note that dispersing $I_D(k)$ by wavenumber and its capturing depend on the experimental details of the grating and the detection apparatus, respectively.

Using the property of Fourier transform pair $\frac{1}{2}[\delta(z+z_0)+\delta(z-z_0)] \overset{F}{\leftrightarrow} \cos kz_0$ and the convolution property of Fourier transform $x(z) \otimes y(z) \overset{F}{\leftrightarrow} X(k)Y(k)$, the inverse Fourier transform of Eq. (2-9) in section 2.1.3 could be given as:

$$\begin{aligned} i_D(z) &= \tfrac{\rho}{8}[\gamma(z)(R_R + R_{S1} + R_{S2} + \cdots + R_{Sn})] \text{ 'DC term'} \\ &+ \tfrac{\rho}{4}\left[\gamma(z) \otimes \textstyle\sum_{n=1}^{N} \sqrt{R_R R_{Sn}}\,\delta[z \pm 2(z_R - z_{Sn})]\right] \text{ 'Cross-correlation term'} \\ &+ \tfrac{\rho}{8}\left[\gamma(z) \otimes \textstyle\sum_{n\neq m=1}^{N} \sqrt{R_{Sn} R_{Sm}}\,\delta[z \pm 2(z_{Sn} - z_{Sm})]\right] \text{ 'Autocorrelation term'.} \end{aligned} \qquad (2\text{-}10)$$

Here, $\gamma(z)$ is obtained by the Fourier transform of the spectrum $S(k)$, called the "coherence function," which dominates the axial PSF for each reflector in the OCT system. The Fourier transform between the light source spectrum $S(k)$ and the "coherence function" $\gamma(z)$ has been illustrated in the discussion of OCT axial resolution under Section 2.1. Clearly, the acquired sample field reflectivity profile is embedded within the cross-correlation term of Eq. (2-10):

$$\sqrt{R_S(z_S)} = \textstyle\sum_{n=1}^{N} \sqrt{R_{Sn}}\,\delta[z_S - z_{Sn}]. \qquad (2\text{-}11)$$

If we carry out the convolutions by making use of the sifting property of the delta function, interferometric measurement, regarded as the "axial-scan" or "A-scan," can be obtained:

$$\begin{aligned} i_D(z) &= \frac{\rho}{8}[\gamma(z)(R_R + R_{S1} + R_{S2} + \cdots + R_{Sn})] \\ &+ \frac{\rho}{4}\sum_{n=1}^{N} \sqrt{R_R R_{Sn}}\left[\gamma\big(2(z_R - z_{Sn})\big) + \gamma\big(-2(z_R - z_{Sn})\big)\right] \\ &+ \tfrac{\rho}{8}\textstyle\sum_{n\neq m=1}^{N} \sqrt{R_{Sn} R_{Sm}}\left[\gamma\big(2(z_R - z_{Sn})\big) + \gamma\big(-2(z_R - z_{Sn})\big)\right]. \end{aligned} \qquad (2\text{-}12)$$

The results for discrete sample reflectors and the "A-scan" with a Gaussian-shaped light spectrum are illustrated in Figure 2-9. As shown in the figure, the sample field reflectivity

profile $\sqrt{R_S(z_S)}$ can be restored in the cross-correlation terms with the following modifications:

(1) The sample reflectivity profile $\sqrt{R_S(z_S)}$ is a function of the reference coordinate z_R instead of the sample coordinate z_S; the zero position corresponds to the distance equal to reference arm reflector.

(2) The apparent displacement of each sample reflector from the reference reflector is doubled, meaning the interferometer measures a round-trip distance to each reflector. Thus, a new single-pass depth variable is defined ($\hat{z} = 2z$) to rescale axial depth to account for the factor of 2.

(3) Each sample reflector appears blurred to a width of a coherence length by convoluting with the function $\gamma(z)$. Using a light source with as broad a bandwidth as possible (low coherence length) increases the fidelity of the sample reflector profile.

(4) The detected sample reflectivity is usually very small but amplified by the homodyne gain factor represented by the strong reference reflectivity.

In conclusion, these modifications can be dealt with by properly interpreting the data. Additionally, artifacts such as mirror-image artifacts arising from the cross-correlation terms and artifacts arising from the DC terms and the autocorrelation terms also modify the field reflectivity profile and are generally more significant. Approaches have been developed to eliminate these artifacts. In next two sessions, the metrics to evaluate the OCT signal are introduced.

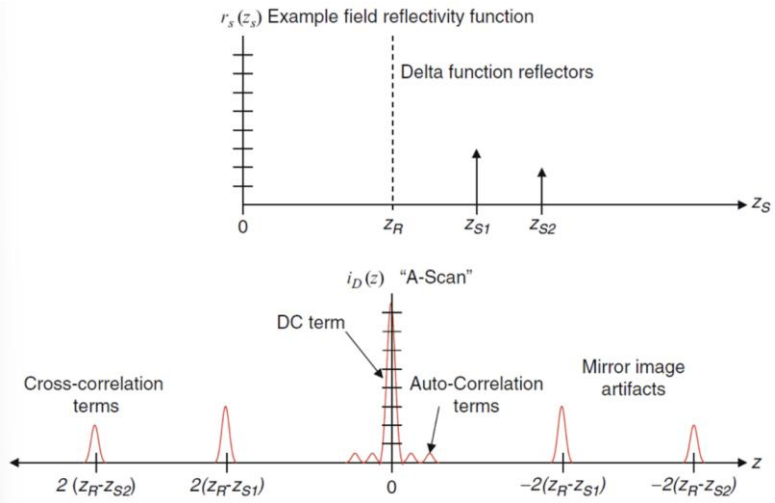

Figure 2-9. Representation of the discrete-reflector sample field reflectivity function (top) and the corresponding "A-scan" (bottom) in SD-OCT. (This figure is adapted from reference [5]).

2.1.4 Sensitivity Fall-off in SD-OCT

The aforementioned spectral interferogram $I_D(k)$ of FD-OCT and its corresponding Fourier transform $i_D(z)$ in Section 2.1.3 illustrate the fundamental principle underlying the SD-OCT imaging system. However, in practical conditions, the spectral interferogram is captured by devices with real-world limitations and is typically recorded through a "sampling" operation to enable rapid digital signal computation of its Fourier transform. The conceptual effects of spectral resolution and the sampling operation on the spectral interferogram and A-scan are illustrated in Figure 2-10.

Firstly, the spectral interferogram is always acquired by instrumentation with limited spectral resolution $\delta_r k$ (or $\delta_r \lambda$), which in SD-OCT is the spectral resolution of the spectrometer, such as the finite spacing of the CCD pixels. As a result, the spectral interferogram may be degraded due to this finite spectral resolution. The effect of the finite spectral resolution can be modelled by convolving the ideal spectral interferogram $I_D(k)$ from Eq. (2-9) with a Gaussian function whose FWHM is $\delta_r k$. The Gaussian function can therefore be expressed as $g(k) = \frac{2\sqrt{ln2}}{\Delta k\sqrt{\pi}} e^{-\frac{4ln2 \cdot k^2}{\delta_r k^2}}$.

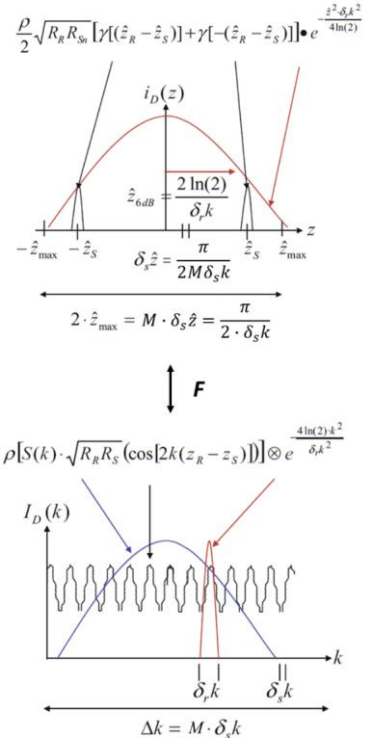

Figure 2-10. Sensitivity "falloff" and imaging depth limits in SD-OCT. The sensitivity falloff at depth $\hat{z}_{6dB}$ is linked to the spectral resolution of the interference pattern, governed by the spectrometer resolution $\delta_r k$ in SD-OCT. (This figure is adapted from reference [5]).

Given the convolution property $F[f(x) \otimes \mathrm{g(x)}] = F[f(x)] \cdot F[g(x)]$, the processed A-scan data is then expressed as the ideal A-scan $i_D(z)$ multiplied by a sensitivity fall-off (or sensitivity "rolloff") factor, whose shape could be obtained by Fourier transforming operation of the Gaussian-shaped spectral resolution factor:

$$i_D(\hat{z}) \exp\left[-\frac{\hat{z}^2 \cdot \delta_r k^2}{4ln2}\right] \overset{F}{\leftrightarrow} I_D(k) \otimes \frac{2\sqrt{\ln 2}}{\Delta k \cdot \sqrt{\pi}} \exp\left[-\frac{4ln2 \cdot k^2}{\delta_r k^2}\right]. \qquad (2\text{-}13)$$

Here, we use the rescaled depth variable $\hat{z} = 2z$ to remove the apparent depth-doubling factor and to allow the processed A-scan data to compare directly with the sample structure. As demonstrated in the exponential terms, the "roll-off" of sensitivity with depth can be understood as the decreasing visibility of higher fringe frequencies corresponding to large sample depths. The sensitivity falloff is quantified as the one-sided depth range at which the sensitivity decreases by a factor of 1/2 (so that $\exp\left[-\frac{\hat{z}^2 \delta_r k^2}{4 \ln 2}\right] = \frac{1}{2}$), which is 6-dB inSNR units:

$$\hat{z}_{6dB} = \frac{2 \ln 2}{\delta_r k} = \frac{\ln 2}{\pi} \frac{\lambda^2}{\delta_r \lambda}, \qquad (2\text{-}14)$$

where $\hat{z}_{6dB}$ is given in both wave number ($\delta_r k$) and wavelength ($\delta_r \lambda$) terms and the latter is recognizable as 1/2 of the coherence length corresponding to the spectral resolution.

Secondly, in real-world processing of spectral interference data in SD-OCT, the computer-based device usually samples the spectral interferogram for rapid digital computation of its Fourier transform. The spectral interferogram is sampled with sampling interval $\delta_s k$ into M channels linearly spaced in the k-domain. Thus, the total collected wave number range is $\Delta k = M \cdot \delta_s k$, and the sampling interval in the z-domain is then set to be $\delta_s \hat{z} = 2\pi \,/\, (2\Delta k) = \pi \,/\, (M \cdot \delta_s k)$ where the factor of 2 in the denominator is due to the use of the rescaled depth parameter $\hat{z}$. Given by the Nyquist criterion, the maximum sampling depth are:

$$\pm \hat{z}_{max} = \pm \frac{\pi}{2 \cdot \delta_S k} = \pm \frac{\lambda^2}{4 \cdot \delta_S \lambda}. \qquad (2\text{-}15)$$

A summary of these parameters is provided in Table 2-1. In addition to these two limitations, which are difficult to overcome, some additional real-world complications can arise, most of which can be handled with appropriate signal processing. For example, dispersion effects due to mismatched optical path lengths between sample arm and reference arm may be corrected by adding appropriate phase factors to the interferometric data before the Fourier transforming operation.

Table 2-1. Effects of finite spectral resolution and sampling in SD-OCT

	6-dB sensitivity roll-off point $\hat{z}_{6dB}$	Maximum one-sided imaging depth $\hat{z}_{max}$
Wavenumber units	$\frac{2\ln 2}{\delta_r k}$	$\frac{\pi}{2 \cdot \delta_S k}$
Wavelength units	$\frac{\ln 2}{\pi} \cdot \frac{\lambda^2}{\delta_r \lambda}$	$\frac{\lambda^2}{4 \cdot \delta_S \lambda}$

Note: $\delta_r k$ and $\delta_r \lambda$: the spectral resolution of the spectrometer; $\delta_s k$ and $\delta_s \lambda$: the spectral sampling interval in signal processing; depth listed here are in free space and should be divided by the refractive index in media.

In conclusion, while the limitations of finite spectral resolution and sampling affect SD-OCT imaging, these can be managed with careful signal processing. Additionally, artifacts such as mirror-image artifacts arising from the cross-correlation terms and artifacts from the DC and autocorrelation terms can also modify the field reflectivity profile and are generally more significant. Approaches have been developed to eliminate these artifacts.

2.1.5 Signal-to-Noise Ratio in Spectral-Domain OCT

As mentioned at the beginning of Section 2.1.3 SD-OCT significantly improves imaging speed and sensitivity, often used interchangeably with SNR if light attenuation is not considered (i.e., assuming the sample surface is a perfect reflector), compared to TD-OCT. SD-OCT achieves increased sensitivity or SNR by significantly reducing noise, particularly shot noise, through the use of a multielement array detector instead of a single-element detector. In a single-detector TD-OCT imaging system, the shot noise produced by the power at a particular wavelength is present at all frequencies, affecting the SNR at all other wavelengths. In contrast, SD-OCT eliminates this cross effect of shot noise by spectrally dispersing each wavelength to a separate detector. The significantly improved sensitivity or SNR (by approximately 2~3 orders of magnitude) of SD-OCT over TD-OCT allows for faster image acquisition speeds without compromising image quality [6] [8].

To theoretically demonstrate the sensitivity of an SD-OCT system, we express the SNR of SD-OCT in decibel units (dB), which denotes the minimum detectable reflected optical power relative to a perfect reflector. SNR is defined as the ratio of squared signal power ($\langle I_D \rangle^2$) to noise process variance (σ^2): $SNR = \frac{\langle I_D \rangle^2}{\sigma^2}$. Complete SNR analysis includes evaluating the

optical power incident on the detector and considering different possible noise sources. The signal and noise terms here are expressed in terms of charge squared $[e^2]$ to facilitate the analysis of noise in cases of detectors using CCDs. Only the real part of the complex cross-correlation term of the spectral density is used, contributing to a detected signal given by:

$$S_{SD} = \frac{\pi^2 e^2 P_{ref} P_{sample} \tau_i^2}{E_\nu}[e^2]. \qquad (2\text{-}16)$$

Here, η denotes the detector efficiency; e is the electron charge; P_{ref} and P_{sample} are the reference arm power and sample arm power per detector element respectively; τ_i represents the integration time and E_ν the photon energy. Noises including the readout noise, dark noise, shot noise (σ_{shot}^2), and relative intensity noise (σ_{RIN}^2) contribute to the overall noise of the detector per readout cycle and per detector element:

$$\begin{aligned} \sigma_{noise}^2 &= \sigma_{r+d}^2 + \sigma_{shot}^2 + \sigma_{RIN}^2 \\ &= \sigma_{r+d}^2 + \frac{\eta e^2 P_{ref} \tau_i}{E_\nu} + \left(\frac{\eta e P_{ref}}{E_\nu}\right)^2 \tau_i \tau_{coh}[e^2]. \end{aligned} \qquad (2\text{-}17)$$

Here, the reference arm power is assumed to be much higher than that of the sample arm; σ_{r+d}^2 denote the sum of readout noise and dark noise; τ_i represents the detector integration time, $\tau_{coh} = \sqrt{\frac{2\ln 2}{\pi}}\frac{\lambda_c^2}{c \cdot \delta\lambda}$ denotes the coherence time with c the light speed and λ_c the centre wavelength of the light source. When shot noise dominants both readout-dark noises and relative intensity noises (i.e. $\sigma_{shot}^2/\sigma_{r+d}^2 > 1$ and $\sigma_{shot}^2/\sigma_{RIN}^2 > 1$), optimal SNR performance is achieved. When the readout-dark noises are equal to the relative intensity noise ($\sigma_{r+d}^2 = \sigma_{RIN}^2$), the optimal reference-arm power is found ($P_{ref} = \frac{\sigma_{r+d} E_\nu}{\eta e \sqrt{\tau_i \tau_{coh}}}$).

For an SD-OCT system to operate close to the shot-noise-limit performance, shot noise should dominate over readout-dark noise and relative intensity noise (RIN) at the optimal reference arm power. Under this circumstance, the inequalities described above can also be expressed as:

$$\frac{e\sqrt{\tau_i}}{\sigma_{r+d}\sqrt{\tau_{coh}}} > 1. \qquad (2\text{-}18)$$

In general, we expect the coherence time τ_{coh} of the detector to be as long as possible and the integration time τ_i as short as possible. Specifically, the coherence time τ_{coh} is inversely proportional to the spectral resolution of the spectrometer ($\tau_{coh} = \sqrt{\frac{2\ln 2}{\pi}}\frac{\lambda_C^2}{c \cdot \delta\lambda}$), which in turn

linearly relates to the maximum ranging depth of the system because the maximum ranging depth is also inversely proportional to the spectral resolution of the spectrometer ($\pm z_{max} = \pm\frac{\lambda_c^2}{4\cdot\delta\lambda}$). Thus, a longer coherence time allows higher maximum ranging depth. Decreasing the integration time permits an increase in the reference arm power without saturating the detector which consequently reduces the autocorrelation noise induced by interference within the sample in an ultrahigh-speed SD-OCT. Conclusively, the system performance is mostly determined by the readout and dark noise (σ_{r+d}) of the detector as presented in Eq. (2-18).

Thus, the SNR of SD-OCT system that operates in the shot noise limit performance is shown to be:

$$SNR_{SD} = \frac{S_{SD}}{\sigma_{noise}^2} = \frac{\frac{\eta^2 e^2 P_{ref} P_{sample} \tau_i^2}{E_\nu^2}}{\frac{\eta e^2 P_{ref} \tau_i}{E_\nu}} = \frac{\eta P_{sample} \tau^i}{E_\nu}. \qquad (2\text{-}19)$$

As shown in Eq. (2-19), in the shot-noise-limit, SNR of SD-OCT appears to be independent of the spectral bandwidth of the light source. This implies that the axial resolution can be improved without penalty to the system's SNR, provided the full spectral bandwidth is imaged onto an array detector, such as a CCD. However, it is worth noting that the sample arm power in Eq. (2-19) is assumed to come from a single sample reflecting surface. In biological tissue, the back-reflected power comes from multilayered structures along the depth profile, and the SNR at a position along the depth is given on average by the total power reflected by all depths within the coherence length of the light source. Thus, as the axial resolution increases, the coherence length decreases, resulting in a decrease in the total back-reflected power within the light coherence length. Consequently, the SNR at a particular position will reduce as the axial resolution increases.

In conclusion, this section introduced the essential theories behind OCT imaging. The following section presents its application in skin diagnostics.

2.2 Skin Diagnosis and OCT

2.2.1 Importance of Skin Health and Diagnostic Challenges

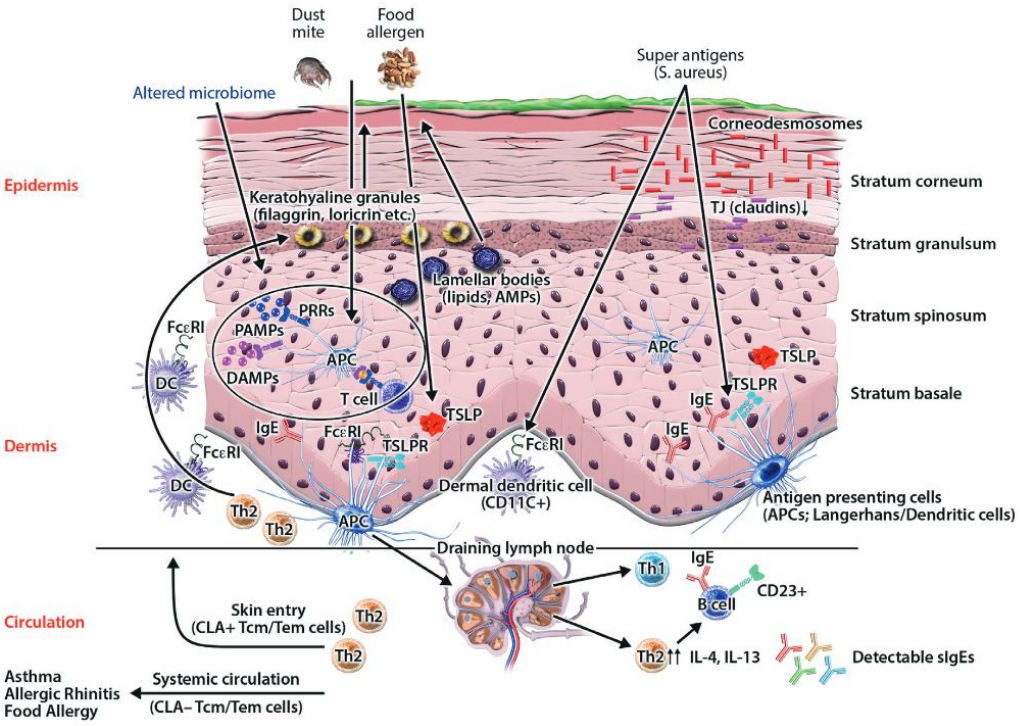

Figure 2-11. A compromised skin barrier increases allergen penetration and triggers activation of the innate immune system. Various factors contribute to skin barrier dysfunction, including immune dysregulation, impaired terminal epithelial differentiation like filaggrin (FLG) deficiency, reduced antimicrobial peptides (AMPs), changes in the composition of intercellular lipids in the stratum corneum, and alterations in the skin microbiome. (This figure is adapted from reference [9]).

In recent years, both intrinsic and extrinsic factors affecting skin health—particularly aging and moisture retention—have gained increasing attention. Skin aging involves structural deterioration driven by two main processes: chronological aging, a natural decline in cellular regeneration, and photoaging, caused by ultraviolet (UV) exposure and oxidative stress [10]. These lead to dryness, wrinkles, and pigmentation changes, as cumulative damage to deoxyribonucleic acid (DNA) and proteins weakens the skin barrier.

Dry skin (xerosis) commonly accompanies aging due to reduced lipid synthesis and external stressors like low humidity or irritants. The stratum corneum, the outermost barrier layer, relies on a lipid matrix to retain moisture, but its composition deteriorates with age, leading to increased trans-epidermal water loss. Moisturizers that replenish lipids and trap moisture are widely used to counteract xerosis and improve skin texture, serving both therapeutic and

preventive roles in skin aging [10].

Beyond dryness, skin barrier dysfunction can initiate immune responses and contribute to conditions like atopic dermatitis (AD). As shown in Figure 2-11, a compromised barrier allows allergen penetration, activating antigen-presenting cells (APCs) and T cells, which release cytokines (e.g., IL-4, IL-13, TSLP), further weakening the barrier [9]. This cycle of inflammation is aggravated by filaggrin deficiency, impaired tight junctions, and microbial imbalance (dysbiosis), increasing susceptibility to chronic inflammation and related disorders such as asthma and allergic rhinitis [9].

Given this complexity, there is a growing demand for non-invasive diagnostic tools capable of detecting early signs of barrier dysfunction and inflammation. Advanced imaging and sensing technologies offer real-time monitoring of structural and biochemical changes, enabling early intervention and improved disease management [9].

Finally, lipid composition within the stratum corneum plays a critical role in barrier function. An organized matrix of ceramides, cholesterol, and fatty acids maintains hydration and prevents pathogen entry. In AD, this balance is often disrupted, compromising barrier integrity and exacerbating immune activation. Restoring lipid homeostasis has been proposed as a promising therapeutic strategy to support barrier repair and reduce inflammation [11].

To understand the motivation for applying OCT in dermatology, we first review the importance of skin health, and the challenges associated with current diagnostic methods. This lays the groundwork for exploring why advanced imaging modalities are needed.

2.2.2 Overview of Non-Invasive Skin Imaging Techniques

Non-invasive imaging has become vital in dermatology, offering detailed visualization of skin structure without the need for biopsies. Among these, OCT stands out for its ability to provide high-resolution, depth-resolved images in real time. OCT combines ultrasonography and optical interferometry, enabling vertical and horizontal section imaging with penetration depths up to 2 mm [12].

Dynamic OCT (D-OCT) extends this by visualizing skin microvasculature, aiding in the differentiation of benign and malignant lesions, such as nevi and melanoma, through vascular pattern analysis. This vascular capability addresses limitations of traditional OCT, which struggled with melanocytic lesion identification [12].

OCT and D-OCT are widely used for diagnosing actinic keratosis, non-melanoma skin cancers, and inflammatory conditions such as eczema, psoriasis, and scleroderma, especially where techniques like Reflectance Confocal Microscopy (RCM) fall short. These modalities also support wound monitoring and assessment of age-related changes in skin structure, offering real-time tracking of tissue response [12].

Advancements in SD-OCT have further improved imaging speed and resolution, enabling the detection of subtle, dynamic changes in skin layers and cellular structure—essential for monitoring rapidly evolving conditions like inflammatory dermatoses [13].

Despite its strengths in structural imaging, OCT does not capture biochemical or molecular changes, such as inflammation markers or metabolic activity shifts, which often precede visible structural alterations. This limitation highlights the need for complementary approaches, such as integrating OCT with molecular assays or multimodal imaging, to achieve a more complete understanding of skin pathology [13].

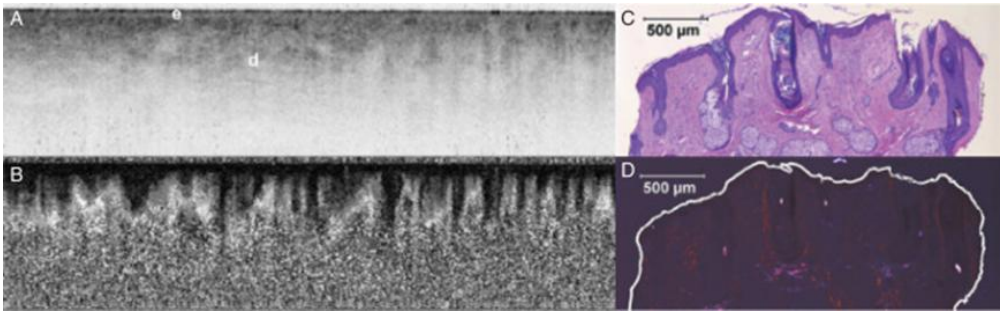

Figure 2-12. In vivo OCT images of normal human skin. Standard (A) and polarization-sensitive (B) scans captured from the forehead, spanning 5 mm in width and 1.2 mm in depth. Matching histological sections from the same area, stained with H&E, are shown under brightfield (C) and polarized (D) microscopy. (This figure is adapted from reference [13]).

Figure 2-12, Figure 2-13 and Figure 2-14, Figure 2-13 and Figure 2-14 illustrate the diverse applications of OCT in imaging normal and pathological human skin, enhancing our understanding of skin structure and conditions. Figure 2-12 presents OCT images of normal human skin from the forehead, with conventional structural imaging (A) and polarization-sensitive imaging (B) showing depth up to 1.2 mm. The corresponding histology images (H&E stained) viewed under brightfield (C) and polarized (D) microscopy confirm the OCT's accuracy in visualizing skin layers in vivo [13].

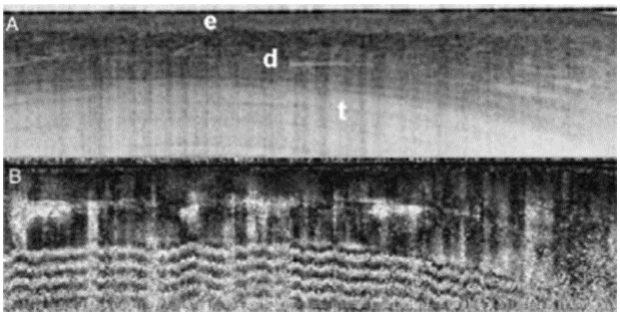

Figure 2-13. In vivo OCT images of normal human skin. Structural (A) and polarization-sensitive (B) scans of the skin above the metacarpal phalangeal joint of the index finger, covering a width of 5 mm and a depth of 1.2 mm. The epidermal (e) and dermal (d) layers are clearly observed, overlaying the extensor tendon (t). (This figure is adapted from reference [13]).

Figure 2-13 depicts OCT images of normal human skin over the metacarpal phalangeal joint of the index finger. The structural image (A) and polarization-sensitive image (B) reveal clear distinctions between the epidermal (e) and dermal (d) layers, extending down to the extensor tendon (t). This demonstrates OCT's ability to provide detailed layer-by-layer visualization, essential for assessing structural integrity and identifying abnormalities within skin layers [13].

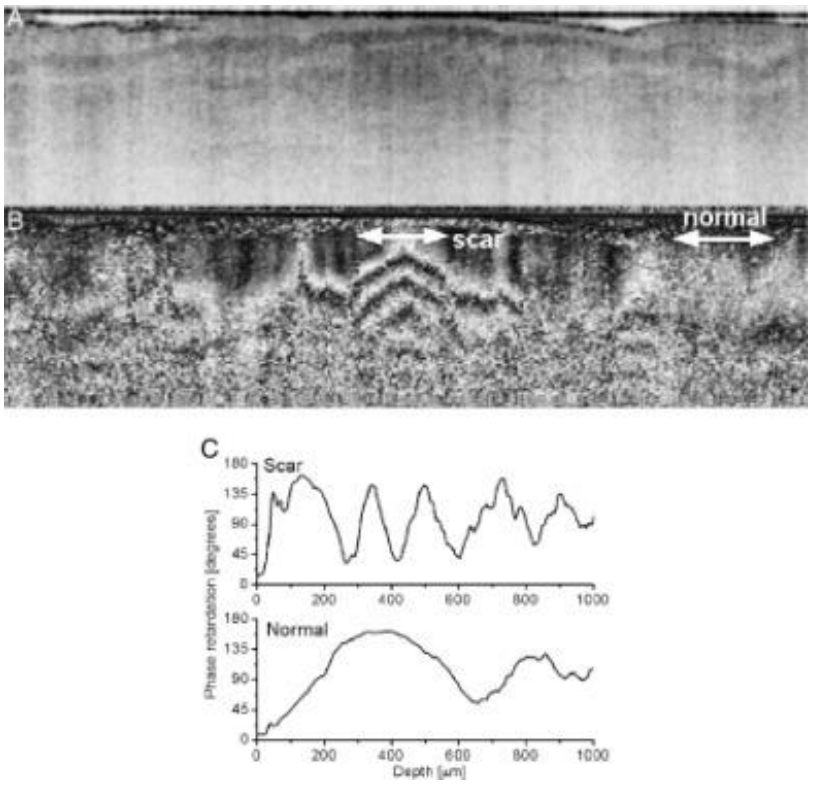

Figure 2-14. In vivo OCT images of scar tissue. Structural (A) and polarization-sensitive (B) scans from a scarred area on the hand, spanning 5 mm in width and 1.2 mm in depth. Labelled arrows in (B) mark regions identified as scar tissue and adjacent normal skin based on clinical assessment. (C) Plots of average phase retardation versus depth below the skin surface, calculated within the regions indicated by the labelled arrows

in (B). (This figure is adapted from reference [13]).

Figure 2-14 focuses on OCT images of scar tissue on the hand, showing structural (A) and polarization-sensitive (B) views. The labelled arrows in image (B) indicate clinically determined regions of scar tissue adjacent to normal skin, highlighting OCT's utility in differentiating between scarred and healthy tissue. The accompanying graph (C) shows phase retardation as a function of depth, calculated in the regions marked by the arrows in (B). This data provides additional quantitative insight into tissue properties, such as density and organization, which are altered in scar tissue [13].

Through these examples, OCT demonstrates its versatility and precision in skin diagnostics, offering clinicians critical insights into both normal and pathological skin structures. However, OCT's structural focus necessitates complementary techniques to capture biochemical changes, thereby enabling a more comprehensive approach to diagnosing and managing complex skin conditions [13].

Building on the diagnostic challenges discussed, this section introduces common non-invasive imaging modalities—such as dermoscopy, ultrasound, confocal microscopy, and others—and compares their capabilities and limitations relative to OCT.

2.3 OCTA and Blood Flow Velocimetry

2.3.1 Working Principle of OCTA

OCTA is a major advancement in ophthalmic imaging, providing high-resolution, depth-resolved visualization of retinal and choroidal blood flow. Unlike fluorescein angiography (FA), which is limited to superficial vessels, OCTA can image deeper plexuses such as the radial peripapillary, intermediate, and deep capillary networks, offering new opportunities for disease characterization, monitoring, and treatment evaluation [2].

OCTA detects blood flow by analysing motion contrast from repeated A-scans at the same location—stationary tissues remain unchanged, while moving blood cells produce detectable differences. These changes are visualized as flow maps (Figure 2-15 and Figure 2-16), enabling 3D vascular imaging [2].

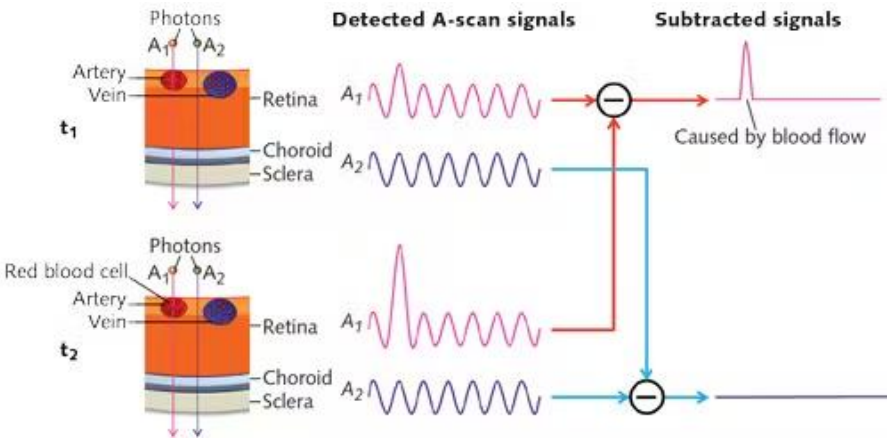

Figure 2-15. OCTA working principle. A_1 represents the OCT signal from a moving particle, while A_2 corresponds to the OCT signal from static tissue. The signals are captured at two time points, t_1 and t_2. (This figure is adapted from reference [14]).

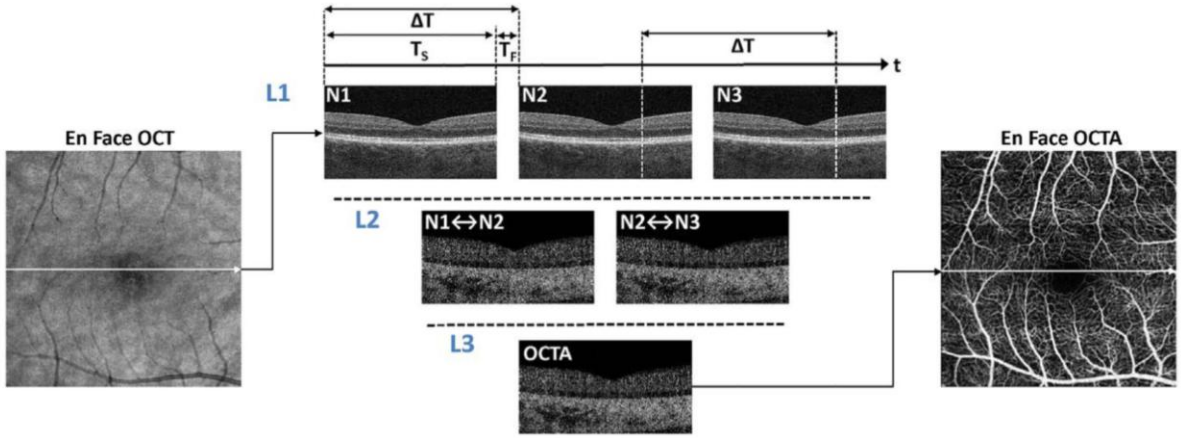

Figure 2-16. Simplified representation of OCTA. OCTA maps vasculature by identifying motion contrast from flowing blood cells. Multiple B-scans (N1, N2, N3) are captured at the same retinal location (Line L1), and differences or decorrelations between consecutive B-scans are computed (Line L2). The resulting decorrelation data is compiled into an OCTA cross-sectional image (Line L3), and this process is repeated at different positions to create a 3D volumetric dataset. The acquisition time (TS) for each B-scan is determined by the A-scan rate and the number of A-scans per B-scan. The OCT beam rapidly returns to its starting position during the flyback time (TF), and the B-scan is repeated after a time delay (ΔT), which is the sum of acquisition and flyback times. Each A-scan within a B-scan is also repeated at the interscan time, which is a critical parameter affecting OCTA sensitivity and saturation. (This figure is adapted from reference [2]).

The technique evolved from Doppler OCT [15], [16], which measured phase shifts between A-scans but struggled with detecting perpendicular flow. Optical Microangiography (OMAG) addressed this by introducing phase modulation, successfully imaging microvasculature in both animal and human studies [1], [2], [17]. Further improvements came with Split-Spectrum Amplitude Decorrelation Angiography (SSADA), which enhanced flow detection sensitivity

and image clarity.

With a basic understanding of OCT and skin imaging, we now turn to OCTA. This section outlines the fundamental principle of OCTA, which derives flow information from temporal decorrelation between repeated B-scans.

2.3.2 Optical Microangiography (OMAG)

OMAG is a pivotal technique in the development of OCTA. It addressed the challenge of bulk eye motion by modifying OCT hardware to introduce phase variations, which improved the differentiation between stationary tissue and blood flow. OMAG has been instrumental in visualizing cerebral vasculature through the intact skull in mice and has been applied to human retinal and choroidal vasculature. The technique uses OCT to acquire volumetric data, segment retinal layers, and display vascular structures in *en-face* images. By compensating for bulk eye motion, OMAG has paved the way for more accurate and detailed visualization of blood flow within the eye [2].

OMAG utilizes the principle of complex OCT signals to distinguish between static and dynamic scattering particles (e.g., red blood cells) [17] [19]. OMAG performs differential operation between adjacent measurements in the amplitude, phase and complex information as:

$$OMAG = \frac{1}{N-1}\sum_{i=1}^{N-1}(|C_{i+1} - C_i|) \qquad (2\text{-}20)$$

where C_i is the corresponding complex information of OCT signal in the i'th of all N repeated measurements [19]. By modulating the phase of the OCT signal, OMAG enhances the sensitivity to flow by introducing phase shifts that cause decorrelation between sequential scans of moving particles. This method allows for the extraction of flow information with high sensitivity and resolution [20].

Among the various OCTA algorithms, OMAG stands out for its ability to resolve capillary-level blood flow. This section details its core mechanism and strengths in high-resolution flow detection.

2.3.3 Split-Spectrum Amplitude Decorrelation Angiography (SSADA)

SSADA improves SNR and reduces sensitivity to bulk eye motion by dividing the OCT spectrum into multiple narrow-band spectra. This division reduces axial image resolution, which helps match the transverse OCT image resolution and reduces sensitivity to eye motion.

By calculating speckle decorrelations on a B-scan to B-scan basis and combining the split spectral data, SSADA generates a single data set with increased SNR. This technique has been widely adopted in commercial OCTA instruments, significantly enhancing their performance [2].

The SSADA algorithm measures the amplitude decorrelation. The decorrelation calculation is achieved purely through processing the amplitude signal and does not require phase information. To evaluate the flow signals coming from the scattering tissue, the average decorrelation image $\overline{D}(x,z)$, at each position was obtained by averaging N-1 decorrelation image frames computed from N reflectance amplitude images frames from M-B mode scanning. Each decorrelation frame was computed from 2 adjacent amplitude frames: $A_n(x,z)$ and $A_{n+1}(x,z)$. Using the full spectrum, it is given by:

$$\overline{D}(x,z) = 1 - \frac{1}{N-1}\sum_{n=1}^{N-1}\frac{A_n(x,z)A_{n+1}(x,z)}{\frac{1}{2}A_n(x,z)^2 + \frac{1}{2}A_{n+1}(x,z)} \qquad (2\text{-}21)$$

where x and z are lateral and depth indices of the B-scan images and n denotes the B-scan slice index. In this equation, the decorrelation SNR acquired from full spectrum can only be increased by increasing the number N of B-scans taken at the same position [3].

In contrast to OMAG, SSADA uses spectrum-splitting to improve the robustness of decorrelation signals. We now examine how SSADA enhances flow contrast while reducing motion noise.

2.3.4 OCTA Developments

OMAG and SSADA have both significantly advanced OCTA by addressing different imaging needs. OMAG provides high-resolution microvascular detail, particularly in slow-flow environments, while SSADA enhances SNR and reduces motion artifacts, making it well-suited for clinical retinal imaging. The choice between them depends on specific diagnostic requirements, with each offering complementary strengths.

The commercialization of OCTA began with the release of AngioVue (Optovue) in 2014, followed by SS-OCT systems from Topcon and Zeiss. The integration of Vertical-Cavity Surface-Emitting Laser (VCSEL) technology has enabled faster imaging speeds, expanding OCTA's potential for real-time, high-throughput imaging [21], [22], [23].

OCTA offers several advantages: non-invasive, depth-resolved visualization of

microvasculature, high-contrast imaging without dye, and generation of quantitative vascular markers. It allows for rapid, repeatable scans, which are especially valuable in disease monitoring. However, limitations include insensitivity to vascular leakage, dependency on high imaging speeds, limited flow quantification range, and potential imaging artifacts requiring careful interpretation [24], [25], [26].

The creation of OCTA images relies on motion contrast detection through repeated B-scans at the same location. Interscan time plays a critical role in balancing flow sensitivity and motion artifact suppression. Post-processing methods like threshold masking are used to minimize noise and enhance image fidelity. Final outputs can be displayed via en-face projections and cross-sectional overlays, enabling detailed visualization of retinal and choroidal vasculature [2].

In summary, OCTA has revolutionized ophthalmic imaging by providing non-invasive, high-resolution blood flow visualization. Techniques like OMAG and SSADA, combined with advances in hardware and processing, have improved accuracy and clinical relevance. Despite certain limitations, OCTA remains a powerful tool for diagnosing and managing retinal and choroidal vascular diseases [2], [3], [27].

This section reviews recent advances in OCTA technologies, focusing on improvements in imaging speed, sensitivity, and motion robustness for clinical skin applications.

2.3.5 OCTA-Blood Flow Velocity Model by SSADA

Blood flow velocimetry in OCTA involves quantifying flow velocity within the microvasculature by analysing either Doppler shifts or decorrelation rates in the OCT signal. Accurate flow measurement is essential for evaluating vascular health and identifying abnormalities.

A major milestone came in 2013 when Tokayer et al. introduced a quantitative method using SSADA to relate decorrelation signals to blood flow velocity and interscan time. Their work established a linear estimation model and examined the influence of Doppler angle, providing a reproducible framework that has since guided OCTA-based flow analysis [28].

Using phantom experiments, they presented:

- The relationship between decorrelation and interscan time (Figure 2-17).
- The relationship between decorrelation and flow velocity (Figure 2-18).

Their results showed that decorrelation is proportional to either interscan time or flow velocity before reaching a saturation level. These relationships are simplified into a linear model for practical application. Furthermore, the decorrelation is characterized with Doppler angle as monotonically proportional and independent of flow velocity influence (Figure 2-19) [28].

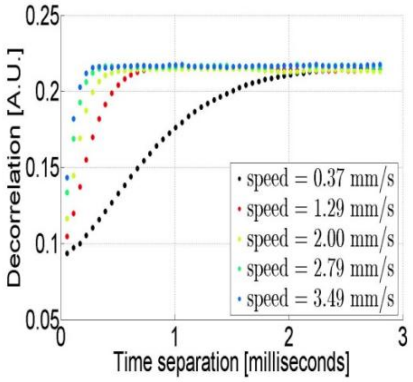

Figure 2-17. Decorrelation values recorded at various interscan times (Δt) for different flow speeds. (This figure is adapted from reference [28])

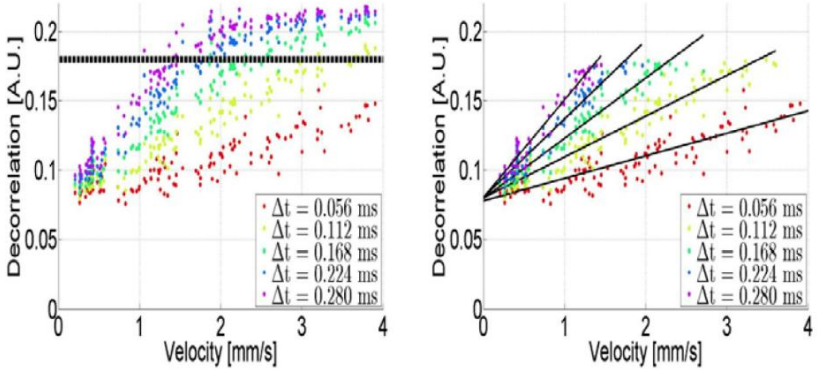

Figure 2-18. Decorrelation values observed at different flow velocities for various interscan times (Δt). (This figure is adapted from reference). [28])

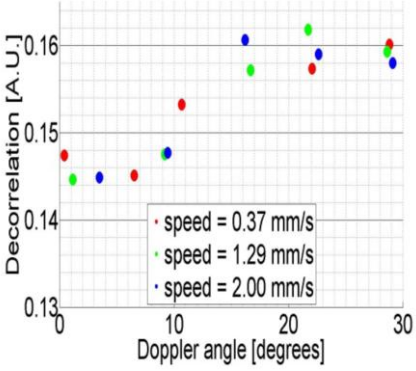

Figure 2-19. Relationship between measured SSADA decorrelation signal and Doppler angle. The Spearman's correlation coefficient (ρ) is 0.87, indicating a strong monotonic relationship between decorrelation values and

Doppler angle. The observed relationship follows a sigmoidal pattern. (This figure is adapted from reference). [28])

This method serves as an initial, accurate, and feasible approach for OCTA blood flow velocimetry. However, its accuracy is affected by the Doppler angle, which contributes an additional decorrelation component to the overall signal. By combining this method with Doppler OCT, a complementary approach is achieved: while Doppler OCT can measure flow in any direction except when the flow is perpendicular to the scanning beam (resulting in a 0-degree Doppler angle) [15] [16], this method is most accurate when the Doppler angle is 0 degrees. This synergy allows for comprehensive blood flow measurement, leveraging the strengths of both techniques to overcome individual limitations.

Su et al. expanded upon the quantitative groundwork laid by Tokayer et al. by introducing a microfluidic chip to standardize OCTA measurements, addressing the need for consistent calibration across different OCTA systems. The characterization of decorrelation in relation to flow velocity and interscan time was achieved using the following analytical model [29]:

$$D = (D_{sat} - D_{Brownian}) \cdot \left(1 - e^{-\frac{3V}{V_{sat}}}\right) + D_{Brownian}, \qquad (2\text{-}22)$$

where D is the SSADA decorrelation value measured at the centerline of microfluidic channels, D_{sat} is the saturated decorrelation value, and V_{sat} is defined as the saturation velocity, where D reaches 95% of D_{sat}. $D_{Brownian}$ is the background decorrelation value caused by the Brownian motion. $D_{Brownian}$ was se as a constant value based on the measurement and the values for $D_{sat}$and V_{sat}were found by the fitting [29].

Furthermore, the relationship between the saturated decorrelation and the flow channel width is characterized by:

$$D_{sat} = (D_{sm} - D_{Brownian}) \cdot \left[\frac{erf\left(\frac{w}{2\sqrt{2}\sigma}\right)}{\left\{B*\left[1-erf\left(\frac{w}{2\sqrt{2}\sigma}\right)\right]+erf\left(\frac{w}{2\sqrt{2}\sigma}\right)\right\}}\right] + D_{Brownian}, \qquad (2\text{-}23)$$

where B is a constant related to background reflection and $D_{\mathrm{sm}}$is the maximum saturated decorrelation value. D_{sat} is the saturated decorrelation value when the beam spot size is much less than the channel size. σ is a constant related to beam size and w is the channel width [29]. erf is error function. A phantom experiment is conducted to verify the relationship between saturated decorrelation (D_{sat}) and channel width (w) as shown in Figure 2-20.

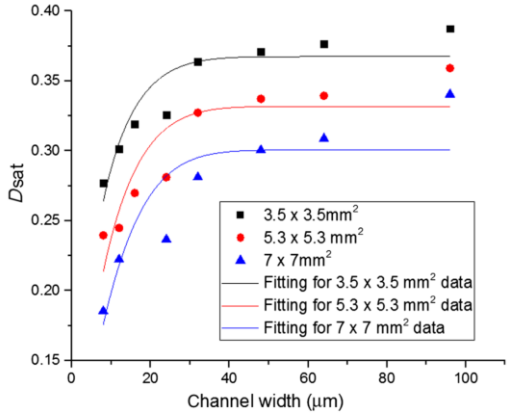

Figure 2-20. Relationship between the saturated decorrelation value (D_{sat}) and channel width at a blood flow speed of 15 mm/s. Black squares, red circles, and blue triangles represent data points for scan sizes of 3.5 × 3.5 mm², 5.3 × 5.3 mm², and 7 × 7 mm², respectively. The black, red, and blue lines correspond to fits using Eq. *(2-23)* for each scan size. D_{sm} is a model parameter that defines the maximum D_{sat} value. (This figure is adapted from reference *[29]*)

Yang et al. further optimized OCTA calibration by analysing how hematocrit levels of the blood affect OCTA signals. The decorrelation signal should include the influence by hematocrit concentration (HCT) as:

$$D(HCT) = 1 - M_S - M_F g_A\left(HC\mathrm{T} \times \mathrm{erf}\left(\frac{w}{2\sqrt{2}\,\sigma}\right)\right), \qquad (2\text{-}24)$$

where M_S is the portion of signal from static particles and M_F is the portion of the signal from the moving particles, anisotropy $g_A(\mathrm{HCT}) = e^{-2k_0^2 \frac{\mu_a(\lambda,HCT)+\mu_s'(\lambda,HCT)}{\mu_s(\lambda,HCT)} v_0^2 \Delta t^2/6}$, μ_a is absorption coefficient and μ_s is scattering coefficient. $\mu_s'$is reduced scattering coefficient [30].

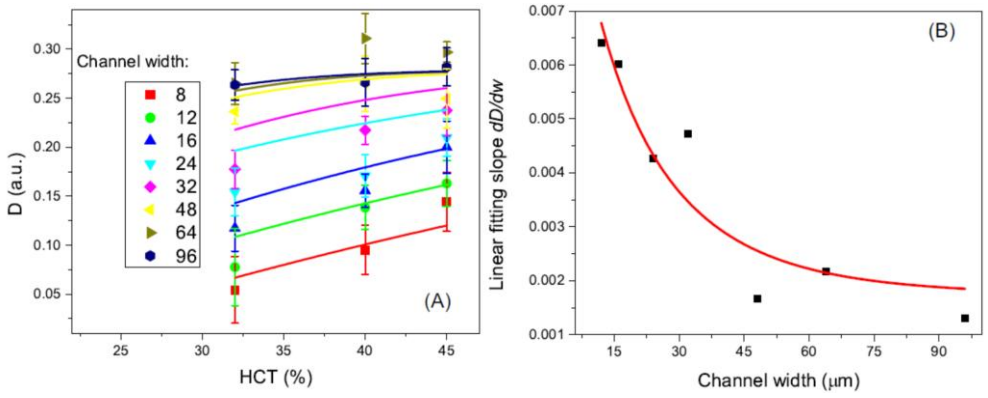

Figure 2-21. (A) Decorrelation values plotted against HCT for channel widths ranging from 8 μm to 96 μm. Solid lines represent the theoretical model fitting for each channel width. (B) The slope of the linear fit to

experimental data as a function of channel width, with the red solid line indicating the theoretical model fitting. (This figure is adapted from reference [30])

The SSADA method for blood flow velocimetry has been successfully applied to in-vivo imaging. Building on this foundation, the dynamic range—defined as the valid decorrelation region for the linear estimation model—was further enhanced by integrating multiple SSADA images obtained at different interscan times. This enhanced method, known as High Dynamic Range (HDR) OCTA, significantly improves the dynamic range of the original technique. The increase in dynamic range was validated through phantom experiments, as demonstrated in Figure 2-22. Furthermore, the HDR-OCTA method was tested *in-vivo*, with promising results illustrated in Figure 2-23 [31]. This advancement allows for more accurate and detailed imaging of blood flow dynamics, enhancing the applicability and reliability of OCTA in clinical settings.

OCTA not only visualizes vasculature but also offers the potential to quantify blood flow. Here, we introduce the velocity estimation model based on SSADA and discuss its assumptions and limitations.

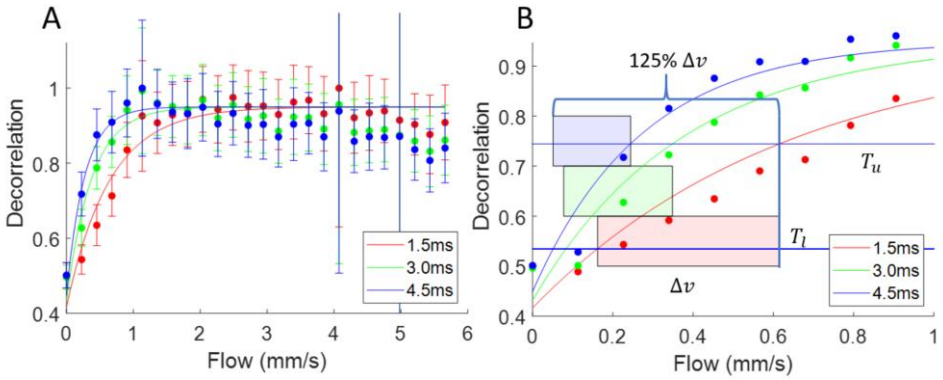

Figure 2-22. (A) Fitted results from flow phantom experiments at various scanning intervals and flow speeds. (B) Dynamic range derived from experimental data, with shaded rectangles highlighting the dynamic range for different scanning intervals. Δv represents the dynamic range for a 1.5 interval, while combining three intervals expands the dynamic range by 125%. T_u denotes the upper threshold, and T_l the lower threshold. (This figure is adapted from reference [31])

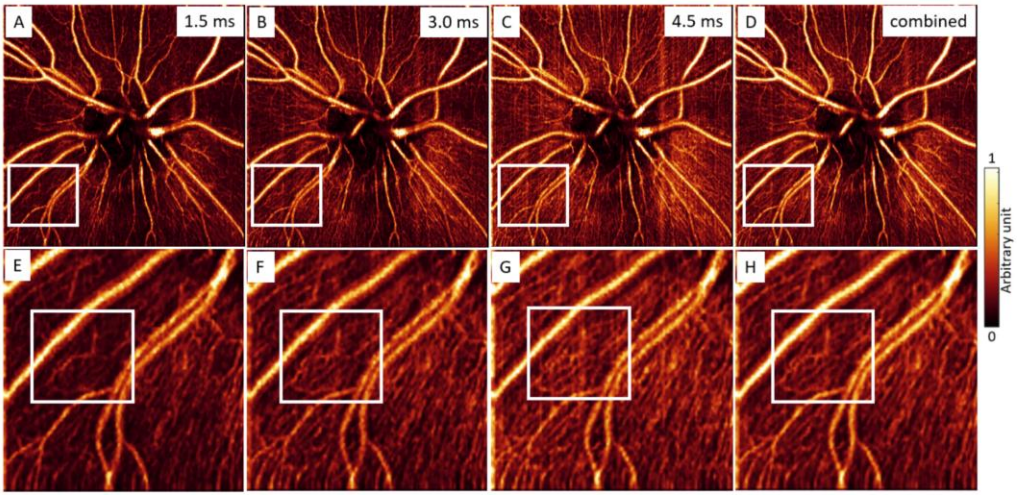

Figure 2-23. Human peripapillary retina images. (A-C) Images captured at three distinct scanning intervals, each with a unique dynamic range. (D) Combined HDR-OCTA image. The white boxes in A, B, C, and D are enlarged in E, F, G, and H, respectively. A smaller white box within E, F, G, and H highlights regions with notable differences between the scanning intervals. (This figure is adapted from reference [31])

2.3.6 OCTA-Blood Flow Velocity Model by OMAG

Beyond SSADA, OMAG has also been verified for its relationship between signal and blood flow velocity, as well as interscan time [18]. The analytical model for the OMAG signal is given by:

$$I_{OMAG} = \sqrt{\left[0.89\sqrt{\frac{6C\cdot V_{vael}}{\pi d^3}}(\alpha(t)+\alpha(t+\Delta T))\right]\left[1-\left[\exp\left(-\frac{8}{6}\left(\frac{2\pi}{\lambda_0}\right)^2\langle V^2\rangle\Delta T^2\right)\right]^{\frac{1}{2}}\times c\cos\left(\Delta\phi(t)\right)\right]}, \quad (2\text{-}25)$$

where C is the particle concentration, V_{vael} is the total imaging voxel volume, d is the particle diameter assuming spherical particles, $\alpha(t)$ and $\alpha(t+\Delta T)$ are the backscattering coefficients of single particle (reflectance), N is the number of particles, $\Delta\phi(t)$ is the difference between the two random phases at scan time t and $t+\Delta T$, ΔT is the interscan time and λ_0 is the central wavelength.

This model was verified through phantom experiments, with results shown in Figure 2-24 and Figure 2-25. Additionally, the relationship involving particle concentration was characterized and presented in Figure 2-26. These findings confirm that the OMAG signal is suitable for a linear estimation model for blood flow velocimetry. However, it was observed that the OMAG signal is not dependent of the flow channel width, as depicted in Figure 2-27. This indicates that while OMAG is effective for blood flow measurement, additional considerations for

channel width are unnecessary to ensure accuracy.

Similarly, the OMAG-based approach to velocity quantification is discussed next, with attention to how phase-resolved techniques extend its capability beyond mere vessel mapping.

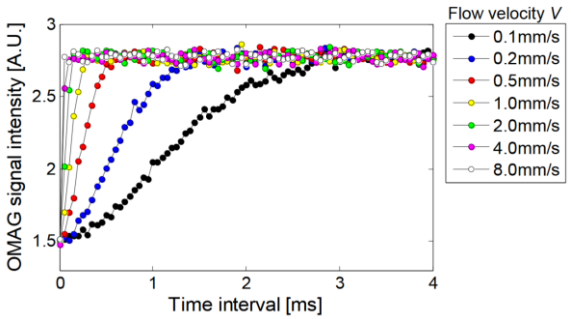

Figure 2-24. Numerical simulation of multi-time scale OMAG magnitudes at varying flow velocities with 5% Intralipid. (This figure is adapted from reference). [18])

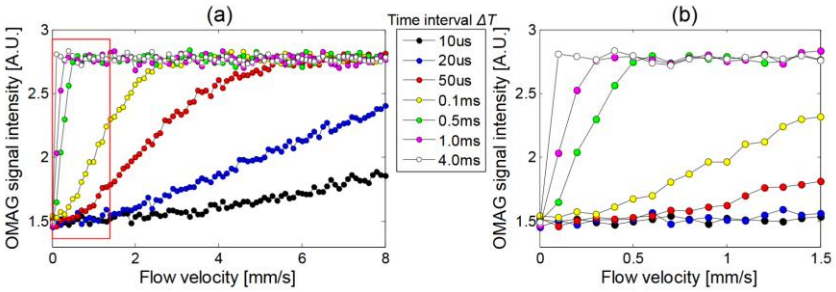

Figure 2-25. (a) Numerical simulation of multi-velocity scale OMAG magnitudes by adjusting time intervals in a scattering medium with 5% Intralipid solution (Visualization 1 and Visualization 2). (b) Enlarged view of the red box area in (a). (This figure is adapted from reference [18])

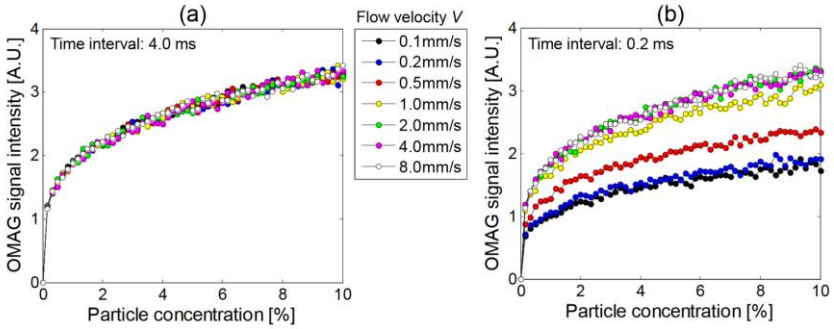

Figure 2-26. Numerical simulation of multi-concentration scale OMAG magnitudes with varying flow velocities at time intervals of (a) 4.0 ms and (b) 0.2 ms, respectively (Visualization 3). (This figure is adapted from reference [18])

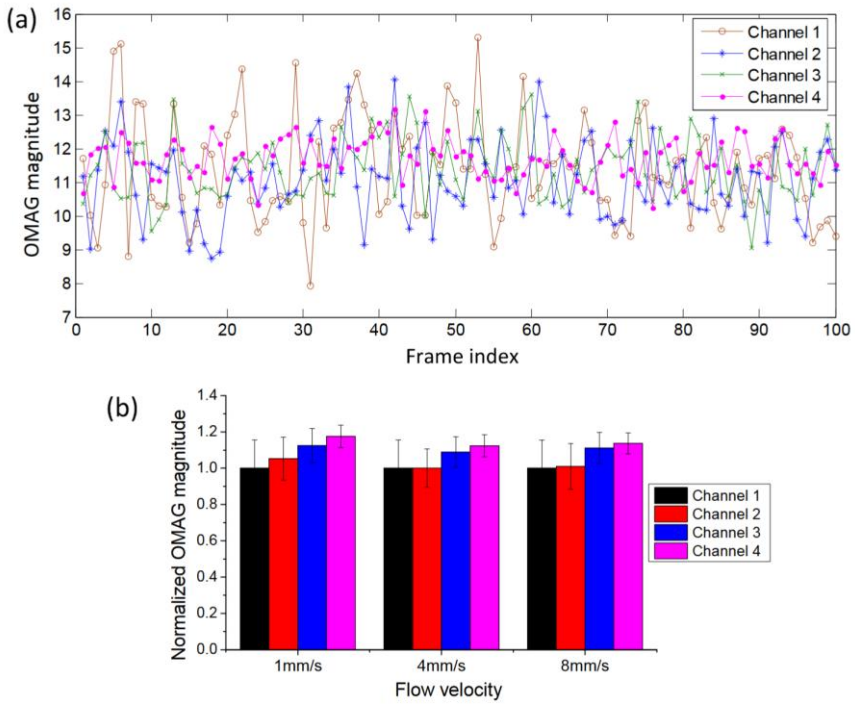

Figure 2-27. (a) OMAG signal intensity across four channels over 100 consecutive cross-sections at the same frame location (pump rate = 34.56 μL/hr). (b) Normalized OMAG intensity comparison for the four channels under pump rates corresponding to flow velocities of 1 mm/s, 4 mm/s, and 8 mm/s. Mean values and standard deviations were calculated from all measurements. (This figure is adapted from reference). [18])

2.3.7 Bias Velocity Method for Transverse Motion Velocimetry

Dynamic Light Scattering OCT (DLS-OCT) combines the strengths of dynamic light scattering and OCT to enable high-resolution 3D imaging of particle dynamics, including both diffusion and translational motion. This technique allows for precise measurement of parameters such as axial/transverse velocities and diffusion coefficients at micrometer-scale resolution.

DLS analyses particle motion via the autocorrelation function of scattered light, while OCT provides depth-resolved imaging through coherence gating. In DLS-OCT, the autocorrelation is derived from the phase-resolved OCT signal, enabling differentiation between static and dynamic scatterers. The method accounts for factors such as finite probing volume, non-ergodicity, and mixed motion types, making it a powerful tool for blood flow measurement and microvascular analysis [32].

The amplitude of the autocorrelation of the DLS-OCT signals is:

$$|g(\tau)| = e^{-(\gamma\tau)^2} \qquad (2\text{-}26)$$

γ roles as the decaying rate of $|g(\tau)|$. If consider only $g(\tau) = e^{2ikv_z\tau}e^{-4kD|\tau|}e^{-v_z^2\tau^2/w_z^2}e^{-(v_x^2+v_y^2)\tau^2/w_{xy}^2}$, along x axis only, then:

$$\gamma = \left[\frac{\left(v_x^{flow} - v_x^{scan}\right)^2}{w_{xy}^2} + \frac{\left(v_y^{flow}\right)^2}{w_{xy}^2} + \frac{\left(v_z^{flow}\right)^2}{w_z^2} + \frac{4k^2D}{\tau}\right]^{\frac{1}{2}} \qquad (2\text{-}27)$$

to be in the form of $\gamma = [A(B - v_x^{scan})^2 + C]^{1/2}$, where $A = 1/w_{xy}$, $B = v_x^{flow}$ and $C = \left(v_y^{flow}\right)^2 + \frac{w_{xy}^2\left(v_z^{flow}\right)^2}{w_z^2} + \frac{4k^2D}{\tau}w_{xy}^2$, and simplified in non-diffusive:

$$\gamma = \sqrt{\frac{\left(v_x^{flow} - v_x^{scan}\right)^2}{w_{xy}^2}} = \frac{\left|v_x^{flow} - v_x^{scan}\right|}{w_{xy}}, \qquad (2\text{-}28)$$

where τ is the interscan time, v_x^{flow} is the flow velocity along x direction, v_x^{scan} is the scan velocity along x direction, v_y^{flow} is the flow velocity along y direction, v_z^{flow} is the flow velocity along z direction, w_{xy} is the transverse resolution (in x-y plane), w_z is the axial resolution (in z direction), k is the wave-vector and D is the diffusivity of the particles.

The scheme is shown in Figure 2-28. To get the minimum decay rate, γ_{min}, $v_x^{flow} = v_x^{scan}$ is a must, whereas the single particle is relatively static to the scan, and the decorrelation holds only for orthogonal motion and diffusion. Inversely, when measured with γ_{min}, B will be equal to v_x^{scan} and is v_x^{flow} [33].

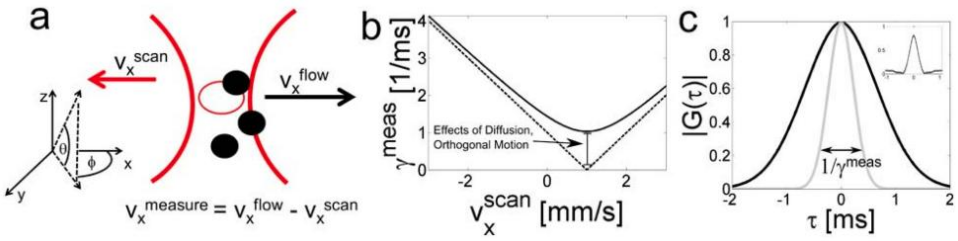

Figure 2-28. Symmetry breaking and resolving directional ambiguity using scan bias. (a) Three reference frames are illustrated: flow, scanning, and measurement, with corresponding angles defined, including the latitudinal angle θ and longitudinal (azimuthal) angle ϕ. (b) Theoretical decay rate-scan bias curve, comparing the case where v_x^{flow} is the sole flow component (dashed line) to the scenario with additional orthogonal motion and diffusion (solid line). (c) Theoretical autocorrelation curves for two scan biases: $v_x^{scan} = 0$ (dark) and $v_x^{scan} =$

$-v_x^{flow}$ (light), with widths representing two points on the curve in (b). (Inset) Example autocorrelation curve derived from data. (This figure is adapted from reference [33]).

To measure γ, n scans will be taken and $\ln\left\{\left|\frac{g(n\tau_0)}{g(\tau_0)}\right|\right\} = \gamma^2(n^2-1)\tau_0^2$ to eliminate β, the delta-correlated noise, from $|g(\tau)| = \beta e^{[-(\gamma\tau)^2]}$, where $2 \leq n \leq 8$. The article uses 8 scan biases to fit the curve.

This method could solve the blood flow velocimetry with good accuracy. However, it is not suitable for eye's blood flow velocimetry clinical practice. As 8 OCTA biases are applied, 9 OCT scans are required at the same sample position. Assuming an 80 kHz scanning rate (the maximum scanning rate before SNR drops rapidly as shown in Figure 2-29), then 0.11ms is taken to complete each A-line. Assuming a typical 4 s total integration time based on clinical practice, there are 4 s/0.11 ms = 36363 A-lines to be completed. Assuming a typical 15μm scan spot size and a square FOV, the completable FOV is then $\left(\sqrt{36363} \times 15/2\right) = 1430\ \mu m \times 1430\ \mu m$, which is less than the clinical requirement (at least 3.3 mm×3.3 mm).

While most OCTA models assume axial flow, real biological tissues involve multidirectional motion. This section presents a transverse velocity estimation method based on decorrelation asymmetry and bias detection.

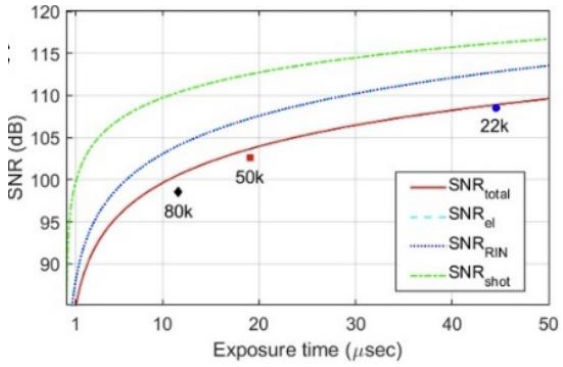

Figure 2-29. SNR variation as a function of exposure time. (This figure is adapted from reference [34]).

2.3.8 Limitation of OCTA Blood Flow Velocimetry Method

The OCTA blood flow velocimetry model, whether based on SSADA or OMAG, encounters challenges when the flow has a Doppler angle greater than 0 degree. For SSADA, the decorrelation value is affected by an additional component due to this Doppler angle. OMAG, however, has not yet been thoroughly studied yet in past studies. Nevertheless, we could still conduct analysis based on the analytical model in [18].

Examining the basic OMAG signal formation as described in [18]:

$$I_{OMAG} = \sqrt{(A(t)^2 + A(t+\Delta T)^2)[1 - g_1(\Delta T)\cos(\Delta\phi(t))]}, \quad (2\text{-}29)$$

the OMAG signal includes a normalized electric field autocorrelation function, $g_1(\Delta T) = A(t+\Delta T)A(t)\rangle/\langle A(t)A(t)\rangle$, which is influenced by the Doppler angle, as demonstrated in [31]. Here, $A(t)$ and $A(t+\Delta T)$ are the time-varying random amplitudes at interscan time t and $t+\Delta t$. This statement will also be covered in a later section of this thesis. Consequently, whether using SSADA or OMAG, a non-zero Doppler angle will always contribute to measurement inaccuracies in blood flow velocimetry.

The scan bias method for blood flow velocimetry can bypass the influence of the non-zero Doppler angle. However, this method has its limitations, as it requires a large number of scans to acquire sufficient data for building the fitting model, making it impractical for clinical imaging. Therefore, addressing the influence of the non-zero Doppler angle in OCTA blood flow velocimetry models is of greater importance and will be discussed in a subsequent section of this thesis.

To conclude this section, we summarize the main limitations of current velocity models in OCTA, including sensitivity to AVG, motion artifacts, and difficulties in absolute quantification.

2.4 Deep Learning Based Super-Resolution

Deep learning-based super-resolution techniques have shown promise in enhancing the resolution of medical images. These methods use convolutional neural networks (CNNs) to learn high-frequency details from low-resolution images. Self-supervised learning, where the model learns from the data itself without needing paired high-low resolution images, is particularly useful for medical applications where such paired data is scarce.

2.4.1 Deep Learning Fundamentals

Deep learning, a branch of machine learning, uses multi-layered artificial neural networks to analyse complex data such as images, audio, and text. These networks are inspired by biological neural systems and consist of input, hidden, and output layers [35]. Each neuron processes inputs and passes outputs to the next layer, enabling the network to learn patterns through hierarchical transformations. The input layer receives raw data (e.g., image pixels), hidden layers extract features, and the output layer generates predictions like classifications or

numerical values [36]. This structure is illustrated in Figure 2-30.

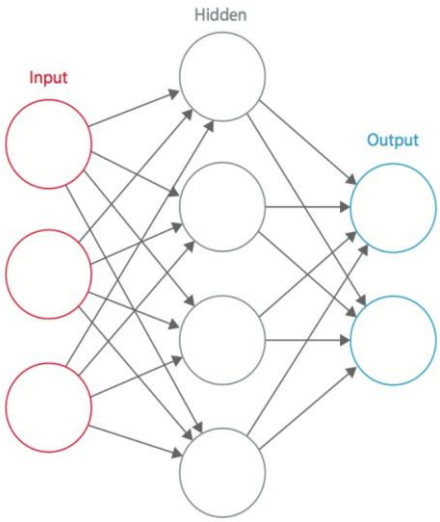

Figure 2-30. Basic Structure of an Artificial Neural Network (This figure is adapted from reference [37])

Activation functions play a crucial role in introducing non-linearity into the network, enabling it to learn and represent complex patterns in the data. Common activation functions include ReLU (Rectified Linear Unit), which outputs the input if it is positive and zero otherwise; the sigmoid function, which maps inputs to a range between 0 and 1; and the hyperbolic tangent (tanh), which maps inputs to a range between -1 and 1 [35]. ReLU is illustrated in Figure 2-31.

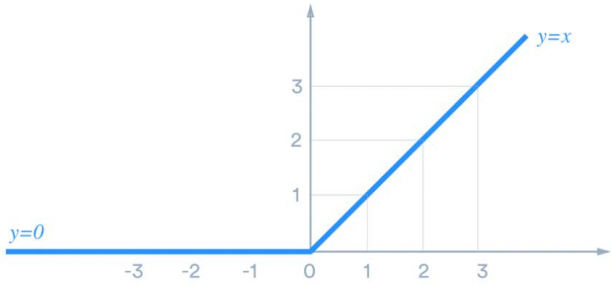

Figure 2-31. ReLU is defined as $y = max\ (0, x)$ (This figure is adapted from reference [38])

Neural networks learn by adjusting weights and biases for each neuron. Weights control input importance, while biases help shift the activation function for better data fitting. The learning process minimizes a loss function, such as Mean Squared Error (MSE) for regression or Cross-Entropy Loss for classification [36]. Training is performed using optimization algorithms like Stochastic Gradient Descent (SGD) or Adam, which update parameters via backpropagation. Gradients of the loss with respect to each parameter are computed and adjusted in the direction that reduces error [35].

CNNs are specialized for image processing and include three main layers: convolutional, pooling, and fully connected layers [39]. Convolutional layers use filters to extract spatial features (e.g., edges, textures), controlled by parameters such as filter size, stride, and padding [36]. Pooling layers, like max pooling, reduce spatial dimensions to lower computation and prevent overfitting. Fully connected layers integrate extracted features to produce the final output [39]. An early CNN architecture, LeNet-5, consists of input, convolutional, pooling, and fully connected layers. Designed for 32×32 grayscale images, it demonstrated the effectiveness of CNNs for image recognition tasks [40].

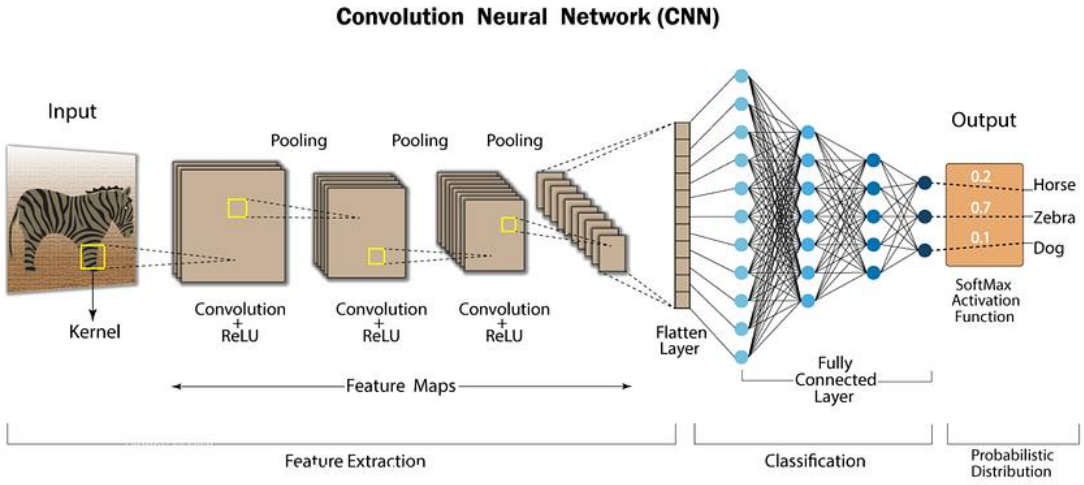

Figure 2-32. CNN architecture (This figure is adapted from reference [41])

In forward propagation, input data moves layer by layer through the network, with each neuron applying an activation function and passing outputs onward. Backpropagation adjusts weights and biases to minimize the loss function by computing gradients and updating parameters via optimization algorithms like SGD or Adam [35].

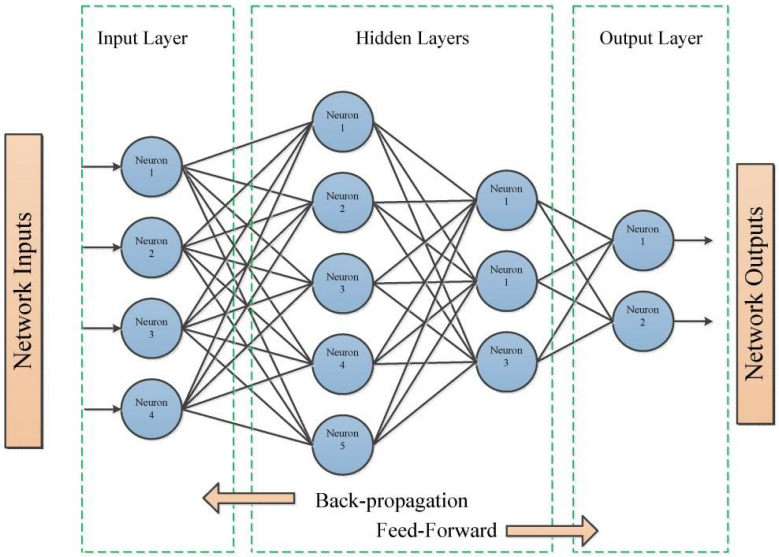

Figure 2-33. Feedforward and back propagation artificial neural network (ANN) (This figure is adapted from reference [42])

An epoch is one full pass through the training data, while batch size defines how many samples are processed at once. Smaller batches update more frequently; larger batches offer more stability [35]. To prevent overfitting, regularization techniques like L2 regularization and Dropout are commonly used. Model performance is assessed using metrics such as accuracy, precision, recall, and F1-score [35]. Transfer learning enables models pre-trained on large datasets to be fine-tuned for new tasks with limited data, improving efficiency and performance [43].

Deep learning's ability to learn features automatically has revolutionized imaging. It enhances resolution and quality in Magnetic Resonance Imaging (MRI), Computed Tomography (CT), and X-rays, supports astronomical image analysis, and improves resolution in fluorescence, optical, and electron microscopy [43]. These capabilities have enabled breakthroughs in imaging detail once thought unattainable.

Shifting to resolution enhancement, we begin with the fundamentals of deep learning, introducing key architectures and training principles used in modern image processing tasks.

2.4.2 Deep Learning Method for Super-resolution

Super-resolution microscopy enables imaging beyond the diffraction limit, traditionally achieved through techniques like structured illumination microscopy (SIM), stochastic optical reconstruction microscopy (STORM), and stimulated emission depletion microscopy (STED). While effective, these methods often require complex optics, specific fluorophores, and

intensive reconstruction, limiting their accessibility [43].

In contrast, deep learning offers a data-driven approach to super-resolution without detailed modelling of the imaging system. Techniques using Generative Adversarial Networks (GANs) have shown strong performance in enhancing microscopy images, transforming low-resolution inputs into high-resolution outputs without prior knowledge of the PSF.

A GAN consists of a generator and a discriminator trained together (Figure 2.34). The generator learns to produce high-resolution images, while the discriminator distinguishes them from real ones. Over time, the generator becomes adept at creating realistic super-resolved images [43], [44].

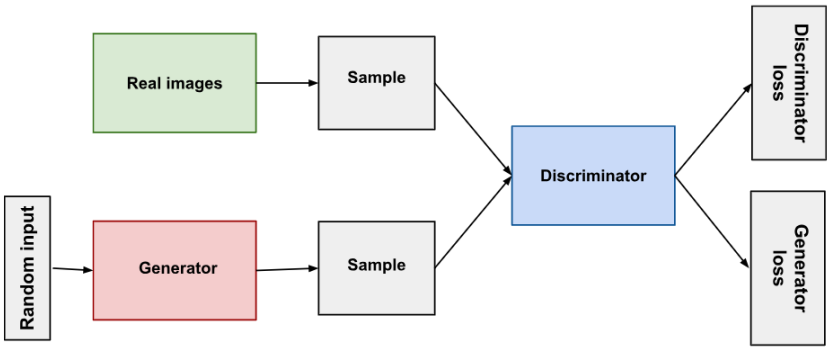

Figure 2-34. the overall structure of the GAN (This figure is adapted from reference [45])

Wang et al. demonstrated the use of GANs for cross-modality super-resolution in fluorescence microscopy by training on paired low- and high-resolution images. The method was successfully applied to wide-field, confocal, and total internal reflection fluorescence (TIRF) microscopy, achieving resolution comparable to high-numerical-aperture or STED systems [43], [46].

Compared to traditional methods like Lucy-Richardson deconvolution or non-negative least squares (NNLS), deep learning offers faster, non-iterative image enhancement without the need for parameter tuning [46]. GANs enabled images acquired with low-NA objectives to match the resolution of high-NA or STED images, revealing subcellular structures previously unresolved [43]. In scanning electron microscope (SEM), deep learning enhances resolution by learning from co-registered high-resolution images, reducing the electron dose and minimizing sample damage [43], [46]. Similar approaches in CT and MRI have improved

spatial resolution, aiding in more accurate diagnosis and treatment planning [43], [47].

Overall, deep learning–based super-resolution offers a hardware-efficient, versatile solution across imaging modalities, enhancing image clarity without complex setups or heavy post-processing. We then present the general concept of super-resolution using deep learning, where networks learn to map low-resolution images to high-resolution outputs, typically using paired data.

2.4.3 Enhanced Super-Resolution Generative Adversarial Networks (ERSGAN)

Traditional super-resolution (SR) methods often struggled with artifacts. The introduction of Super-Resolution GAN (SRGAN) improved image quality but still produced unnatural results. To overcome this, the Enhanced Super-Resolution GAN (ESRGAN) was developed, offering substantial improvements in perceptual quality [48].

ESRGAN improves upon SRGAN through three main changes: an updated architecture using Residual-in-Residual Dense Blocks (RRDB), improved adversarial loss, and refined perceptual loss. RRDB combines residual learning and dense connections, enabling deeper network training and better feature retention (Figure 2-35 and Figure 2-36). ESRGAN also removes Batch Normalization (BN) layers to avoid training–testing mismatch artifacts, resulting in sharper, more realistic images [48].

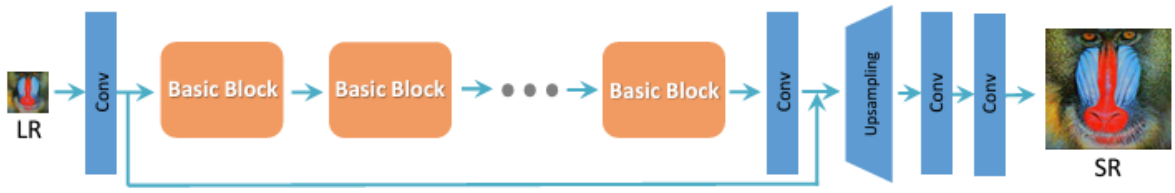

Figure 2-35. Network architecture for ESRGAN (This figure is adapted from reference [48])

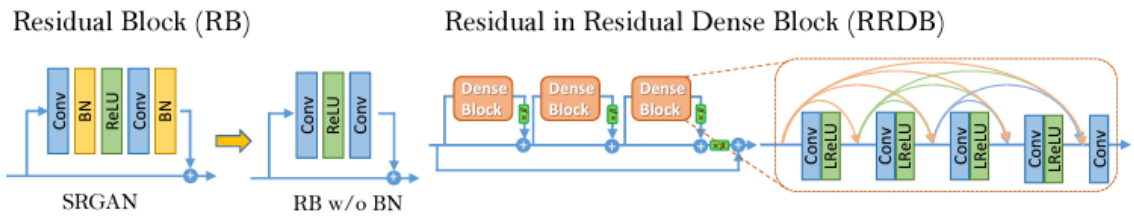

Figure 2-36. Architecture for RRDB (This figure is adapted from reference [48])

ESRGAN enhances image realism using a relativistic discriminator, which predicts how much more realistic a real image is compared to a generated one. This approach encourages the

generator to produce finer textures and sharper edges [48].

The model also improves perceptual loss by extracting features before activation layers in a pre-trained Visual Geometry Group (VGG) network, enabling better supervision and preserving complex structures and brightness details in super-resolved images [48]. Training ESRGAN involves a two-stage process: first, a PSNR-oriented model is trained with L1 loss for pixel-level accuracy; then, it is fine-tuned using adversarial and perceptual losses for visual realism. It was trained on large datasets like DIV2K and Flickr2K to capture diverse textures [48]. In benchmarks such as the PIRM-SR Challenge, ESRGAN outperformed previous methods in both visual quality and quantitative metrics, producing high-resolution images with enhanced textures and realism [48].

Traditional methods like bicubic interpolation and deconvolution (e.g., Richardson-Lucy) often fail to preserve fine details and may introduce artifacts [47], [49]. In contrast, deep learning-based approaches like ESRGAN learn complex mappings from data, generating high-quality outputs with realistic detail—essential in medical imaging, microscopy, and other high-precision fields [49], [50]. Comparisons are shown in Figure 2-37.

ESRGAN has been successfully applied in MRI, CT, and retinal imaging, improving resolution and aiding in more accurate diagnosis and treatment planning [47].

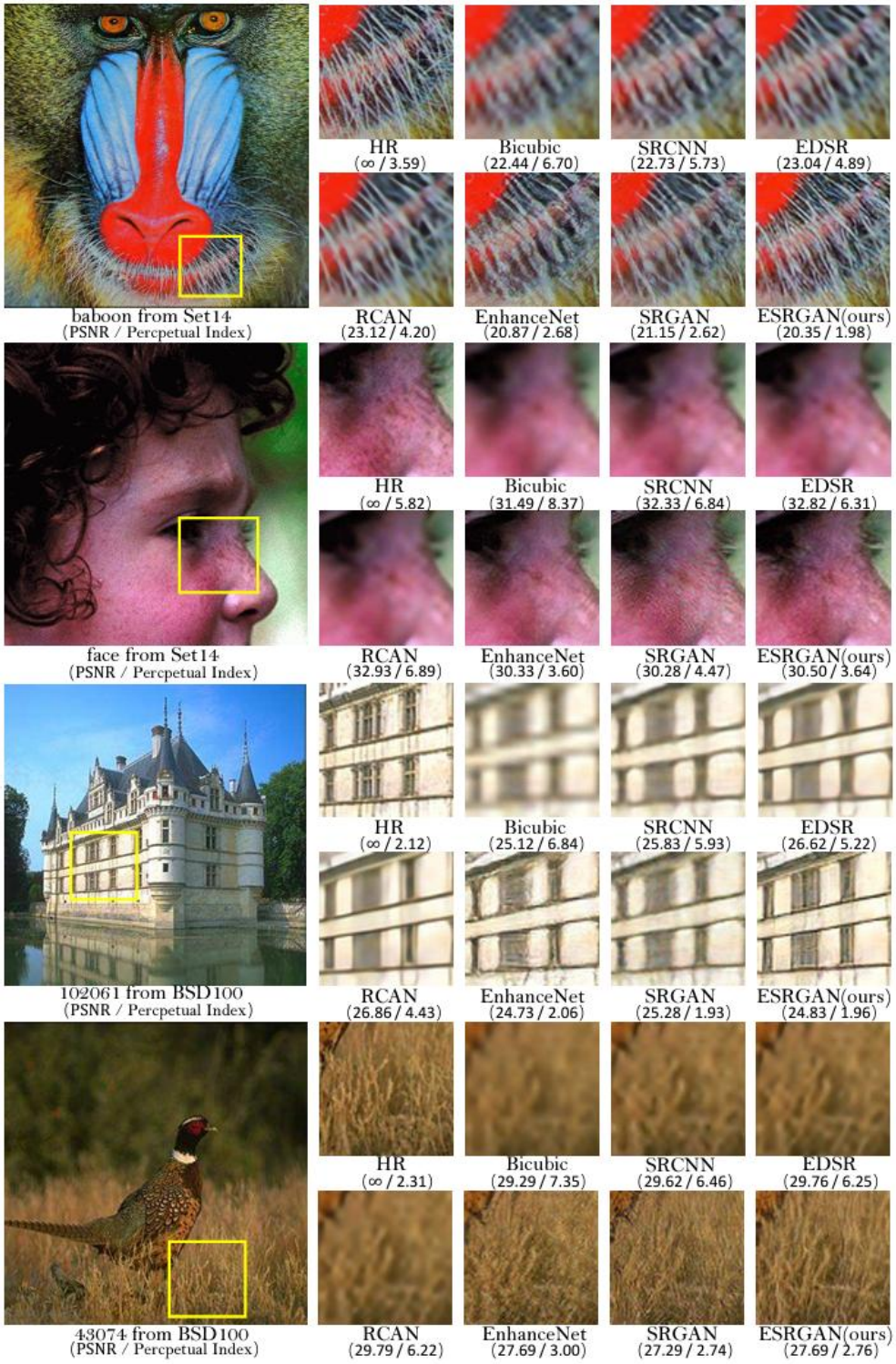

Figure 2-37. Qualitative results of ERSGAN (This figure is adapted from reference [48])

In microscopy, ESRGAN enhances fluorescence images to reveal sub-cellular structures not visible with traditional optics, supporting advanced biological research and diagnostics [51]. It is also used in astronomy to improve telescope image resolution, enabling clearer observation of distant celestial objects [52]. By combining architectural improvements, adversarial training,

and refined perceptual loss, ESRGAN delivers high-quality images with realistic textures and sharp details. Its strong benchmark performance and wide applicability have made it a leading tool for image super-resolution across various fields [53].

Among deep learning approaches, GANs have proven highly effective for realistic image reconstruction. This section explains the structure of ERSGAN and its enhancements over standard GANs.

2.4.4 Spectrum-based Deep Learning for Resolution Enhancement for OCT Image

Advancements in OCT technology—such as higher imaging speeds and wider fields of view—pose challenges in data acquisition, transfer, and storage. Spectrum-based deep learning has emerged as a promising solution, enhancing image quality while reducing data volume.

A notable approach involves learnable spectral–spatial sub-sampling in swept-source OCT, which jointly optimizes sub-sampling patterns and reconstruction using three neural networks: a mask generator, fringe reconstructor, and image enhancer. This method achieved a data compression ratio of up to 62.5× with minimal loss in image quality (~24.2 dB PSNR), validated on ex-vivo human coronary OCT datasets [52].

GAN-based methods, such as modified SRGANs, have been applied to recover spectral bandwidth and improve axial resolution. By simulating reduced A-scan resolution through spectral windowing, these models successfully reconstruct high-resolution features using transfer learning and data augmentation, especially for wide-field retinal OCT [53].

Another key development is neural network–based reconstruction from under-sampled spectral data, enabling high-quality OCT imaging with less acquisition time. This reduces motion artifacts and improves patient comfort while maintaining resolution and contrast [52], [53].

Collectively, these spectrum-based deep learning methods—whether through sub-sampling optimization, bandwidth recovery with GANs, or sparse-data reconstruction—offer substantial gains in resolution, efficiency, and diagnostic utility.

Future work should refine these approaches through better architectures, larger datasets, and real-time clinical integration. These innovations have the potential to transform OCT imaging, improving diagnostic accuracy and patient outcomes while streamlining clinical workflows. Instead of using image pairs, our approach focuses on spectral-domain data for self-supervised

learning. This section introduces the novel pipeline developed in this thesis, explaining how it overcomes common limitations of paired training.

2.4.5 Limitation of supervised spectrum deep learning

Most spectrum-based deep learning methods in OCT are supervised and focus on resolution recovery, requiring paired high- and low-resolution (HR–LR) images for training. This limits their adaptability and practicality, especially in clinical settings where HR data is difficult to obtain. These models also cannot exceed the system's native resolution and often require system-specific retraining.

In contrast, unsupervised methods offer greater flexibility. The self-super-resolution (SSR) approach by Zhuoqun Yuan et al. [54] uses only the system's own spectral data, avoiding the need for external HR references. Using Enhanced Spatial Residual Attention Module GAN (ESRAMGAN), it efficiently achieves super-resolution, highlighting the potential of self-supervised learning in OCT imaging.

While spectrum-based training offers advantages, it also introduces unique challenges. This section discusses these limitations, such as dependence on spectral quality and potential overfitting to noise patterns.

2.5 Biosensing Technologies for Skin Health Monitoring

2.5.1 Advances in Biochemical Monitoring for Skin Health

Wearable hydrogel patches have become key tools in biochemical monitoring, enabling non-invasive detection of biomarkers like pH, glucose, and lactate through interaction with skin excretions. Guo et al. (2024) [55] developed a photoacoustic (PA) system integrated with a pH-responsive Polyvinyl Alcohol and sucrose (PVA–Suc) hydrogel embedded with nitrazine yellow dye. This patch allows real-time, non-invasive wound pH monitoring, offering valuable insights into the healing process.

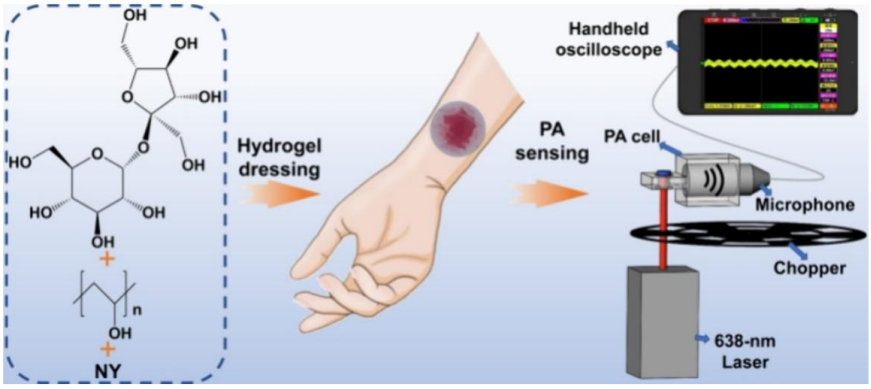

Figure 2-38. Working Principle of Portable PA Device Combined with PVA/Suc/NY Hydrogel Dressing for Point-of-Care Testing of Wound pH Values (This figure is adapted from reference [55]).

Figure 2-38 shows the working principle of the portable PA device, which integrates the PVA/Suc/NY hydrogel with a PA sensing system. Upon contact with wound exudate, the dye's optical properties change with pH. A 638-nm laser triggers the PA signal, which is detected by a microphone and analysed via a handheld oscilloscope, enabling rapid, point-of-care wound pH assessment [55].

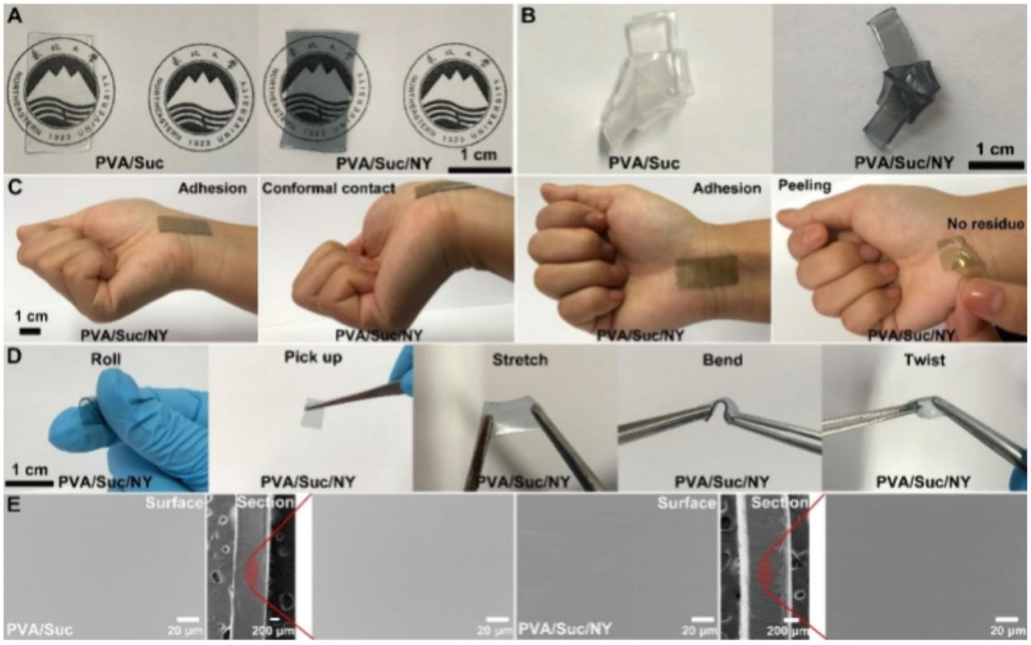

Figure 2-39. (A) Transmittance images of the PVA/Suc hydrogel and PVA/Suc/NY hydrogel. (B) Knotting ability of the PVA/Suc hydrogel compared to the PVA/Suc/NY hydrogel. (C) Adhesion of the PVA/Suc/NY hydrogel to human skin. (D) Flexibility of the PVA/Suc/NY hydrogel demonstrated through rolling, picking up, stretching, bending, and twisting. (E) SEM images showing the structures of the PVA/Suc hydrogel and PVA/Suc/NY hydrogel. (This figure is adapted from reference [55]).

Figure 2-39 highlights the properties and functionality of the PVA/Suc/NY hydrogel patch.

Panel (A) confirms its transparency, essential for PA sensing. Panel (B) shows its flexibility through knotting, while (C) demonstrates strong, residue-free skin adhesion. Panel (D) verifies robustness under mechanical stress, and (E) presents SEM images showing structural integrity and uniform dye distribution [55].

This PA-integrated hydrogel patch enables continuous, non-invasive pH monitoring, crucial for wound assessment. Its flexibility, transparency, and adhesion make it suitable for wearable use on moving skin. As shown by Guo et al., such patches hold great promise for real-time wound care and biochemical monitoring [55].

Monitoring skin pH is important, as deviations can indicate inflammation or microbial imbalance, common in conditions like dermatitis, eczema, and psoriasis. Early pH detection supports timely intervention [56].

Additionally, integrating liquid crystals (LCs) into hydrogels enables a new class of biosensors. These LC-embedded patches detect pH, glucose, and lactate through optical shifts caused by changes in LC orientation, offering sensitive, real-time biochemical monitoring.

Beyond imaging, monitoring biochemical parameters like pH and glucose is essential for comprehensive skin assessment. This section reviews recent advancements in non-invasive biochemical sensing technologies.

2.5.2 Liquid Crystal Biosensors for Real-Time Biochemical Monitoring

LC-based patches are highly suited for real-time skin diagnostics due to their sensitivity to biochemical changes. By detecting shifts in LC molecular orientation and optical properties, they provide early insight into skin conditions [56].

LC droplets respond to subtle molecular interactions, generating detectable optical signals without the need for labels. Their responsiveness makes them ideal for non-invasive monitoring of biomarkers like pH, glucose, and lactate [56].

The sensing mechanism relies on LC properties such as optical anisotropy, alignment transitions, and ultra-sensitivity to stimuli. Biochemical analytes can disrupt the "easy axis" alignment of LC molecules via electrostatic, hydrogen bonding, or ligand interactions, causing optical changes that amplify detection across a ~100 μm region. These alignment shifts, driven by changes in anchoring energy, are central to LC biosensing and remain an area of active study [56], [57].

A defining property of LCs is their optical anisotropy, resulting in birefringence. When plane-polarized light passes through an LC, it splits into two orthogonal rays, each experiencing a different refractive index: the ordinary (n_o) and the extraordinary (n_e) refractive indices. This difference leads to a phase shift, δ, which is expressed by:

$$\delta = \frac{2\pi d}{\lambda}(n_e - n_o), \qquad (2\text{-}30)$$

where d is the thickness of the LC layer and λ is the wavelength of the incident light.

The intensity I of transmitted light through crossed polarizers depends on the alignment of LC molecules and is given by:

$$I = I_0 \sin^2 2\phi \sin^2 \frac{\delta}{2}, \qquad (2\text{-}31)$$

where I_0 is the initial light intensity, ϕ is the azimuthal angle of the LC molecules relative to the polarizer axis.

When LC molecules align homeotropically (perpendicularly), they appear dark under crossed polarizers ($\delta = 0$), whereas other alignments produce bright fields. This anisotropic property enables detection of LC orientation changes through optical signals, with variations in brightness and colour observed under polarized optical microscopy (POM). These birefringence-driven changes provide a straightforward method for detecting orientation transitions in LC-based biosensors [56].

LC biosensors can be implemented in various configurations, each exploiting LC orientation transitions in response to biochemical interactions. The principal configurations of LC droplet are illustrated in Figure 2-40.

LC droplets dispersed in water offer a highly adaptable biosensing platform. The droplet's size influences alignment, with potential configurations including radial, bipolar, or pre-radial arrangements. As shown in Figure 2-40, adding surfactants can transition LC droplets from a bipolar to a radial configuration, enhancing sensitivity to biomolecular interactions. This droplet-based configuration is especially useful in applications requiring high sensitivity, as alignment transitions can provide real-time signals of target biomolecule presence [56].

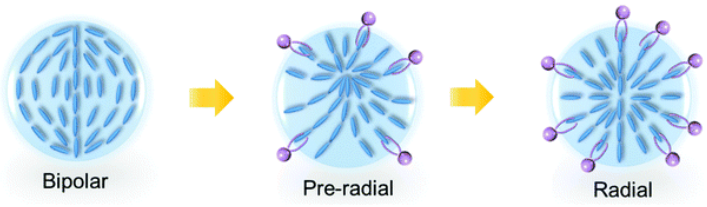

Figure 2-40. Schematic illustration of LC molecule orientation transitions. In LC droplets, alignment transitions from bipolar to radial with surfactant presence. (This figure is adapted from reference [56]).

In advanced applications, LC droplets are often doped with dyes or configured as whispering gallery mode (WGM) lasers to enhance sensitivity. In the WGM setup, LC droplets act as resonators, amplifying small environmental changes into significant optical shifts. This allows detection of target molecules at concentrations as low as picomolar levels, making LC biosensors highly effective for biochemical sensing [56].

LC biosensors are highly responsive to weak external stimuli, enabling them to amplify molecular interactions into detectable optical signals without complex equipment. They are effective in detecting a wide range of biological targets, including glucose, enzymes, ions, and other critical biomarkers, making them well suited for portable, real-time skin diagnostics [56].

Their sensing mechanism relies on LC properties such as optical anisotropy, alignment transitions, and high interfacial sensitivity. Molecular interactions—via hydrogen bonding, electrostatic forces, or ligand coordination—disrupt LC alignment, causing optical changes that propagate across a detection range of ~100 μm. These alignment shifts, triggered at the nanoscale, result from complex anchoring energy changes that remain an area of active research [56], [57].

LC biosensors have been used to monitor key biomarkers for skin diagnostics. PH sensing is crucial, as pH imbalance signals inflammation or microbial disruption, common in eczema, psoriasis, and dermatitis. Jang and Park [58] developed pH-responsive cholesteric LC droplets using microfluidics. These droplets exhibited optical shifts based on protonation changes in poly (acrylic acid)-functionalized surfaces, enabling precise pH monitoring on the skin.

Glucose monitoring is especially important for diabetic patients. Kim et al. [59] created LC droplets functionalized with glucose oxidase, which respond to glucose via enzymatic oxidation, altering pH and causing a radial-to-bipolar transition. Their system achieved a detection limit of 0.03 mM with a response time of ~3 minutes, offering a sensitive and cost-effective solution for diabetic wound care.

To assess oxidative stress, Zhou et al. [60] developed an LC platform that uses detection of glutathione (GSH)'s inhibitory effect on γ-glutamyl transpeptidase (γ-GT). Functionalizing the LC interface with cleavable surfactants enabled detection down to 1 pg/mL, supporting evaluation of chronic skin conditions and aging.

Acetylcholine (ACh), relevant to sweat secretion and wound healing, was targeted by Han and Jang [61] using an AChE-functionalized LC sensor on a nanostructured polymer. ACh hydrolysis triggered LC orientation shifts, with a detection limit of 10 nM, providing a tool for monitoring hyperhidrosis and healing processes.

For heavy metal ion detection, Amin et al. [62] incorporated BSA into LC droplets on DMOAP-coated surfaces, achieving 1 nM detection sensitivity. This allows precise monitoring of environmental toxins affecting skin health.

Further innovations include bio-electrostatic LC micro-lasers, explored by Wang et al. (2020) [57], where charged LC droplets in a WGM configuration detect biomolecules like proteins and nucleic acids via measurable wavelength shifts, with sensitivity down to 1 pM. These advances surpass traditional polarized optical microscopy in sensitivity.

LC droplet lasers have also been embedded into smart photonic labels, as demonstrated by Capocefalo et al. (2021) [63], enabling flexible spectral fingerprinting responsive to environmental changes. Additionally, LC microlenses, described by Xu et al. (2014) [64], offer fast response and mechanical stability, further enhancing the precision and adaptability of LC-based biosensors.

Among emerging technologies, LC-based biosensors are especially promising. This section discusses how liquid crystal droplets respond to biochemical stimuli and how these changes can be captured by OCT.

2.5.3 Limitation of Optical and Biochemical Techniques

Optical biosensors listed in section 2.5.2 have advanced biomolecule detection using spectroscopy and fluorescence, but they are limited to surface sensing and lack the depth-resolved imaging offered by OCT. Wearable hydrogel patches enable non-invasive biochemical monitoring via interaction with sweat or skin excretions, yet they typically lack structural imaging capabilities essential for a comprehensive assessment of skin health. Structural imaging helps visualize skin layer morphology and detect anomalies associated with disorders, complementing biochemical data. Currently, no system integrates OCT’s structural imaging

with biochemical sensing. Combining OCT with LC-doped hydrogel patches could provide a powerful tool to simultaneously assess both structural and biochemical skin features. This integration would enable real-time monitoring of inflammation, metabolic changes, and tissue integrity, improving diagnostic accuracy and supporting better management of complex skin conditions.

To conclude, we summarize the respective limitations of purely optical and biochemical approaches, highlighting the potential of combining them for multimodal diagnostics.

Chapter 3. : Axial Velocity Gradient Decoupling by Dual Beam OCTA

3.1 Background Introduction

Of particular significance for studying various retina pathologies is the measurement of retinal blood flow [5]. Doppler OCT method has been used for blood flow velocimetry, however, is also limited to such as its inability to directly measure the flow perpendicular to the scanning beam [65]. Besides, OCTA signals also correlate with blood flow velocity and can be used for blood flow velocimetry according to DLS theories [32]. OCTA offers the advantages over Doppler OCT as could measure flow perpendicular to the scanning beam directly [3]. Nevertheless, the Doppler angle, the angle between the scanning beam and the sample, influences the measurement accuracy [28]. An analytic model is formulated to attribute the dependence of autocorrelation on the Doppler angle to AVG [66]. This work further points out that it is not possible to accurately measure the velocity of particles from a single DLS measurement when AVG is present, but possible to apply repeated measurements to decouple the AVG contributions, like those with different optical resolutions or introducing a scanning bias [66].

Repeated measurements with different optical resolutions or introducing a scanning bias increases acquisition time for the same FOV regarding to the standard OCTA. In addition, the accuracy is subject to motion artefacts as both image position and apparent flow velocity might be altered by eye motion during repeated measurements. Few-Mode OCT (FM-OCT) leverages a novel modally-specific photonic lantern (MSPL) to generate two foci with different transverse point spread functions, corresponding to distinct optical modes: one from the fundamental Gaussian mode and the other from a higher-order non-Gaussian mode [67]. This difference in mode shapes may render existing analytical models inapplicable, potentially introducing errors. As a result, the theoretical framework requires further refinement to account for the mode-dependent discrepancies and ensure accurate interpretation of the measurements.

The purpose of this research is to provide a general yet low-cost solution to simultaneously imaging with two different optical resolutions. The requirements for the foci of the two beams for decoupling AVG are deduced following the previously established model [66]. Dual beam OCT system is then developed according to the requirements. The primary novelty of our study

lies in the application of a simpler and more cost-effective solution to eliminate the influence of AVG in OCTA blood flow velocimetry. The system requires only one spectrometer and off-the shelf optics, so that it costs much less than previous dual-beam or multi-beam solutions [10] [11] [12]. In addition, it does not rely on special optics (such as MSPL) and is generally applicable for any centre wavelength and spectral width. It is generally practical method and easy to repeat/reproduce.

3.2 Dual-Beam OCT

3.2.1 Method

3.2.1.1 Analytical Model for Decoupling

Generally, without normalization, the first order autocorrelation representing OCTA signal is given by [66]: $g^{(1)}(x,y,z,\tau) = \langle F(x,y,z,\tau)F^*(x,y,z,0)\rangle$, where F is the complex back scattering signal at the position (x,y,z), (x,y,z) denotes the position of the voxel of sampling. Assuming a Gaussian PSF, the first order autocorrelation could be further derived [66]:

$$\begin{aligned} g^{(1)}(\tau) &= exp[-i2nk_c v_{z0}\tau]\, exp\left[ink_c\left(\overrightarrow{v_0}\cdot\vec{\nabla}v_z\right)\tau^2\right] \\ &\times exp[-4n^2k_c^2 D\tau]\, exp\left\{-\frac{1}{2}\left[\chi_{xy}\frac{v_{zx}}{w_z}+\chi_{xy}\frac{v_{zy}}{w_z}+\chi_z\frac{v_{zz}}{w_z}\right]\tau\right\} \\ &\times exp\left[-\frac{1}{4}n^2k_c^2\left|\vec{\nabla}v_z\right|^2\tau^2\right] exp\left[-\frac{v_{x0}^2\tau^2+v_{y0}^2\tau^2}{w_{xy}^2}\right] exp\left[-\frac{v_{z0}^2\tau^2}{2w_z^2}\right], \end{aligned} \quad (3\text{-}1)$$

where D is the diffusive coefficient and $e^{-4n^2k_c^2D\tau}$ denotes the diffusion term, k_c is the centre wave number of the power spectrum and n is the refractive index. v_{x0}, v_{y0} and v_{z0} are the velocity components of the mean velocity in a single voxel, w_{xy} is the lateral resolutions in x and y direction and w_z is the axial resolution in z direction, and v_{zz} characterizes the axial velocity change per axial resolution. $\vec{\nabla}$ is the gradient operator, $\chi_{xy} = \ln(40/39)$ and $\chi_z = \ln(5/2)$ are factors that arise during an approximation approach in [66], and the mean voxel velocity $\overrightarrow{v_0}$ and the magnitude of a modified gradient operator $\left|\vec{\nabla}v_z\right|$ are defined as Eq. (3-2) [66].

$$\overrightarrow{v_0} = \left(v_{x0}, v_{y0}, v_{z0}\right), \quad (3\text{-}2)$$

$$\left|\vec{\nabla} v_z\right|^2 = \left(w_{xy}\frac{\partial v_z}{\partial x}\right)^2 + \left(w_{xy}\frac{\partial v_z}{\partial y}\right)^2 + 2\left(w_z\frac{\partial v_z}{\partial z}\right)^2.$$

By experimental results [66], only quadratic terms, $\exp\left[-\frac{1}{4}n^2k_c^2\left|\vec{\nabla} v_z\right|^2\tau^2\right]$ and $exp\left[-\frac{v_{x0}^2\tau^2+v_{y0}^2\tau^2}{w_{xy}^2}\right]exp\left[-\frac{v_{z0}^2\tau^2}{2w_z^2}\right]$, in $\left|g^{(1)}(\tau)\right|$ contribute much greater than the Doppler term $\exp[-4n^2k_c^2D\tau]$ and linear term $\exp\left\{-\frac{1}{2}\left[\chi_{xy}\frac{v_{zx}}{w_z}+\chi_{xy}\frac{v_{zy}}{w_z}+\chi_z\frac{v_{zz}}{w_z}\right]\tau\right\}$[66]. The dual beam OCT system uses two scanning beams of different beam sizes. Based on the simplified $\left|g^{(1)}(\tau)\right|$ in (3-3), the magnitudes of the autocorrelation signals, $|g_1|$ and $|g_2|$, can be expressed as Eq. (3-4). The contribution of AVG in the entire autocorrelation signal can be extracted from (3-3) as $g_{AVG} = exp\left[-\frac{1}{4}n^2k_c^2\left|\vec{\nabla} v_z\right|^2\tau^2\right]$. This AVG contributed autocorrelation term g_{AVG} ranges in (0,1]. Hence, ideally for a horizontal flow containing no AVG, $g_{AVG} = 100\%$. With defining $\alpha = w_{xy_1}^2/w_{xy_2}^2 = w_{z_1}^2/w_{z_2}^2$, the AVG terms of $|g_1|$ and $|g_2|^\alpha$ are equal according to Eq. (3-5). By setting $w_{xy}^2 = 2w_z^2$, $|g_{\text{aft}}|$ is a function of blood flow velocity without influence of AVG as Eq. (3-6).

$$\left|g^{(1)}(\tau)\right| \approx exp\left[-\frac{1}{4}n^2k_c^2\left|\vec{\nabla} v_z\right|^2\tau^2\right]exp\left[-\frac{v_{x0}^2\tau^2+v_{y0}^2\tau^2}{w_{xy}^2}\right]exp\left[-\frac{v_{z0}^2\tau^2}{2w_z^2}\right]. \quad (3\text{-}3)$$

$$|g_i| = exp\left[-\frac{1}{4}n^2k_c^2\left|\vec{\nabla} v_{z_i}\right|^2\tau^2\right]exp\left[-\frac{v_{x0}^2\tau^2+v_{y0}^2\tau^2}{w_{xy_i}^2}-\frac{v_{z0}^2\tau^2}{2w_{z_i}^2}\right], (i = 1,2), \quad (3\text{-}4)$$

$$\left|\vec{\nabla} v_{z_2}\right|^2\alpha = \alpha\left(w_{xy_2}\frac{\partial v_z}{\partial x}\right)^2 + \alpha\left(w_{xy_2}\frac{\partial v_z}{\partial y}\right)^2 + 2\alpha\left(w_{z_2}\frac{\partial v_z}{\partial z}\right)^2 = \left|\vec{\nabla} v_{z_1}\right|^2, \quad (3\text{-}5)$$

$$\left|g_{aft}\right| = \frac{|g_1|}{|g_2|^\alpha} = exp\left[-\frac{v_0^2\tau^2}{w_{xy_1}^2}(1-\alpha^2)\right]. \quad (3\text{-}6)$$

where the spatial derivatives of v_z are assumed to be constants.

3.2.1.2 Dual-beam OCT System and Experimental Setup

The dual beam OCT system is consisted of two Michelson interferometers sharing the same spectrometer Figure 3-1 (A). The light source (SUPERLUM M-T-850-HP) provides illumination over an 80 nm spectral width (2 of 3 channels switched off) centred at 850 nm. The light is guided by 50:50 fibre couplers. The two sample beams are aligned to be parallel with a 1.83 mm transverse displacement using a reflective mirror (RM). The collimated sample beam diameters are simulated to be 1.05 mm and 2.62 mm measured at 1% power level, respectively (Figure 3-1 (B)), and the ratios of the power loss due to the aperture division by

the pick-up mirror are simulated to be 9.97% and 8.67% respectively. The single-trip optical pathlength differences between the two sample beams is adjusted to be 1.2 mm. In the spectrometer, two input fibres are mounted with a V-groove with a spacing of 127 μm [70]. The collimated beams are dispersed by a 1765 lines/mm grating (PING-Sample-025, Ibsen photonics) and focused by a multi-element camera lens (focal length 176.8 mm) onto a line camera (EV71YO1SCL2010-BA3, Octoplus). The total photon-to-electron conversion efficiency of the spectrometer was measured to be 0.32, which includes the diffraction efficiency of the grating and quantum efficiency (~47%) of the camera sensor. The total ranging depth is 5.1 mm in air and the signal intensity roll-off is 2.68 dB/mm from DC to the -6 dB point. Spectra are digitized at 12-bit resolution and transferred to the computer through camera link cables and an image acquisition board (KBN-PCE-CL4-F, Bitflow).

Here in sample arm, we use H (light path: L5→L7) to represent the channel of the narrower illumination beam and L (light path: L6→L7) to represent the channel of the wider illumination beam. Then the bright field signals with larger and smaller beam sizes are associated with the OCT channel configurations as LL (light path: L6→L7→L6) and HH (light path: L5→L7→L5), and the dark field signal is associated with the OCT channel configuration HL (light path: L5→L7→L6 or L5→L7→L6). A Gaussian window (GW) is applied to the spectrum to satisfy $w_{xy}^2 = 2w_z^2$. As the object being sampled is 5% intralipid solution and human skin dermal tissues, the axial resolutions are measured with refractive indices of 1.43 (determined by the ratio of optical path lengths of the empty and filled tube) and 1.38 [71] respectively (Table 3-1). Both dark field signals are included into one single OCT channel due to identical resolution.

In our method, the spectrometer is equipped with two input fibres instead of the single fibre typically used in standard OCT spectrometers. Each fibre carries interference signals from one of the two reference arms. The tips of the two fibres are separated along the direction of the linear sensor with a spacing of 256 μm, ensuring that the linear sensor captures the full spectral range from both fibre tips. Consequently, there is a lateral shift between the two interferograms on the linear sensor, given by $256\,\mu m \cdot M$, where M is the magnification of the camera lens. In our spectrometer, this lateral shift corresponds to 70 pixels. This method is detailed in the study by Wang et al. (2023), which describes the implementation of multi-channel OCT using a single spectrometer [70].

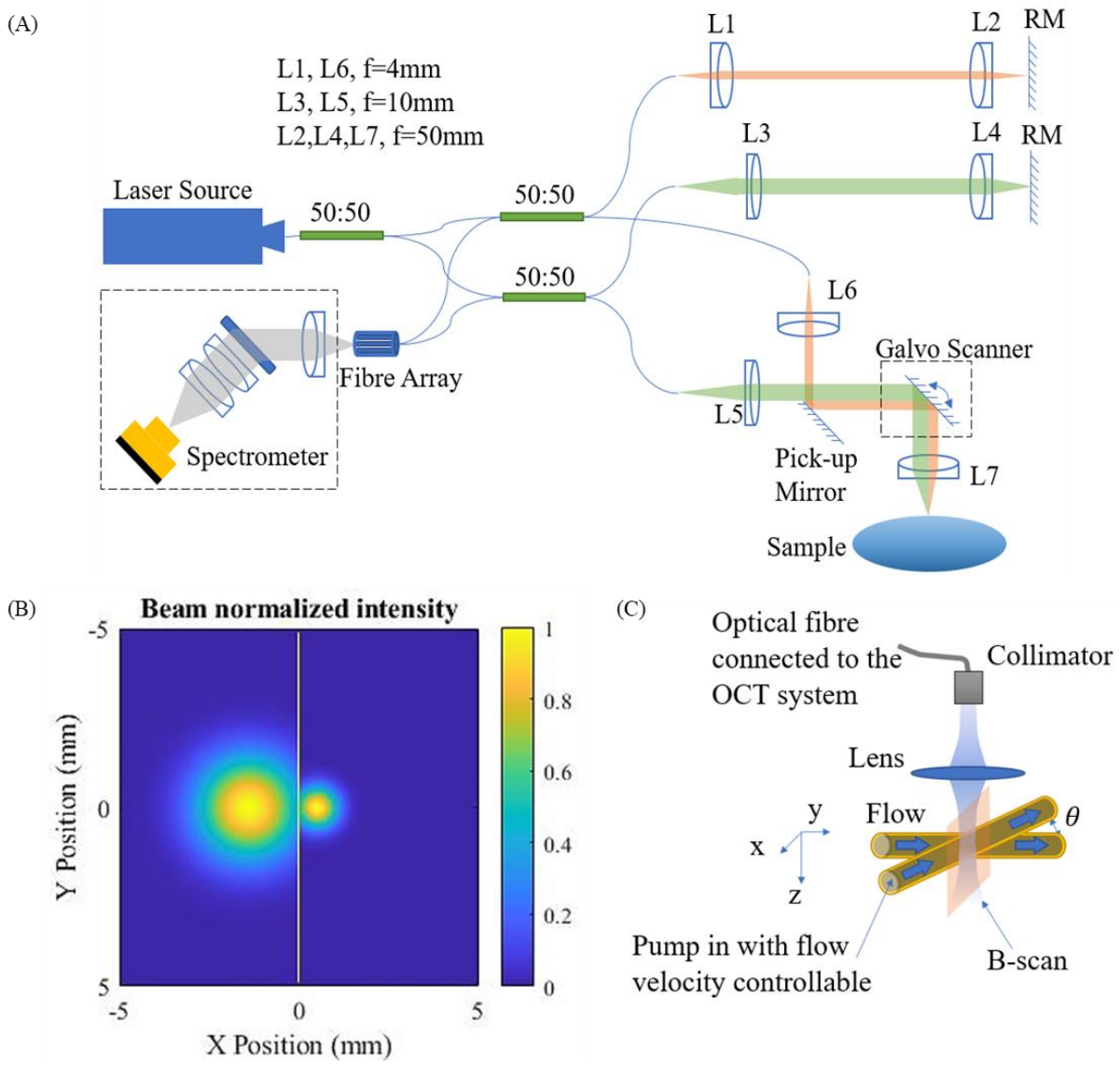

Figure 3-1. (A) The OCT schematic. RM: reflective mirror. f is focal length; (B) Normalized beam profile on the pick-up mirror in sample path with yellow line (x=0) marking the mirror edge position, (C) Phantom experiment design.

Table 3-1. (A) Spatial resolutions for OCT channels ($\alpha_{HH/HL} = \frac{w_{xyHH}^2}{w_{xyHL}^2}$ and $\alpha_{HH/LL} = \frac{w_{xyHH}^2}{w_{xyLL}^2}$).

OCT channel configuration	**w_{xy} (µm)**		**$w_z = w_{xy}/\sqrt{2}$ (µm)**		**α**
	Theoretical	**Measured**	**Theoretical**	**Measured**	
HH	**14.71**	**15.02**	**10.40**	**10.39**	/
HL	**19.31**	**19.40**	**13.65**	**13.68**	$\alpha_{HH/HL} = 0.58$
LL	**36.76**	**36.92**	**25.99**	**26.05**	$\alpha_{HH/LL} = 0.16$

(B) GW widths and respective measured axial resolutions

OCT channel configuration	Window Width (nm)	w_z (μm) in air	Window Width (nm)	w_z (μm) n=1.43	Window Width (nm)	w_z (μm) n=1.38
HH	**16.8**	**10.39**	**11.2**	**10.41**	**11.7**	**10.38**
HL	**11.3**	**13.68**	**8.5**	**13.62**	**8.8**	**13.64**
LL	**5.9**	**26.05**	**4.5**	**25.98**	**4.6**	**26.10**

The model is validated through a phantom experiment and a skin vasculature image experiment. In the phantom experiment as shown in Figure 3-1 (C), The blood flow is simulated by pumping (pump model: LSP01-2A) the intralipid solution (5% concentration diluted from 20% Sigma-Aldrich emulsion solution) with a predetermined flow rate in a glass capillary tube with internal diameter of 0.129 mm. θ is the inclination angle of the flow. The average flow speed is set as 0, 0.5, 1, 1.5, 2, 2.5 and 3 mm/s according to the flow rate and the nominal cross-sectional area of the tube lumen, and θ is set to be 0° and 30°.

To evaluate the available autocorrelation signal range for velocimetry, the dynamic range (DR) is defined referring to [31] [72] as the ratio between difference of the measurable average maximum and minimum autocorrelations ($\overline{A_{max}}$ and $\overline{A_{min}}$) and the standard deviation of the autocorrelation measurement. Based on the measurements on the average saturated autocorrelation $E(g_{saturate})$, the average autocorrelation value with 0 flow velocity $E(g_{offset})$ and the standard deviation of the autocorrelation values $std(g)$ of the data set g, DR is expressed as Eq. (3-7):

$$DR = 20\,log_{10}\frac{\overline{A_{max}}}{\overline{A_{min}}} = 20\,log_{10}\left(\frac{\left|E(g_{saturate}) - E(g_{offset})\right|}{std(g)}\right) \qquad (3\text{-}7)$$

The skin vasculatures at the palm side of the proximal interphalangeal joint of the middle finger in a healthy human subject is imaged. The optical power incident on the skin is below American National Standards Institute exposure limit for skin safety [73]. In the data processing for the skin vasculature image, only bright-field signals are used for a larger DR of decoupled signal based on the results in phantom experiment.

To evaluate the influence of AVG, the AVG contribution is defined from [28] as:

$$AVG\ contribution\ original = 100 \times \frac{||g_{\theta\neq0^\circ}|-|g_{\theta=0^\circ}||}{0.5\times(2-|g_{\theta\neq0^\circ}|-|g_{\theta=0^\circ}|)}, \qquad (3\text{-}8)$$

where $g_{\theta\neq0^\circ}$ and $g_{\theta=0^\circ}$ represent the original autocorrelation signal obtained for blood flow at non-zero and 0° inclination angle. Since this AVG contribution is calculated based on a single vessel with

same flowing speed by in different inclination angles, which is not feasible for real vessel in our case, we modify the AVG contribution as following:

$$AVG\ contribution\ modified \equiv 100 \times \frac{\left||g_{aft}|-|g_{bef}|\right|}{0.5\times(2-|g_{aft}|-|g_{bef}|)}, \quad (3\text{-}9)$$

where g_{bef} is the original autocorrelation signal before decoupling. In the modified version the same vessel before and after decoupling is evaluated. Since the difference in autocorrelation caused by inclination is only included in AVG term, g_{aft} is equivalent to the g_{bef} adjusted to 0° inclination angle. The phantom experiment data is firstly used to verify this modification before evaluating on in-vivo images.

g_{AVG} is also evaluated to validate the AVG influence. It is possible to use original autocorrelation signals measured in HH and LL channels, $|g_{HH}|$ and $|g_{LL}|$, to obtain g_{AVG} by following equations:

$$\begin{aligned} g_{AVG_{HH}} &= \frac{|g_{HH}|}{|g_{aft}|^{\frac{1}{1-\alpha^2}}} = \frac{|g_{HH}|}{\left(\frac{|g_{HH}|}{|g_{LL}|^{\alpha}}\right)^{\frac{1}{1-\alpha^2}}} = \left(|g_{HH}|^{-\frac{\alpha^2}{1-\alpha^2}}|g_{LL}|^{\frac{\alpha}{1-\alpha^2}}\right)|_{\alpha=0.16} \\ &= |g_{HH}|^{-0.026}|g_{LL}|^{0.164}, \end{aligned} \quad (3\text{-}10)$$

$$|g_{LL}| = g_{AVG_{LL}}\, exp\left[-\frac{v_0^2\tau^2}{w_{xy_{LL}}^2}\right] = g_{AVG_{LL}}\, exp\left[-\frac{v_0^2\tau^2}{w_{xy_{HH}}^2/\alpha}\right], \quad (3\text{-}11)$$

$$g_{AVG_{LL}} = |g_{LL}|\left(exp\left(\frac{v_0^2\tau^2}{w_{xy_{HH}}^2}\right)\right)^{\alpha} = |g_{LL}|\left(\frac{g_{AVG_{HH}}}{g_{HH}}\right)^{\alpha} = |g_{LL}||g_{HH}|^{-0.164}. \quad (3\text{-}12)$$

To relates g_{AVG} with AVG contribution modified (e.g. HH), we modify the AVG contribution as:

$$AVG\ contribution\ modified = \frac{\left||g_{aft}|-|g_{bef}|\right|}{0.5\times(2-|g_{aft}|-|g_{bef}|)} = \frac{\left(\frac{|g_{HH}|}{g_{AVG_{HH}}}\right)^{1-\alpha^2}-|g_{HH}|}{2-\left(\frac{|g_{HH}|}{g_{AVG_{HH}}}\right)^{1-\alpha^2}-|g_{HH}|} \times 2 \propto \frac{1}{g_{AVG_{HH}}}. \quad (3\text{-}13)$$

We employed MB scanning mode [19] at the A-line rate of 10 kHz for the phantom experiment. With 6 A-scans per image position, interscan time intervals (0.1, 0.2, 0.3, 0.4 and 0.5 ms) are achieved. We acquired 400 B-frames which are averaged to improve SNR. There were 128 A-

lines per B-frame with a transverse step size $\Delta w_{xy} = 4.36$ µm. The MB scanning mode was also employed in the skin experiment with an A-line rate of 5 kHz and 6 A-scans per image position yielding a 0.2 ms interscan time. There were 250 A-lines per B-frame and 250 B-frames per scan volume, so that the total acquisition time is 75 seconds. With 4.36 µm transverse step size, FOV is 1.125 mm × 1.125 mm. The total optical power on the sample is measured as 0.3 mW. Based on bright field signals detected by the spectrometer, the sensitivities are measured to be 101.29 dB and 101.00 dB for OCT channels of HH and LL respectively at 5 kHz A-scan rate (102.63 dB and 101.69 dB theoretically). The dark field signal sensitivity could be assessed by subtracting the signal difference between the bright field signal and dark field signal from the bright field signal sensitivity. Thereby, the dark field signal sensitivity is estimated to be 102.08 dB and 101.06 dB respectively. The -6 dB sensitivity roll-off in skin is measured as 1.77 mm.

3.2.2 Result

3.2.2.1 Phantom Experiment

As shown in Figure 3-2 (A & B), the decorrelation OCTA images of flow are obtained by SSADA algorithm [3] with interscan time (Δt) from 0.1 to 0.5 ms ($Decorrealtion = 1 - Autocorrelation$). The intensity of the decorrelation images from 0 to 1 is normalized into 0 to 255 grayscales. The second and third rows in Figure 3-2 (A & B) represent dark field signals created through different light paths. Although they have the same spot size and interscan time, the difference lies in the illumination and detection paths (L5→L7→L6 and L6→L7→L5), resulting in two distinct dark field signals encoded into separate rows. Only the upper half of the tube region (red D-shape region in Figure 3-2 (C)) is chosen for decorrelation measurement since the OCTA signal at the lower half of the tube region may not accurately reflect velocity due to multiple scattering artefacts. However, the decorrelation profile in x direction (Figure 3-2 (D)) does not match the finding in [74] which shows that the decorrelation drops from the lumen edge to the centre.

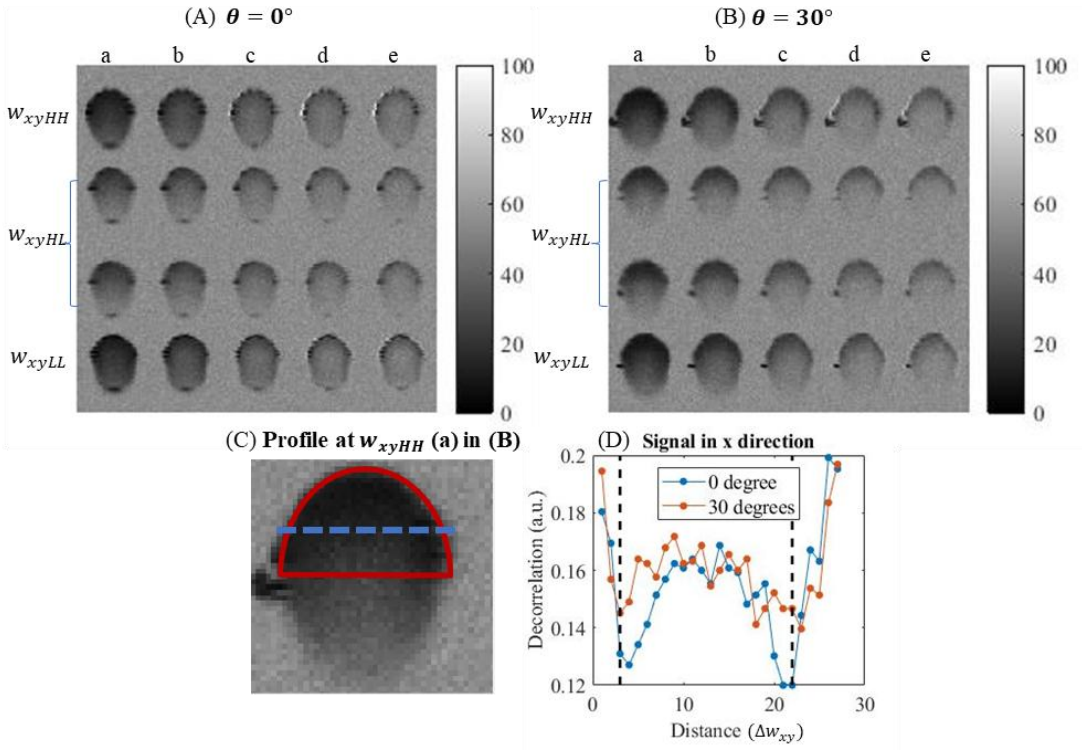

Figure 3-2. OCTA decorrelation images in x-z plane obtained when θ is 0° in (A) and 30° in (B), with 1 mm/s flow speed. Rows from top to bottom are of the 3 spot sizes $w_{xy_{HH}}$, $w_{xy_{HL}}$ and $w_{xy_{LL}}$. Column a-e: Δt = 0.1 ms, 0.2 ms, 0.3 ms, 0.4 ms and 0.5 ms. (C) D-shaped upper region for data analysis. (D) Flow profile in the horizontal direction along the blue dashed line in (C). Vertical dash lines in (D) mark the position of capillary tube inner edge. 'Distance (Δw_{xy})' refers to the lateral distance in the image, measured in units of step size Δw_{xy}.

For each of the experimental conditions shown in Figure 3-2 (A & B) (angle, interscan time and beam size), the decorrelation signals in the D-shape region of each cross-sectional image are averaged, and this averaged 5 decorrelations is again averaged over 400 cross sectional images. We assume g_{bef} is the original averaged autocorrelation signals acquired and g_{aft} is the averaged decoupled autocorrelation signals, then $g_{bef|30°}$ and $g_{aft|30°}$ are for $\theta = 30°$ and $g_{bef|0°}$ and $g_{aft|0°}$ are for $\theta = 0°$ respectively, which are measured in Figure 3-3 and Figure 3-4. The comparison between $g_{bef|30°}/g_{bef|0°}$ and $g_{aft|30°}/g_{aft|0°}$ verifies the effect of decoupling as shown in Figure 3-5 with offset decorrelation (when no flow is applied) subtracted. The ratio $g_{bef|30°}/g_{bef|0°}$ is averaged over all the interscan time and flow velocities (v_0) to be 0.9900, 1.0118 and 0.9935, and standard deviations 0.0123, 0.0147 and 0.0090 for HH, HL and LL configurations (Table 3-1) respectively, which agree with Eq. (3-2) that AVG magnitude is proportional to spot size. $g_{aft|30°}/g_{aft|0°}$ is theoretically to be 1, while is measured with mean values 0.9975 and 0.9977, and standard deviations 0.0027 and 0.0068

for case $\alpha_{HH/HL}$ and $\alpha_{HH/LL}$ for all interscan time and flow velocities, leading to an uncertainty of 0.7% based on the maximum standard deviation. Comparing to $g_{bef|30°}/g_{bef|0°}$, $g_{aft|30°}/g_{aft|0°}$ has its mean values averagely closer to 1 with standard deviations at least 2 times lower.

By Eq. (3-6), $g_{aft|0°}$ and $g_{aft|30°}$ are monotonically decreasing for an increasing flow speed and interscan time (as shown in Figure 3-4). Based on Figure 3-3, the decorrelation signals are found to reach saturation level when interscan time reaches 0.4 ms and above and flow velocity reaches 3 mm/s. To further assess DR in Figure 3-6, the data originally presented in Figure 3-3 and Figure 3-4 is reorganized to consider the product of interscan time and flow velocity, termed as the interscan distance. Based on Eq. (3-7), the DR are measured in Table 3-2. The DR is measured 1.84 dB higher for the lower α value ($\alpha_{HH/LL}$).

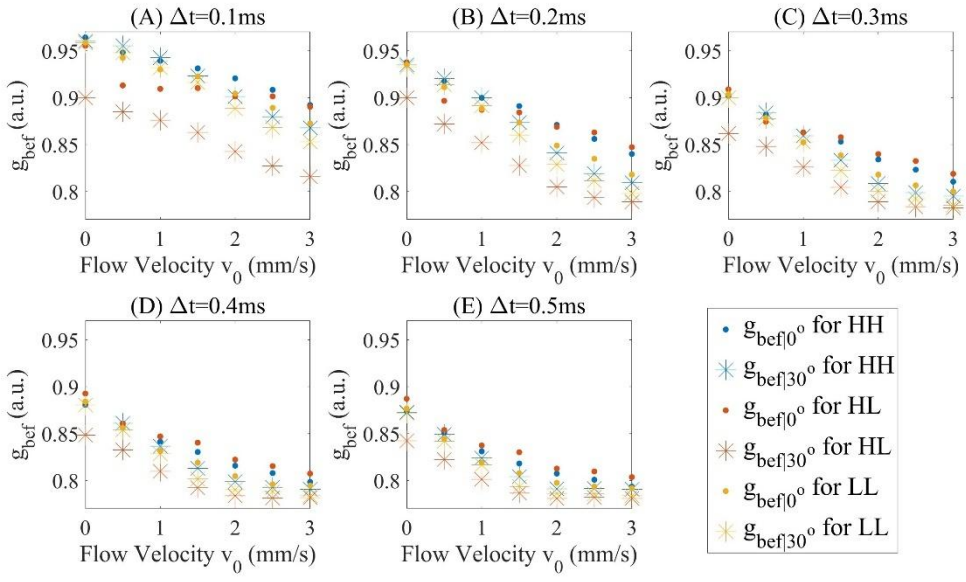

Figure 3-3. $g_{bef|0°}$ and $g_{bef|30°}$ at interscan time (Δt) (A) 0.1 ms, (B) 0.2 ms, (C) 0.3 ms, (D) 0.4 ms and (E) 0.5 ms.

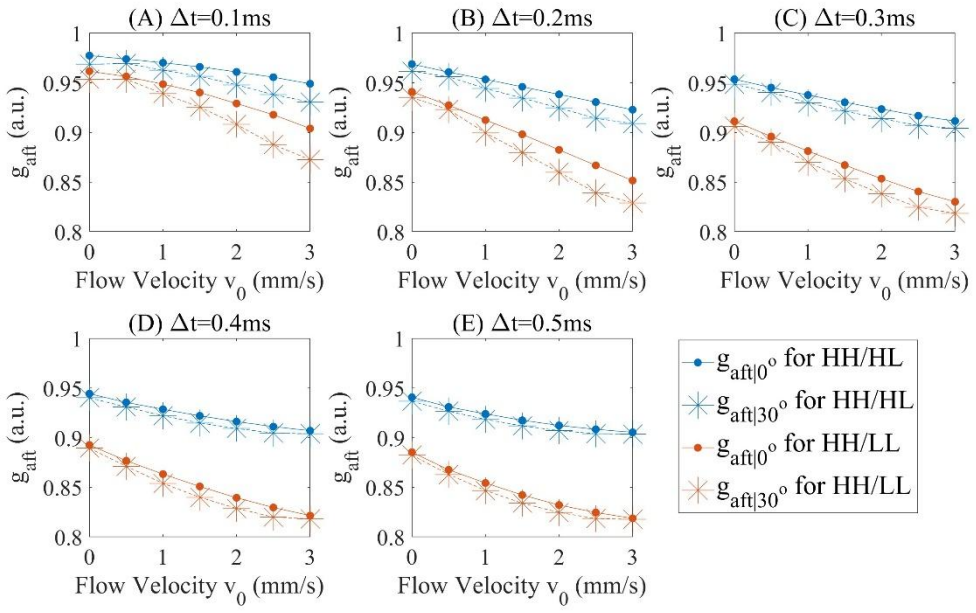

Figure 3-4. $g_{aft|0°}$ and $g_{aft|30°}$ at interscan time (Δt) (A) 0.1 ms, (B) 0.2 ms, (C) 0.3 ms, (D) 0.4 ms and (E) 0.5 ms.

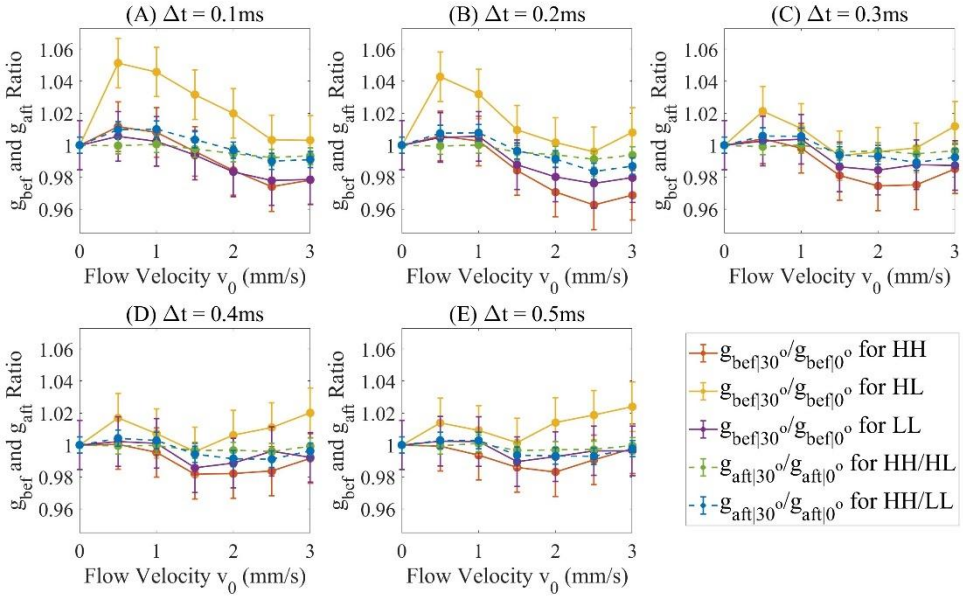

Figure 3-5. Comparative analysis for decoupling at interscan time (Δt) (A) 0.1 ms, (B) 0.2 ms, (C) 0.3 ms, (D) 0.4 ms and (E) 0.5 ms. Error bars indicate standard deviation.

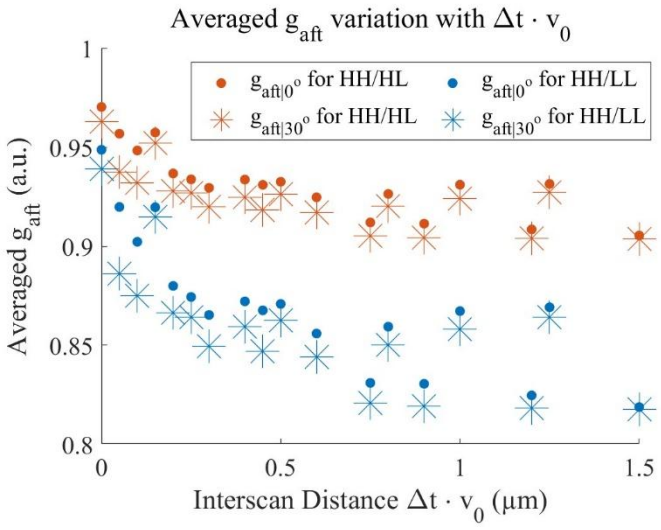

Figure 3-6. Average $g_{aft|0°}$ and $g_{aft|30°}$vs interscan distance ($\Delta t \cdot v_0$).

Table 3-2. DR Measurements for (A) $g_{aft|0°}$

Channel configuration used in decoupling	$E(g_{saturated})$	$E(g_{offset})$	std(g)	DR(dB)
HH/HL	**0.905**	**0.970**	**0.013**	**13.98**
HH/LL	**0.819**	**0.949**	**0.011**	**21.45**

(B) $g_{aft|30°}$.

Channel configuration used in decoupling	$E(g_{saturated})$	$E(g_{offset})$	std(g)	DR(dB)
HH/HL	**0.903**	**0.963**	**0.018**	**10.46**
HH/LL	**0.818**	**0.939**	**0.015**	**18.13**

(C) $g_{bef|0°}$.

Channel configuration	$E(g_{saturate})$	$E(g_{offset})$	std(g)	DR(dB)
HH	**0.806**	**0.929**	**0.010**	**21.80**
HL	**0.810**	**0.888**	**0.010**	**17.84**
LL	**0.810**	**0.935**	**0.010**	**21.86**

(D) $g_{bef|30°}$.

Channel configuration	$E(g_{saturate})$	$E(g_{offset})$	std(g)	DR(dB)
HH	**0.786**	**0.912**	**0.014**	**19.06**
HL	**0.801**	**0.874**	**0.014**	**14.34**
LL	**0.787**	**0.915**	**0.014**	**19.28**

3.2.2.2 Skin vasculature imaging

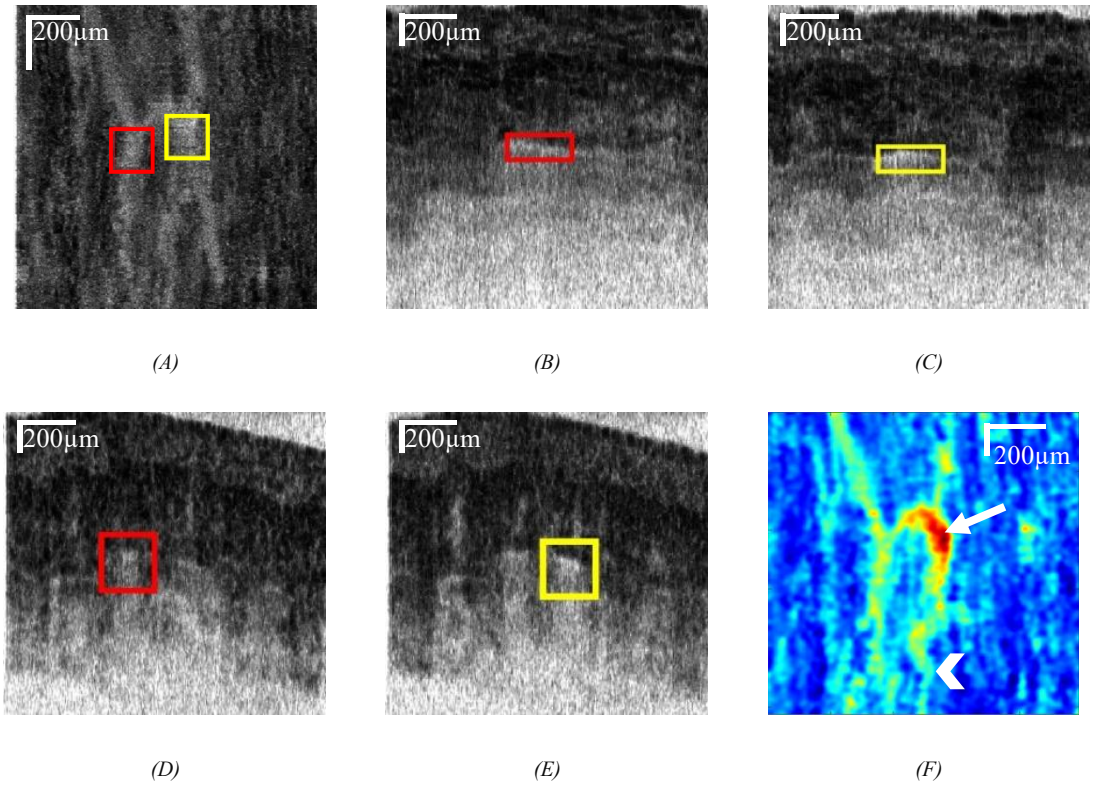

Figure 3-7. (A) En-face OCTA images of blood vessel in the skin in-vivo including a vessel with $\theta = 15°$ (red box) a vessel with $\theta = 0°$ (yellow box). (B) and (C) are images in y-z plane and x-z planes, corresponding to the red box in (A) respectively, and (D) and (E) are images in y-z plane and x-z corresponding to the yellow box respectively. (F) is the relative flow velocity map for $|g_{aft}|$, where white arrows point to vessels with high flow speed (red region), and white chevrons point to vessels with slow flow speed (blue-green region). Field of view: 1.125 mm × 1.125 mm, and depth of field: 1.1 mm.

In the OCTA images of the skin, we identified two blood vessel segments (Figure 3-7 (A ~ E)) aligned along the x axis. The relative flow velocity map is presented in Figure 3-7 (F). One segment is 15° inclined with respect to the x-y plane (Figure 3-7 (B & C)), and the other approximately perpendicular to the input beam ($\theta = 0°$) (Figure 3-7 (D & E)). We measured the inclination angle of blood vessels by outlining the brightest pixels in the vessel (the vessel path included in the red box in Figure 3-7 (B)), fitting a straight line in the x-z plane, and measuring the angle between this line and the horizontal direction, with the assumption that the short vessel segment under investigation is straight and the tissue average refractive index is 1.38. Background signal (location marked by the blue line in Figure 3-7 (B)) is subtracted before decoupling process. For convenience, only signals acquired by light spots with sizes of $w_{xy_{HH}}$ and $w_{xy_{LL}}$ are considered for a greatest DR.

The transverse decorrelation profiles of the above-mentioned two vessel segments are plotted in Figure 3-8. The denominator in the decoupling equation (Eq. (3-6)), $\left(|g_{bef}|\ for\ LL\right)^{\alpha}$, is not equal to 1. To address this, we normalized the intensity by aligning the mean values of the images in the LL and HH channels. Specifically, we multiplied the mean values to ensure that the mean image intensity of $1-|g_{aft}|$ matches $1-|g_{bef}|$ for both LL and HH channels in the $\theta = 0°$ case. Table 3-3 provides a summary of the measurements from Figure 3-8 and presents the average change in normalized autocorrelation due to decoupling, denoted as Δg. Given that the AVG is present in the signal when $\theta = 15°$, the Δg value for $\theta = 15°$ is expected to be higher than that for $\theta = 0°$ after decoupling. The measurement for Δg is 4.17 times higher for $\theta = 15°$ than $\theta = 0°$ by w_{xyLL}, with the uncertainty (measured by standard deviation) of Δg being 2.8 times greater. By w_{xyHH}, Δg is 5 times higher with an uncertainty 4 times greater for $\theta = 15°$ compared to $\theta = 0°$. Since Δg for w_{xyHH} is lower than w_{xyLL}, the AVG influence on images with higher transverse resolution is smaller, which agrees with Eq. (3-2).

The phantom experiment data is used to validate our modified AVG contribution model by $\frac{AVG\ contribution\ original}{AVG\ contribution\ modified}$ which results in 0.9967 and 0.9953 for HH and LL with $|g_{aft}|$ normalized. The evaluation results are presented in 3rd column of Table 3-3. Comparing to AVG contribution in the study [28], where their AVG contribution is approximately 8% for 15° inclination referring to their Figure 5 and their calculation (9.9% for 30° inclination), ours are 45.6% for LL and 8.8% for HH for 15° inclination. According to $\left|\vec{\nabla} v_z\right|^2 = \left(w_{xy}\frac{\partial v_z}{\partial x}\right)^2 + \left(w_{xy}\frac{\partial v_z}{\partial y}\right)^2 + 2\left(w_z\frac{\partial v_z}{\partial z}\right)^2$, the AVG is greater for a lower resolution, which agrees with our experimental results.

g_{AVG} could be calculated for both HH and LL in-vivo images respectively. Our g_{AVG} measurements for LL and HH with 15° inclination are 0.918 and 0.986, while the above study has $g_{AVG} = 0.987$ for Doppler angle 15° (obtained by $\frac{|g_{15°}|}{|g_{0°}|} = \frac{1-0.158}{1-0.144} = 0.987$), which matches the finding of AVG contribution part.

The primary aim of the proposed dual-beam system is to decouple the AVG contribution from the decorrelation signal in OCTA, thereby improving the accuracy of blood flow velocity estimation. Unlike methods focused on enhancing axial resolution or system sensitivity, this approach directly addresses a major source of error in flow quantification.

As shown in Table 3-3, the dual-beam method yields significantly more accurate velocity measurements when compared with the single-beam reference, with average error reduced to 0.7% in phantom experiments. This validates the effectiveness of AVG decoupling and supports the method's clinical applicability for more reliable flow imaging.

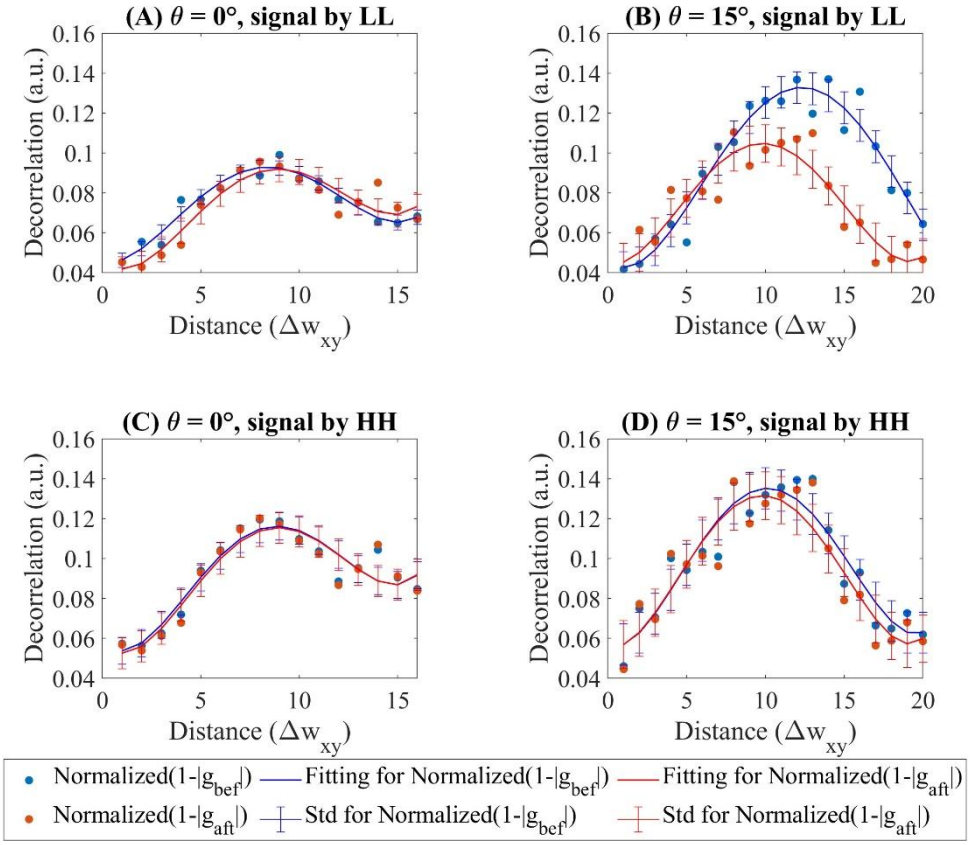

Figure 3-8. The normalized decorrelation profile acquired for the flow in Figure 3-7 of both before and after decoupling for (A) $\theta = 0°$ for signal acquired by LL, (B) $\theta = 15°$ for signal acquired by LL, (C) $\theta = 0°$ for signal acquired by HH and (D) $\theta = 15°$ for signal acquired by HH. Distance (Δw_{xy})' refers to the lateral distance in the image, measured in units of transverse scan step size Δw_{xy}. SD is standard deviation in short.

Table 3-3. The normalized autocorrelation before ($Normalized(|g_{bef}|)$) and after ($Normalized(|g_{aft}|)$) decoupling (mean ± standard deviation), measured AVG contribution (mean) and g_{AVG} (mean).

θ	channel	$Normalized(\|g_{bef}\|)$	$Normalized(\|g_{aft}\|)$	AVG contribution	g_{AVG}
0°	LL	0.925 ± 0.015	0.926 ± 0.018	0%	1.000
15°	LL	0.905 ± 0.032	0.923 ± 0.025	40.0%	0.918
0°	HH	0.908 ± 0.021	0.909 ± 0.022	0%	1.000
15°	HH	0.902 ± 0.030	0.906 ± 0.030	8.8%	0.986

3.3 Two Central Wavelengths

3.3.1 Method

The 2 resolutions by 2 central-wavelengths method are acquired by the addition of digital GW onto the spectrum obtained from the digital data. The imaging system is a general SD-OCT system. The method is only evaluated through the phantom experiment with the same setup as in the 1st method.

The SD-OCT system is consisted of a Michelson interferometer. The light source (SUPERLUM M-T-850-HP) provides illumination over an 230nm spectral width centred at 850nm. The focal lengths for illumination lenses are 10 mm and objective lenses are 30 mm. In intralipid, the transverse and axial resolution with full spectrum is measured to be 9.01 μm and 3.36 μm. As shown in Figure 3-9, when added with two Gaussian windows central at 815 nm and 890 nm with spectral widths of 22.7 nm and 23.4 nm, the measured transverse resolutions are $w_{xy_1} = 8.64\ \mu m$ and $w_{xy_2} = 9.44\ \mu m$, and axial resolutions are 6.10 μm and 6.66 μm. The α values calculated for transverse and axial resolutions are 0.94 and 0.84. The average α is then 0.87. As a comparison, another two Gaussian windows central at 776 nm and 950 nm with spectral widths of 30.0 nm and 24.1 nm., the measured transverse resolutions are $w_{xy_3} = 35.2\ \mu m$ and $w_{xy_4} = 41.0\ \mu m$, and axial resolutions are 5.71 μm and 8.34 μm. The α values calculated for transverse and axial resolutions are 0.74 and 0.47. The average α is then 0.60. These two α values are noted as α_1 and α_2.

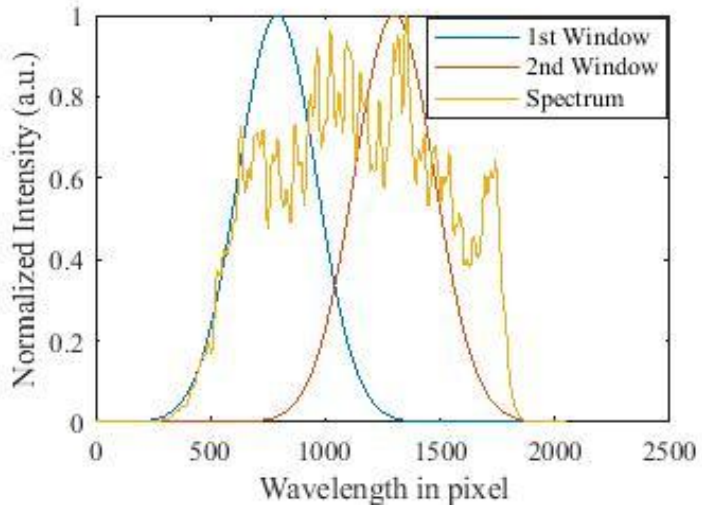

Figure 3-9. Gaussian windows added onto the spectrum.

3.3.2 Result

In the 2 central wavelength method, the results are shown in Figure 3-10. The ratio D_{30}/D_0 is averaged over all the inter-scan time and flow velocities to be 1.2865, 2.9687, 1.2572 and 2.1107, and standard deviations 0.3167, 48.9452, 0.4916 and 16.1473 for all w_{xy_1} to w_{xy_4}. By Eq. (3-6), the averaged decoupled autocorrelation signals g_0 and g_{30} ($g_\theta = \frac{|g_1|}{|g_2|^\alpha}|_\theta$, where $\theta = 0°$ or 30°.) are monotonically decreasing for an increasing flow speed and interscan time (as shown in Figure 3-4), which is valid except α_1 at 0.1ms interscan time with a observed maximum dynamic range about 0.021 at 0.5ms interscan time. g_{30}/g_0 is measured with mean values 1.0044 and 1.0041, and standard deviations 0.0015 and 0.0023 for case α_1 and α_2 for all interscan time and flow velocities, leading to an uncertainty of 0.2% based on the maximum standard deviation. Comparing to D_{30}/D_0, g_{30}/g_0 has its mean values averagely closer to 1 with standard deviations at least 138 times lower. Based on the observation above, the second method is not applicable to the velocimetry due to a too small $|\Delta g|$ ($\max|\Delta g| = 0.008$) even though it successfully decouples the AVG influence.

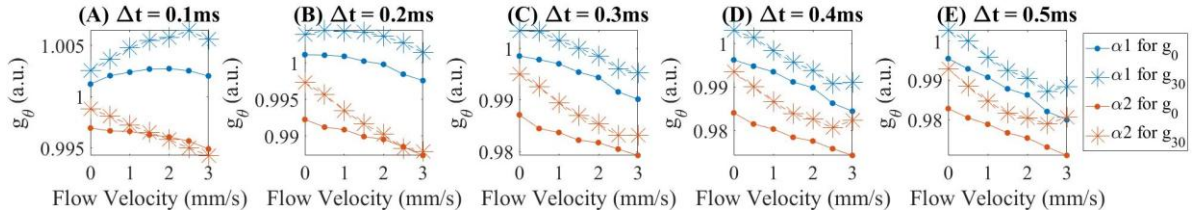

Figure 3-10. Signal records when the average pre-set flow velocity is varying from 0 to 3mm/s with both α values ($\alpha_1 = 0.87$ and $\alpha_2 = 0.60$) for g_0 (decoupled autocorrelation signal when $\theta = 0°$) and g_{30} (decoupled autocorrelation signal when $\theta = 30°$) at interscan time (Δt) (A)0.1ms, (B)0.2ms, (C)0.3ms, (D)0.4ms and (E)0.5ms.

3.4 Discussion

It is known that the slope of the autocorrelation signal is inversely proportional to the spot size, which holds true in the decoupled autocorrelation signal. Based on Eq. (3-6), an equivalent transverse spot size of decoupled decorrelation signal w_{aft} can be derived as Eq. (3-14):

$$w_{aft} = \frac{w_{xy_{HH}}}{\sqrt{1-\alpha^2}} = \sqrt{\frac{w_{xy_{HH}}^2 w_{xy_{HL}}^4}{w_{xy_{HL}}^4 - w_{xy_{HH}}^4}} \; or \; \sqrt{\frac{w_{xy_{HH}}^2 w_{xy_{LL}}^4}{w_{xy_{LL}}^4 - w_{xy_{HH}}^4}}. \qquad (3\text{-}14)$$

Accordingly, the equivalent transverse spot sizes for decoupled channel HH/HL and HH/LL are 18.06 μm and 14.90 μm. The corresponding difference in slope are well reflective in

Figure 3-4.

After decoupling, the DR is lower comparing to that before decoupling in general (Table 3-2). This is expected since the measurement uncertainty, which can be evaluated by the standard deviation $std(g)$, is higher due to error propagation in the decoupling process. One of the other observations is that the offset of dark-field (HL) decorrelation is significantly higher than those of the bright field (HH & LL). This is probably due to the higher random motion between the illumination and detection pin hole. This is one of reason we chose not to use dark-field signals to decouple AVG and measure blood flow.

In the context of imaging the skin vasculature, where both high-resolution (w_{xyHH}) and low-resolution (w_{xyLL}) spots share identical sampling densities (the same artifacts detected in [29] emerge in the images captured by w_{xyLL} as compared to those obtained by w_{xyHH}: the vessels, especially small vessels such as capillaries, will appear larger in the angiograms, and this may lead to a higher value when using a metric such as vessel density, the percentage area occupied by flow pixels on the OCT angiogram.

The A-line rate chosen for this study (5 kHz) is for convenience purpose only. Slow scanning system is vulnerable to a SNR drop due to fringe washout [75]. It also increases the total sampling time and easily saturates the images acquired for fast blood flow. Instead of MB mode scanning, repeated B-scan imaging protocols are normally applied to create OCTA images as less vulnerable to eye motion due to a shorter total sampling time. For artery and vein blood flow velocimetry (fast flow as shown in [76]), a high A-line rate is preferred, which is challenging to SD-OCT system due to significant sensitivity degradation beyond 80 kHz [34]. SS-OCT is a solution as the A-line rate up to 400 kHz while preserving a good sensitivity [2], but higher in cost. Nevertheless, other SD-OCT based fast scan method such as [20] is also suggested as lower system cost while SNR preserved solutions.

In this study, an A-line rate of 5 kHz was used primarily for experimental convenience. Although this rate is lower than those typically used in clinical SD-OCT systems—which generally operate between 20 kHz and 70 kHz—it offers the advantage of a higher SNR due to the longer integration time per A-line. As demonstrated in Figure 4(d) of SELF-OCT [34], increasing the A-line rate leads to a reduction in SNR, which is a well-recognized trade-off in OCT imaging. While the 5 kHz rate facilitates robust signal acquisition for experimental evaluation, it is not representative of clinical imaging speeds. In clinical applications, higher

A-line rates are preferred to minimize motion artifacts and improve imaging speed, albeit at the cost of reduced SNR. This trade-off between speed and image quality is an important consideration when translating research findings to practical, real-time clinical use.

The greater uncertainty observed in the in-vivo imaging results, compared to phantom experiments, is primarily attributed to limited data availability, increased scattering heterogeneity in biological tissue, and motion artifacts. These challenges are inherent to in-vivo OCT imaging. Although repeated acquisitions and simple averaging were used to reduce noise and suppress motion-induced variability, more advanced techniques may further improve image reliability. For instance, motion correction methods based on orthogonal scanning patterns [80], A-scan level correction [80], or image registration frameworks tailored for OCTA [81] have been shown to significantly mitigate motion artifacts in volumetric data. Additionally, real-time motion tracking or hardware-based stabilization can be considered in future system designs. Beyond motion correction, adaptive or model-based averaging strategies may help enhance signal robustness while maintaining spatial fidelity [82], [83]. Incorporating such methods in future implementations could reduce variability in clinical settings and improve overall image quality.

The standard deviation measured for decorrelation values before decoupling is not significantly different from the result in the previous study about HDR-OCTA (Figure 6 in [31]). Both Δg and the standard deviation (SD) mentioned in above study are normalized values. Hence after restoring from the normalized values, the original SD value of the HDR-OCTA study is not significantly different form our results. Hence, $\frac{SD(g)}{\Delta g}$ could exclude the influence of normalization where $\Delta g = E(g_{offset}) - E(g_{saturated})$. For HDR-OCTA, $\frac{SD(g)}{\Delta g} = \frac{0.06}{0.55} = 0.11$, and for our system, $\frac{SD(g)}{\Delta g} = \frac{0.014}{0.126} = 0.11$. The uncertainty measured for original decorrelation is similar to the HDR-OCTA under the same condition. The uncertainties in in-vivo images are larger than that of the phantom experiment. Firstly, it is due to the limited amount of data for averaging. Secondly, the GT value might possibly be varying during the image acquisition due to heterogeneity of the blood scattering behaviour and the hand motion.

A scan-bias method [33] employs 8 OCTA scan biases to fit three independent parameters for the curve of decay rate in OCTA signal versus scan-biased velocity. According to the analytical model, the corresponding scan velocity value equals the real flow velocity when the decay rate reaches its minimum. The AVG is included in one of these independent fitting parameters and

is bypassed when solving for the flow velocity. In comparison to this scan-bias method, our method exhibits several key differences:

(1) It requires only two scanning sessions at the same position to generate two OCTA images with distinct resolutions, using dual beams scanning simultaneously. Each session yields two OCT scans per beam, allowing construction of two OCTA images. In contrast, the scan-bias method requires nine scans to produce eight differently biased OCTA images. This makes our method significantly faster and less susceptible to motion artifacts during in-vivo imaging.
(2) The scan-bias method has only been validated using phantom experiments and may not be suitable for widefield in-vivo imaging due to its extended acquisition time.

The FM-OCT presented by Caroline Boudoux et al. utilizes a MSPL technique to detect back-scattered signals through two fibre modes. Due to the difference in mode-field distribution, theoretically, OCT signals of two modes can be used to cancel the AVG. In their conference presentation, the capability of AVG cancellation is demonstrated using flow phantoms, but no results with blood flow in-vivo are shown. The same group first reported FM-OCT using MSPL in a paper, which we can reference to explore the differences from our method in detail [84]. Compared with FM-OCT, our method are novelty following contents:

(1) AVG cancellation in our system is achieved through a centrosymmetric Gaussian mode-field, ensuring isotropic flow sensitivity regardless of vessel orientation. In contrast, the LP11 mode used in FM-OCT is non-centrosymmetric, leading to orientation-dependent decorrelation behaviour. As noted in their presentation, true 2D (x-y) velocity measurement requires three modes, which current FM-OCT systems do not provide.
(2) Although both methods are based on similar underlying physics, the detection schemes differ. We use bright-field detection in both channels, maximizing sensitivity. FM-OCT employs dark-field detection for the LP11 mode, which exhibits lower signal strength, especially in in-vivo settings where signal quality is critical. This sensitivity difference is evident in their published data.
(3) Our system is built entirely with commercially available components and supports common centre wavelengths (e.g., 850 nm, 1060 nm). In contrast, MSPL devices are custom-fabricated, limited to 930 nm, and their compatibility with broader bandwidths or other wavelengths remains uncertain. This restricts the scalability and accessibility of FM-OCT for routine clinical use.

The decorrelation is based on the dynamic back scattering (DBS) from the sample. Both DBS and dynamic forward scattering (DFS) are types of DLS, but DFS is immune to AVG, and more sensitive and linearly related to blood flow comparing than DBS [74]. However, DBS has an advantage over DFS when measuring on the flow in retinal vessels on the retinal pigment epithelium (RPE) layer. When measuring the flow in retinal vessels, DFS signal is acquired from the projection of the flow on the RPE layer, a layer below the retinal vessels highly scattering and avascular. Thus, the DFS is possibly unattainable for a less reflective RPE due to certain diseases, such as early age-related macular degeneration progression [85], or general less reflective RPE.

There are limitations of this design. First, the interferograms from HH, LL and HL paths have to be optical pathlength delay (OPD) encoded and separated to avoid overlapping the OPD domain, so that the effective ranging depth of interferograms of each path are much smaller than the total ranging depth. Second limitation is that the setup with double reference arms and single spectrometer introduces higher system shot noise [12][28] which is directly proportional to reference power. The number of shot noise electrons is given by:

$$\sigma_{shot}^2 = \frac{\rho\eta\tau}{h\lambda_0}\frac{P_0}{N}(\gamma_s R_S + \gamma_r R_r), \qquad (3\text{-}15)$$

where ρ is the efficiency of the spectrometer, comprising the diffraction grating efficiency and losses due to optical components, N determines the number of pixels of the line array CCD, and R_s and R_r are the reflectivity in the sample and reference arm of a Michelson interferometer, assuming $R_r = R_s = 1$ when characterizing the system. γ_r and γ_s are the part of the input power in each arm. P_0 is the total output power of the light source, including the power of all frequencies, and is evenly distributed to the N pixels. Since signals are received from 2 channels, they reach the CCD at the same time when guided into the spectrometer by the fibre array. Thus, 2 times the spectral bandwidth is widened on each pixel on the CCD. Then the shot noise is increased by $\sqrt{2}$ according to [70]. This limitation could only be solved by adding an extra spectrometer, then higher system cost needs to be considered.

Moreover, recent advancements in deep learning methods for image acquisition and processing, as demonstrated in the study by Liao et al. (2023), provide promising avenues for enhancing the accuracy and efficiency of OCTA [86]. Integrating such deep learning techniques with our current approach could further optimize the image acquisition process, leading to improved measurement accuracy and more robust validation of the decoupling method. This integration

will be a significant basis for future research, potentially opening new possibilities for the application of OCTA in clinical and research settings.

3.5 Conclusion

We introduce a method based on a dual beam OCT to decouple the AVG influence in OCTA for blood flow velocimetry. By choosing appropriate spot sizes of the two sample beams. We show the theoretical basis for cancelling the AVG term. Verification is carried out by both phantom and skin vasculature imaging experiments. By applying decoupling on the autocorrelation model, both phantom experiment and *in-vivo* imaging of skin vasculature demonstrated a reduction in influence attributable to AVG. These advancements offer valuable insights for interpreting blood flow velocities in clinical OCTA applications.

Chapter 4. : Spectrum-Based Training for OCT Axial Super-resolution

4.1 Background Introduction

Skin conditions affecting the stratum corneum and stratum lucidum, such as palmoplantar psoriasis and keratoderma, have received heightened attention due to their prevalence and impact on patient quality of life [11]. OCT imaging has become a widely used tool for diagnosing these skin issues, offering non-invasive visualization of skin layers [13] [85]. Achieving high axial resolution in OCT is essential for accurate diagnosis, particularly when observing subtle boundaries like those between the stratum corneum and stratum lucidum, which can reveal early signs of disease. For conditions such as psoriasis, eczema, and ichthyosis, where boundary clarity is essential, a higher axial resolution enhances diagnostic precision [11].

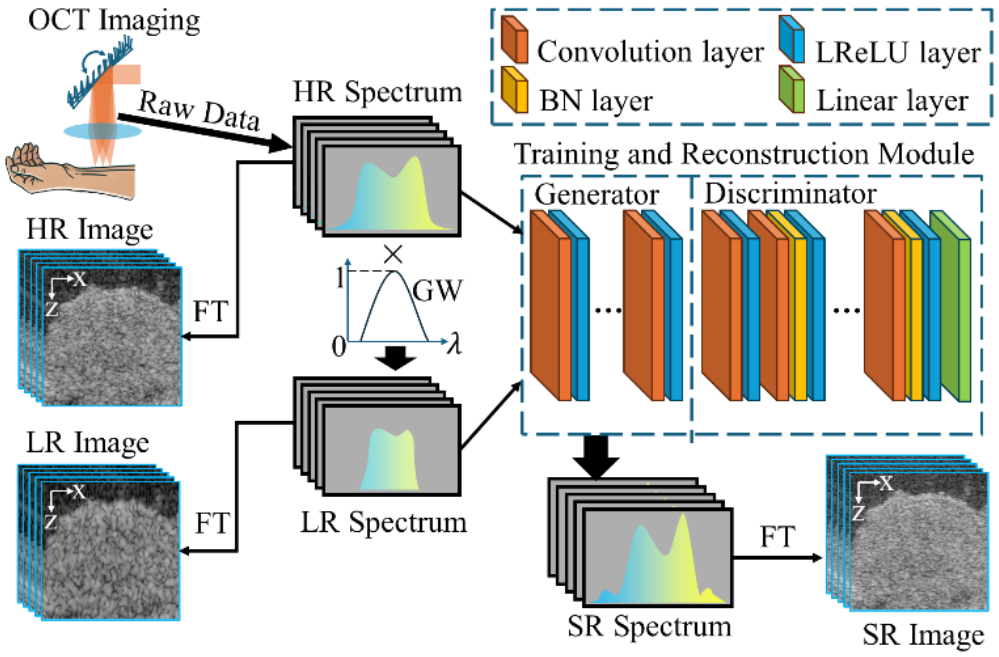

Figure 4-1. Schematic of axial super-resolution in OCT images via spectrum-based self-supervised training. The raw data acquired through OCT imaging consists of high-resolution (HR) spectra for training. By applying a GW to the HR spectra, we generate low-resolution (LR) spectra. Both the HR and LR spectra are then fed into the training and reconstruction module. The trained model is subsequently applied to the HR spectra to produce super-resolution (SR) spectra FT: Fourier Transform. BN: batch normalization. LReLU: LeakyReLU. ×: Multiplication. λ: wavelength.

Recently, deep learning has gained popularity for enhancing resolution in OCT images, offering a cost-effective alternative to traditional hardware-based methods while potentially surpassing the limitations of classical image processing techniques [87] [88] [89] [89] [90] [92] [93] Super-resolution, which achieves image resolution beyond the native limits of the input images [94], has been advanced through deep learning methods focused on image-based training [46] [95] [47] [43] [95] [96] [97] [99] [48] [49]. In OCT imaging, GAN-based models, particularly ESRGAN [48], have been adapted for enhancing image resolution [49]. Qiu et al. leveraged semi-supervised learning to bypass the need for low-high quality image pairs required by supervised networks [100]. The residual in residual dense block (RRDB) networks were successfully used for image-based deep learning (DL) training to obtain axial super-resolution [51], and conditional GANs improved the axial resolution while preserving realistic speckle patterns [101]. Additionally, GANs have been applied to enhance lateral resolution in OCT, such as refocusing *en-face* images [50].

However, these image-based approaches only utilize the intensity (magnitude) data derived from the Fourier-transformed OCT spectrum, which lacks phase information and limits the effectiveness in accurately reconstructing fine boundary details, such as those between the stratum corneum and stratum lucidum. In contrast, spectrum-based approaches incorporate the complete OCT spectral data, including phase information, into the training process, offering potential for more robust super-resolution capabilities. Despite this potential, spectrum-based methods have not yet achieved effective super-resolution [102] [53] [53] [104].

In this study, we introduce the axial super-resolution in OCT images via spectrum-based self-supervised training (as illustrated in Figure 4-1). The advantage of utilization of self-supervised deep learning approach is that it does not need prior knowledge of higher resolutions as reference [54]. the raw data acquired through OCT imaging consists of high-resolution (HR) spectra for training. By applying a GW to the HR spectra, we generate low-resolution (LR) spectra. Both the HR and LR spectra are then fed into the training and reconstruction module. The trained model is subsequently applied to the HR spectra to produce super-resolution (SR) spectra. Our framework yielded a 50% improvement in axial resolution, achieving 4.28 μm from 7.19 μm, along with PSNR gains of up to 3.37 dB and SSIM increases by 0.157, significantly enhancing boundary continuity and fine detail reconstruction.

We believe this method, directly training OCT spectral data to achieve self-supervised super-resolution, will open possibilities to enhance axial resolution and restore boundary continuity,

thereby advancing diagnostic accuracy.

4.2 Method

4.2.1 Super-resolution Network Structure

Here are the structures of the generator and the discriminator in Figure 4-2. The generator incorporates an architecture starting with a single initial convolutional block for initial feature extraction, followed by two middle convolutional (conv) blocks for further feature processing, each utilizing ReLU activation functions for introducing non-linearity. It concludes with a final convolutional layer aimed at generating the output image. The discriminator is designed as a sequential CNN, initiating with a convolutional layer for input processing, followed by three subsequent convolutional blocks. Each block doubles the feature depth while halving the spatial dimension through stride-2 convolutions, supplemented with BN and LReLU activation for non-linearity and training stability. The architecture finalizes a linear layer outputting a singular value to discriminate between real and synthetic spectrums.

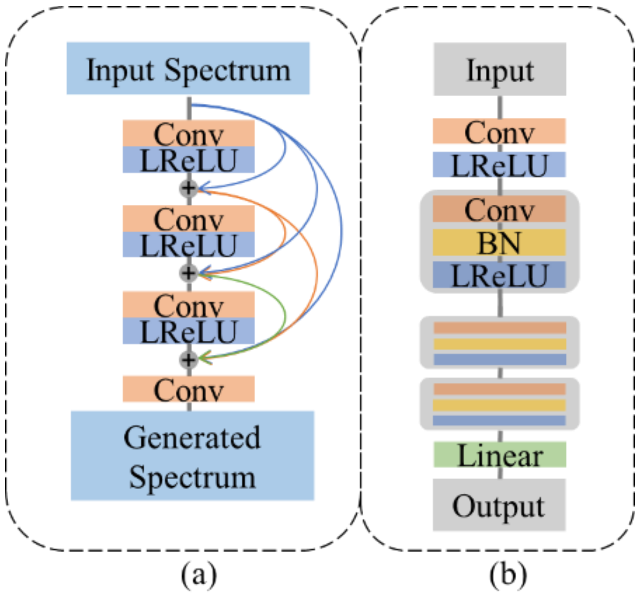

Figure 4-2. (a) Structure of generator, and (b) structure of discriminator

4.2.2 Framework of the Spectral Data Training and Data Preparation

The methodology for training spectral data and generating image data is delineated in Figure 4-3. Spectral data is initially collected using a custom-built SD-OCT system. This raw spectral data undergoes dispersion correction and is subsequently remapped into the k-space (frequency domain) as cited in reference [5], whereupon it is designated as the GT spectrum. Unlike in

Figure 4-1, where the HR spectrum directly consists of the raw data, here we require a GT as a reference for validation purposes. Therefore, we treat the raw data spectrum as GT, while the HR spectrum is obtained by applying a GW to the GT.

The GT spectrum serves as the global reference for all training inputs, as well as for the spectra generated by applying the trained models. In practical applications, however, we should follow the approach outlined in Figure 4-1, where the HR spectrum is directly derived from the raw data.

The GT spectrum is then subjected to two different GW to generate two distinct sets of spectra: HR and LR. The HR spectra, produced with a broader GW, have greater bandwidth than the LR spectra, which are generated using a narrower GW. Following this, the magnitude of all LR and HR spectra pairs are fed to the training process. Given that the phase information remains invariant under the application of GW, the phases from the HR spectra are retained and imposed onto the resultant SR spectra. These SR spectra are then transformed via Fourier transform to produce the final SR images.

During training, low-resolution (LR) spectra are input into the generator, which outputs spectra with widened bandwidth. The discriminator then receives either high-resolution (HR) spectra or generator-produced spectra and classifies them as “real” (HR) or “fake” (recovered from LR). Through backpropagation, the error between generated “fake” spectra and real HR spectra is calculated, guiding updates to the generator’s weights to minimize this error. This cycle repeats, with the generator progressively refining its output until the discriminator can no longer distinguish between real and recovered spectra. Training stops when criteria such as loss function stability or classification accuracy are met [104].

At the stopping point, training concludes when the discriminator becomes unable to differentiate between the generated spectra and the genuine HR spectra. The generated spectra are denoted as fake HR spectra.

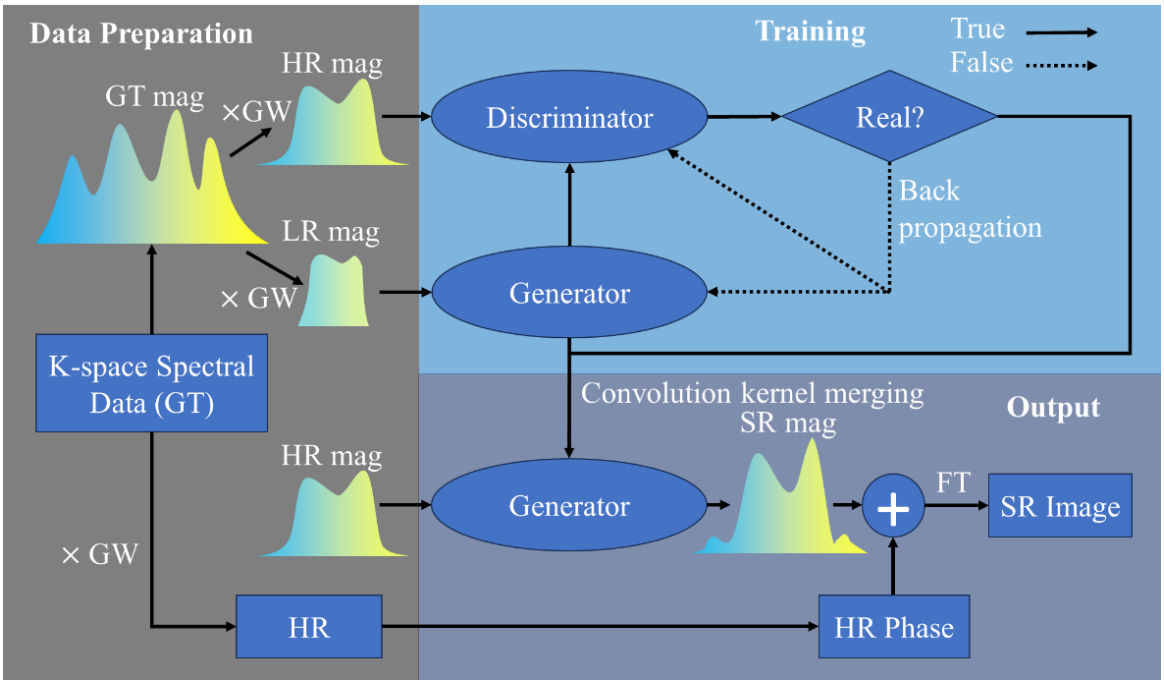

Figure 4-3. The workflow of the method. ×GW: applied with Gaussian window. mag: magnitude. FT: Fourier transform.

4.2.3 Evaluation Metrics and Loss Function

To assess our network's performance, we used two quantitative metrics: peak signal-to-noise ratio (PSNR), structural similarity index measure (SSIM) [105]. The metrics are evaluated with respect to GT images for the LR, HR, generated fake HR and generated SR images, and inspect how similar the target images are to the GT images based on pixel-to-pixel measurement and global structural measurement respectively.

The loss function designed for the generator is also based on a combination of PSNR and SSIM calculation as Eq. (4-1). Hence, the training process strictly follows the PSNR an SSIM constraint.

$$L_{combined}(output, GT) = -PSNR(output, GT) - SSIM(output, GT). \quad (4\text{-}1)$$

The loss function designed for the discriminator is calculated by binary cross-entropy loss [106] for both the real (HR) and fake (generated fake HR) outputs as Eq. (4-2).

$$L_{discriminator}(real, fake) = BCE(real, 1) + BCE(fake, 0), \quad (4\text{-}2)$$

where BCE is the binary cross-entropy loss, 1 is a tensor of ones and 0 is a tensor of zeros.

4.2.4 System Setup, Data Acquisition and Data Processing

The homemade SD-OCT system use a light source (SUPERLUM M-T-850-HP) which provides illumination over a 170 nm spectral width centred at 850 nm. The light is guided by a 90:10 fibre coupler to the sample and reference arms. The collimated beam is dispersed by a 1500 lines/mm grating (PING-1500, Ibsen photonics) and focused by a multi-element camera lens onto a line camera (EV71YEM4CL2010-BA8, E2V). The total photon-to-electron conversion efficiency of the spectrometer was measured to be 0.75, which includes the diffraction efficiency of the grating and quantum efficiency (~47%) of the camera sensor. The total ranging depth is 1.74 mm and the roll-off is 4.06 dB/mm from DC to the -6 dB point. Spectra are digitized at 12-bit resolution and transferred to the computer through camera link cables and an image acquisition board (KBN-PCE-CL4-F, Bitflow).

The mechanism of applying GW to control the axial resolution (Δz) is respect to $\Delta z = 2\ln 2 \cdot \lambda_c^2/\pi\Delta\lambda$, where λ_c is the central wavelength and $\Delta\lambda$ is the spectrum width. GW changes the $\Delta\lambda$, further modifies Δz [5]. The GW widths applied to acquire LR and HR spectra are 9.96 nm and 20.75 nm, then the axial resolutions are measured as 10.87 μm and 5.21 μm in air respectively, while the axial resolution for GT is measured as 2.55 μm in air. Taking refractive index 1.38 in skin [71], the axial resolutions for LR, HR and GT become 15.00 μm, 7.19 μm and 3.52 μm. The transverse resolution is 14.71 μm. We employed an A-line rate of 20 kHz for the *in-vivo* skin imaging. There are 512 A-lines per B-frame and 400 B-frames per scan volume, so that the total acquisition time is 10.24 seconds (400 data is for each data set). With 3.42 μm transverse step size, FOV is 1.75 mm × 1.37 mm. The total optical power on the sample is measured as 0.754 mW. Based on the signal detected by the spectrometer, the sensitivities are measured to be 107 dB. The 6 dB sensitivity roll-off in skin is measured as 0.53 mm (refractive index 1.38 for skin [71]).

The skin in the forearm region close to the wrist of healthy human subjects is imaged. The optical power incident on the skin is below American National Standards Institute (ANSI) exposure limit for skin safety [107].

Our network models were developed using PyTorch on a server equipped with 34 GB of Random-Access Memory (RAM), an NVIDIA TITAN X graphics processing unit (GPU), and an NVIDIA GeForce GTX 980 GPU. Optimization of all networks was carried out using the Adam algorithm, with β_1 and β_2 empirically set to 0.9 and 0.99, respectively. The total number of training iterations was established at 10,000. We employed the Adam optimizer [104] for

training and the loss control based on vgg-19 network [108]. We employed a step decay strategy for the learning rate, initially setting it at 0.0001. To optimize learning efficiency, a global learning rate decay strategy was implemented. This strategy involved reducing the learning rate by 90% whenever there was no decline in loss for three epochs, with the condition that the rate remained above 1×10^{-6}. Training was terminated if the loss failed to change by more than 1×10^{-5} over five epochs. The batch size for training was set to 1.

4.2.5 Axial Resolution Estimation based on Speckle Size Measurement

In the present study, axial resolutions of fake HR and SR images are estimated from measurements of axial speckle size [109]. Given that the axial resolutions of LR and HR images are provided, the axial resolutions for fake HR and SR images are derived through linear interpolation, employing speckle size measurements from LR and HR images as reference points. Herein, axial resolution is quantified by the FWHM of the speckles.

To evaluate the generated images, we estimate the speckle size by a classical method introduced in 2004 [110] which is based on the calculation for the normalized autocovariance function $c_I(x,y)$ by Eq. (4-3):

$$c_I(x,y) = \frac{FT^{-1}\left[|FT[I(x,y)]|^2\right] - \langle I(x,y)\rangle^2}{\langle I(x,y)^2\rangle - \langle I(x,y)\rangle^2}, \qquad (4\text{-}3)$$

where $I(x,y)$ is the pixel intensity at image position (x,y), FT is the Fourier Transform in short and FT^{-1} is the inverse Fourier Transform, and $\langle\,\rangle$ is the calculation for spatial mean. $c_I(x)$ and $c_I(y)$ are all the horizontal and the vertical profile of $c_I(x,y)$, respectively. $c_I(y)$ is used, and FWHM for each intensity peaks in it are averaged to characterize the axial speckle size in terms of pixel number. Instead of $c_I(y)$, the width of speckle size is characterized by the width of $c_I(0,y)$ only in [110].

4.3 Result

4.3.1 Trained Spectrums

Here, the training input spectra LR and HR, and the model applied spectra fake HR and SR, along with GT are all included in one Figure 4-4, Based on the bandwidth comparison, the trained model successfully extends the bandwidths of LR and HR, and further improves the axial resolutions. The spectrum magnitude is ranging from 0 to 255.

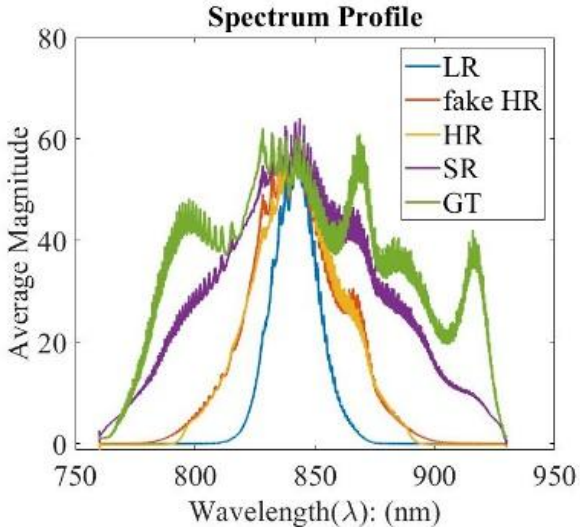

Figure 4-4.Interferometric spectra. The image obtained are shown in Figure 4-5. (a), (d), (b), (f) and (c) respectively.

4.3.2 Metrics Evaluation

The ESRGAN framework [48], a proven and mature method for deep learning-based image super-resolution, is utilized to generate a comparative set of images. This approach facilitates a direct comparison between the spectrum-based training and traditional image-based training. The PSNR and SSIM evaluation is conducted to the entire image sets (400 images) which are transformed from the trained and the generated spectral data, and the results are averaged as shown in Table 4-1. The results clearly indicate that the method for training on spectral data surpasses the conventional super-resolution techniques in terms of these specified metrics, highlighting its superior performance in enhancing image resolution.

Table 4-1. (A) Metrics evaluation results for the spectrum - trained data (average ± standard deviation),

	LR	fake HR	HR	SR
Mean PSNR (dB)	17.20 ± 0.07	19.64 ± 0.10	19.87 ± 0.08	23.24 ± 0.14
Mean SSIM (a.u.)	0.269 ± 0.003	0.376 ± 0.004	0.490 ± 0.003	0.647 ± 0.008

(B) metrics evaluation results for ERSGAN trained data (average ± standard deviation).

	LR	fake HR	HR	SR
Mean PSNR (dB)	17.20 ± 0.07	18.74 ± 0.14	19.87 ± 0.08	20.32 ± 0.30
Mean SSIM (a.u.)	0.269 ± 0.003	0.273 ± 0.003	0.490 ± 0.003	0.480 ± 0.003

4.3.3 Skin Imaging *in vivo*

Figure 4-5 to Figure 4-7 show representative examples where the proposed SR model restores

fine speckle patterns and vessel continuity compared to low-resolution inputs. The improvements are subtle but visible—especially in vessel wall definition and smoother background texture.

Figure 4-5 offers a direct comparison of the B-scan images obtained through both methodologies, with a specific focus on the area encompassing the boundary between the stratum corneum and stratum lucidum, highlighted within a yellow square box and further detailed in Figure 4-6. In the spectrum-trained images, a noticeable reduction in speckle size is evident when comparing the LR and fake HR images (as depicted in Figure 4-5 (a) and (d)), as well as when comparing the SR and authentic HR images (illustrated in Figure 4-5 (b) and (f)). Similarly, images produced using the ESRGAN method also exhibit a similar reduction in speckle size, as seen when comparing LR and fake HR images (Figure 4-5 (a) and (e)), and SR and HR images (Figure 4-5 (b) and (g)). This distinction underscores the effectiveness of training on spectral data in enhancing image resolution and detail. The images are represented as 8-bit grayscale images with pixel intensities ranging from 0 (black) to 255 (white),

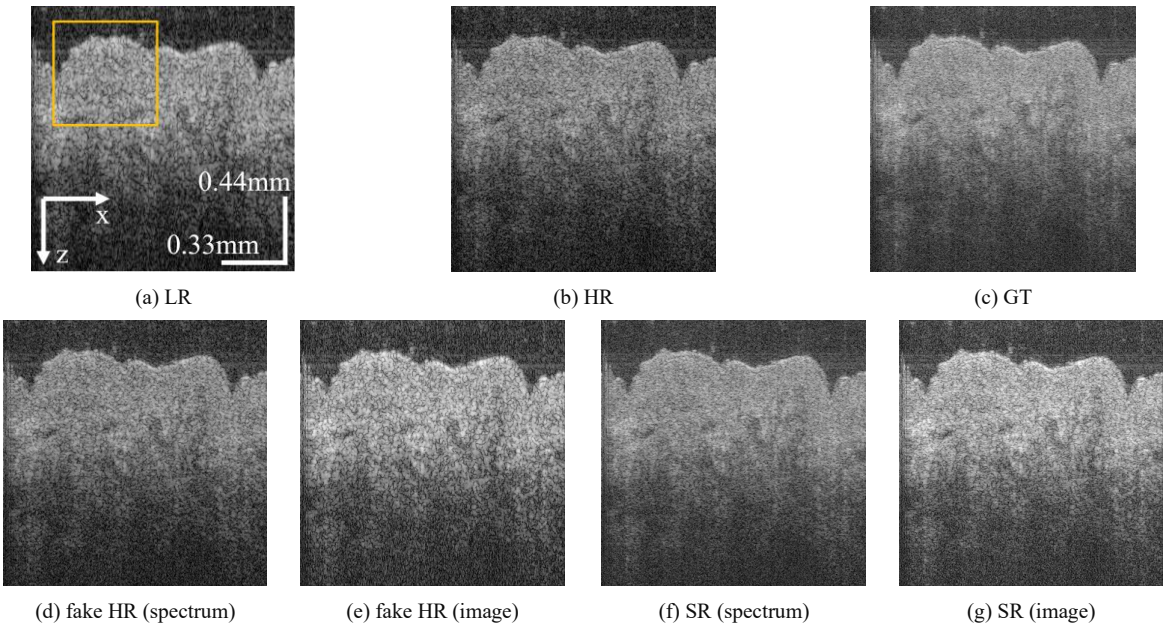

Figure 4-5. B-scan images. 'spectrum' denotes the training based on spectrum. 'image' denotes the training based on image by ESRGAN.

In Figure 4-6, the boundary of stratum corneum and stratum lucidum is selected by the yellow ellipse. The right side of the boundary is visible in all images. However, the left side of the boundary (selected in red ellipse) is only visible in SR images and GT image. To further compare the SR images of spectrum-based and image-based training, we include a part of the boundary by the orange square frames, in Figure 4-6 (c), (f) and (g), which are presented in a

zoom-in view in Figure 4-7. In Figure 4-6, the regions indicated by the orange and green arrows are continuous in (a) and (b), but is disconnected in (c). This demonstrates that the spectrum-trained results successfully recover the boundary continuity, whereas the image-based trained data fails to recover this feature.

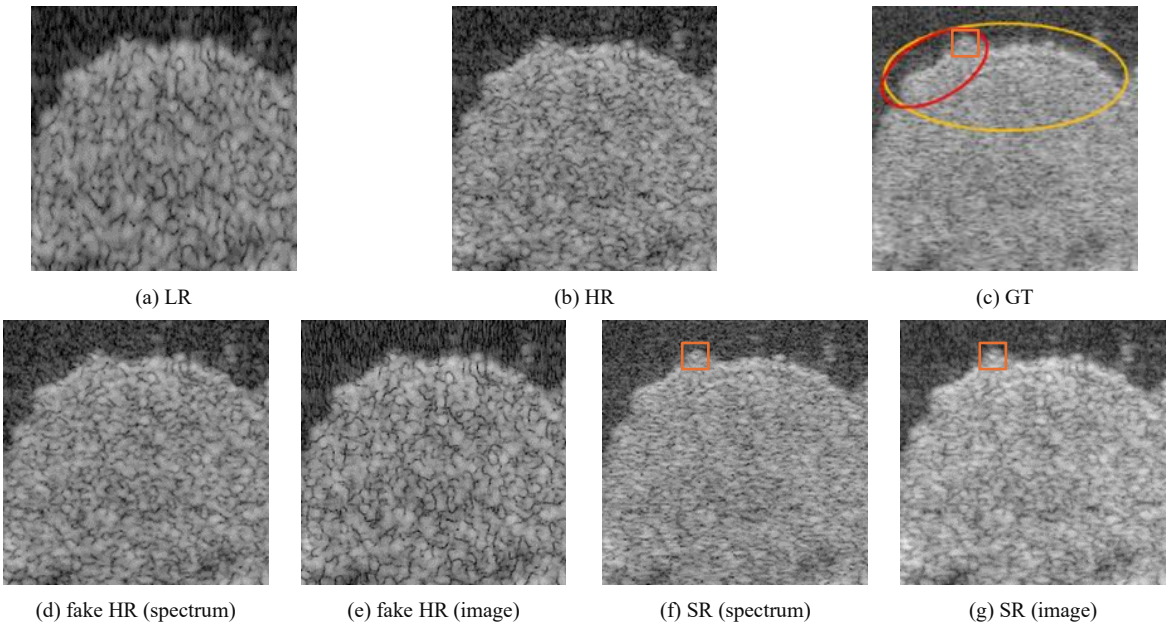

Figure 4-6. Zoom-in images of Figure 4-5. Region of interest (ROI) is indicated in Figure 4-5 (a) by yellow box.

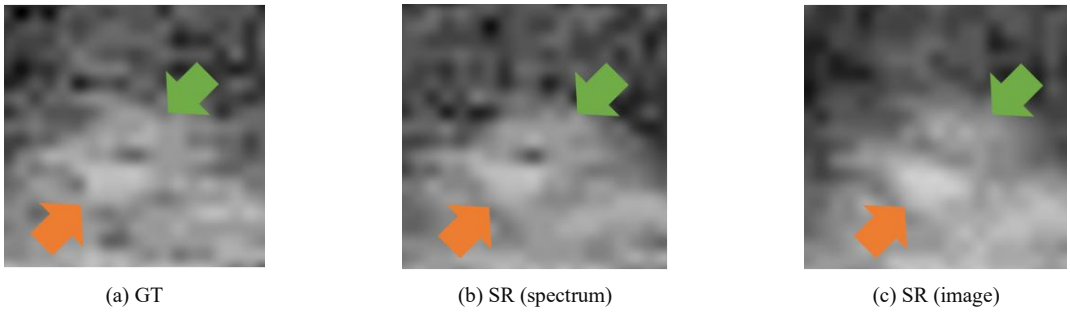

Figure 4-7. Zoom-in view of the orange square frame included region in Figure 4-6 (c) GT, (f) SR (spectrum) and (g) SR (image)

Images acquired from spectrum-based training in Figure 4-5 are measured with PSNR and SSIM, while axial resolutions for fake HR and SR are estimated in Table 4-2. The result of fake HR and SR verify the effect of axial resolution enhancement for the spectrum-based training in terms of both axial resolution estimation and metric evaluation.

Table 4-2. Axial resolution estimation for the image generated by training on spectral data based on speckle size measurements.

	Speckle size mean (pixels)	Axial resolution (μm) in air	Axial resolution (μm) in skin	PSNR (dB)	SSIM (a.u.)
LR	**6.57**	**10.87**	**15.00**	**17.26**	**0.288**
fake HR	**4.01**	**5.60 (estimated)**	**7.38 (estimated)**	**19.80**	**0.425**
HR	**3.82**	**5.21**	**7.19**	**20.12**	**0.518**
SR	**2.52**	**3.10 (estimated)**	**4.28 (estimated)**	**24.03**	**0.716**
GT	**2.17**	**2.55**	**3.52**	**-**	**-**

The axial resolution estimation is also conducted by comparing the measurement of the line widths of a bright line (the surface of the applied ultrasound gel on skin surface for strong reflection prevention) in the B-scan images, and the intensity profiles for the bright line are plotted in Figure 4-8. The outcomes of the FWHM measurements for the bright line widths and the axial resolution estimations are presented in Table 4-3. These results also validate the spectrum-based training to enhance the axial resolution, but the estimated axial resolution is slightly different form speckle size measurement method in Table 4-2.

In addition to metric improvements, visual inspection reveals clearer reconstruction of disrupted or blurred tissue layers. Notably, the dermal–epidermal junction appears more continuous, and finer textures in deeper layers are better preserved, demonstrating improved anatomical interpretability.

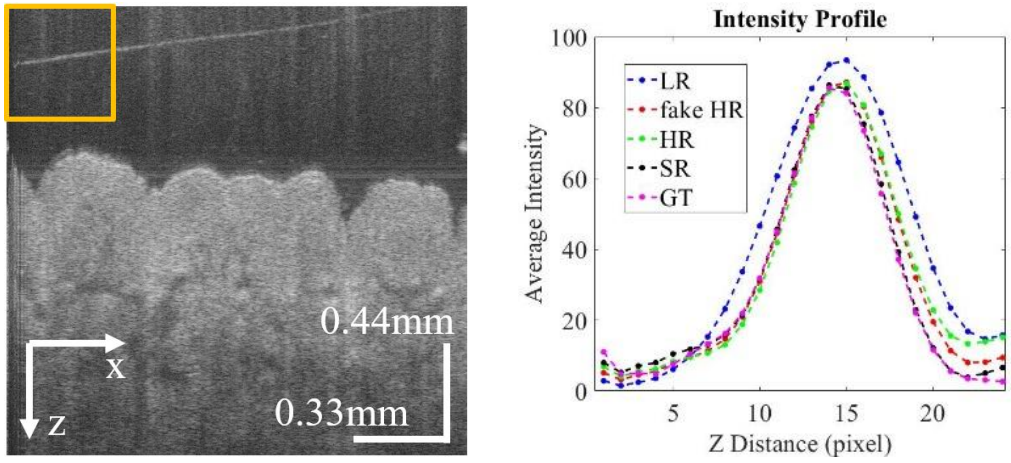

(a) (b)

Figure 4-8. (a) Interface between ultrasound gel and air (yellow box); (b) Corresponding axial intensity profiles.

Table 4-3. Axial resolution estimation for the image generated by training on spectral data based on the bright line width measurement (FWHM).

	Line width mean (pixels)	Axial resolution (μm) in air	PSNR (dB)	SSIM (a.u.)
LR	**8.67**	**10.87**	**17.26**	**0.288**
fake HR	**6.92**	**5.66 (estimated)**	**19.80**	**0.425**
HR	**6.77**	**5.21**	**20.12**	**0.518**
SR	**6.59**	**3.33 (estimated)**	**24.03**	**0.716**
GT	**6.52**	**2.55**	**-**	**-**

4.3.4 Iteratively Model Application

It has been reported that the iteratively application of the model to generate higher order SR images by image-based training led to poorer results in terms of PSNR and SSIM in [54]. Hereby, we also tried iteratively applying the model to generate higher order SR spectrums, where SR_1 is the super-resolution result acquired by applying the model onto HR, and the higher order of SR, SR_{i+1}, is acquired by applying the super-resolution model onto SR_i with $i = 1,2,3$. Comparing to HR (PSNR: 19.87 ± 0.08 and SSIM: 0.490 ± 0.003) and LR (PSNR: 17.20 ± 0.07 and SSIM: 0.269 ± 0.003), the higher order SR provides poorer effect based on metrics evaluation in Table 4-4.

Table 4-4. Metrics evaluation results for the spectral data (average ± standard deviation) of SR with its 4 iterations.

	Mean PSNR (dB)	Mean SSIM (a.u.)
$\boldsymbol{SR_1}$	$\boldsymbol{23.24 \pm 0.14}$	$\boldsymbol{0.647 \pm 0.008}$
$\boldsymbol{SR_2}$	$\boldsymbol{19.19 \pm 0.15}$	$\boldsymbol{0.450 \pm 0.006}$
$\boldsymbol{SR_3}$	$\boldsymbol{16.75 \pm 0.15}$	$\boldsymbol{0.355 \pm 0.005}$
$\boldsymbol{SR_4}$	$\boldsymbol{15.59 \pm 0.24}$	$\boldsymbol{0.322 \pm 0.006}$

However, by looking into the generated images for all higher orders of SR in Figure 4-9. Images of SR with various iterative orders (by spectrum-based trained model)., the speckles in higher order of SR are reduced in size and the boundaries between of stratum corneum and stratum lucidum become more pronounced comparing to SR_1. There is no observable boundary continuity details recovery found for SR_2, SR_3 and SR_4 comparing to GT based on SR_1.The axial resolutions are further estimated based on speckle sizes for subsequent higher order SR images in Table 4-5, where the SR_1 and SR_2 are found to have superior metric evaluation results than HR. Notably, the drop on PSNR and SSIM for SR_3 and SR_4 might be due to their speckle sizes smaller than GT. Limited to the fact that GT is the reference for all cases, we could not conclude that the SR_3 and SR_4 are even more genuine than GT, but they are valuable

to be estimations for the images with higher axial resolutions than GT. Hence, we comment that SR_3 and SR_4fail to achieve super-resolution effects. However, as for SR_1 and SR_2, the two cases show both superior estimated axial resolution and PSNR and SSIM measurements, thus successfully achieve the super-resolution effect.

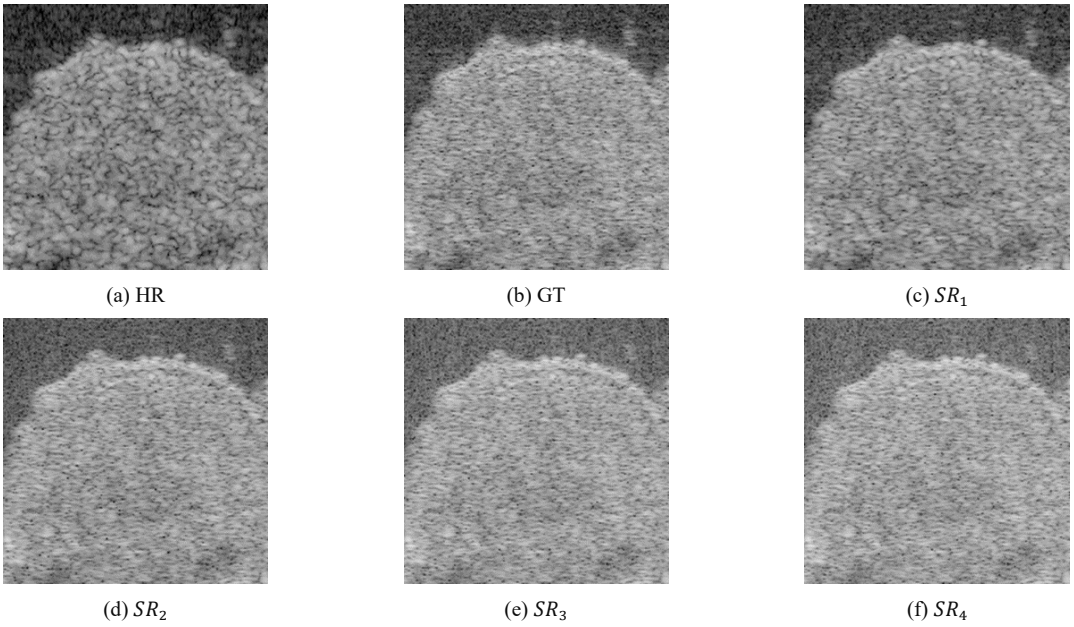

(a) HR (b) GT (c) SR_1

(d) SR_2 (e) SR_3 (f) SR_4

Figure 4-9. Images of SR with various iterative orders (by spectrum-based trained model).

Table 4-5. Axial resolution estimation for the higher order SR images based on speckle size measurements.

	Speckle size mean (pixels)	Axial resolution (μm) in air	Axial resolution (μm) in skin	PSNR (dB)	SSIM (a.u.)	Bandwidth (nm)	Bandwidth Extension (nm)
LR	**6.57**	**10.87**	**15.00**	**17.26**	**0.288**	**39.9**	**-**
HR	**3.82**	**5.21**	**7.19**	**20.12**	**0.518**	**83.2**	**-**
SR_1	**2.52**	**3.10 (estimated)**	**4.28**	**24.03**	**0.716**	**139.8 (estimated)**	**+56.7 (estimated)**
SR_2	**2.18**	**2.57 (estimated)**	**3.55**	**20.50**	**0.549**	**168.7 (estimated)**	**+28.9 (estimated)**
SR_3	**2.11**	**2.45 (estimated)**	**3.38**	**18.03**	**0.450**	**176.9 (estimated)**	**+8.2 (estimated)**
SR_4	**2.14**	**2.50 (estimated)**	**3.45**	**16.90**	**0.412**	**173.4 (estimated)**	**-3.5 (estimated)**
GT	**2.17**	**2.55**	**3.52**	**-**	**-**	**170.0**	**-**

4.4 Discussion

4.4.1 Preference on Resolution Determination

Referring to Table 4-2 and Table 4-3, the estimated axial resolutions for fake HR and SR are different up to 1.06% and 6.91% respective to the bright line width measurement. Both estimation approaches are acceptable based on their mechanism, but the speckle size approach is more preferrable. In real imaging process, the application of ultrasound gel could be very thick for strong reflection prevention, which makes the gel surface outside the depth of view of the image, but the speckles are always available to measure. Moreover, the axial speckle size serves as a more direct reference for characterizing the axial PSF, which in turn relates to axial resolution.

4.4.2 Evaluation Challenges When Super-Resolution Surpasses Ground Truth

In the iterative model application, it was observed that higher iterations of super-resolution led to a reduction in conventional image quality metrics such as PSNR and SSIM, despite visible improvements, including finer speckle patterns and sharper structural boundaries. This apparent paradox arises because the reconstructed images begin to reveal spatial details that exceed the resolution limit of the GT data, which was acquired using a lower-resolution OCT system. As a result, traditional pixel-wise metrics may incorrectly penalize these enhancements, interpreting them as deviations rather than improvements.

This observation highlights the limitations of relying solely on PSNR and SSIM to evaluate super-resolution performance in such contexts. To better capture perceptual and structural improvements, alternative evaluation strategies—such as vessel continuity analysis, structural consistency metrics, or no-reference image quality assessments—should be considered. Additionally, future work could incorporate validation using higher-resolution OCT systems or orthogonal imaging modalities to more accurately assess the fidelity of recovered fine structures when the GT is resolution-limited.

4.4.3 Network and Loss Function Simplicity

The advantage of the spectrum-based training is simpler network structure and loss function. In contrast to the ESRGAN whose generator includes 64 RRDB (23 dense blocks for each RRDB and 5 LReLU blocks for each dense block) [54], this spectrum-based training network

is much simpler (4 LReLU blocks only). Similarly, the discriminator in ESRGAN features 8 convolutional blocks and 2 linear layers, whereas our model simplifies this to just 4 convolutional blocks and a single linear layer. Moreover, while ESRGAN utilizes a composite loss function that includes adversarial loss [104] and VGG-19 perceptual loss [108] , our approach only considers Binary Cross Entropy (BCE) loss and a combined metric of PSNR and SSIM. The computation for BCE loss is straightforward and is defined as follows:

$$BCE\ loss = -\frac{1}{N}\sum_{i=1}^{N}[y_i \cdot log(\hat{y}_i) + (1 - y_i) \cdot log(1 - \hat{y}_i)], \qquad (4\text{-}4)$$

where y_i is the actual label, $\hat{y}_i$ is the predicted probability for the i^{th} example and N is the total example size [106]. BCE Loss is simpler and computationally less demanding than VGG-19 and adversarial loss, while VGG-19 based loss requires to operate a deep convolutional network, and adversarial loss is the most complex in terms of computational demands and training dynamics often requiring careful tuning and posing challenges in terms of training stability.

Alternatively, a combined metric-based loss of –PSNR – SSIM was used in certain configurations to directly optimize for structural image quality and perceptual sharpness. This approach emphasizes visual fidelity, especially important for speckle suppression and tissue boundary recovery in OCT imaging, while avoiding the complexity of VGG or adversarial losses.

4.4.4 Comparison with Hardware-Based Axial Resolution Enhancement

Hardware-based axial resolution enhancement in OCT typically relies on increasing the spectral bandwidth of the light source or employing novel interferometric configurations. Techniques such as the use of supercontinuum sources [111], broader-band swept-source lasers [112], or light source combination strategies [113] have demonstrated axial resolutions below 2 μm. While effective, these approaches often involve increased system complexity, elevated cost, and higher sensitivity to alignment and noise.

Additionally, methods like white-light interferometry or coherence revival schemes have been explored for enhancing axial performance, but they tend to reduce system robustness and scalability for clinical deployment.

In contrast, the proposed deep learning–based method enhances axial resolution computationally, without requiring any hardware modifications. This not only ensures

backward compatibility with existing SD-OCT systems but also aligns with the growing trend toward software-defined imaging platforms. By leveraging raw spectral data, the proposed model learns to recover fine structures otherwise lost due to bandwidth limitations—offering a low-cost, scalable alternative to hardware-intensive solutions.

4.4.5 Broader Applications

Our method, developed to enhance axial resolution in skin OCT imaging by utilizing full spectral data, shows significant promise for broader applications beyond dermatological diagnostics. Our self-supervised approach can potentially be applied to OCT imaging of other tissue types, particularly retinal imaging and OCTA, where high axial resolution and boundary clarity are crucial [1] [2]. While hardware-based resolution enhancement is a possible avenue for improving image quality, this study focuses on deep learning–based methods, which are more flexible, cost-effective, and compatible with future hardware upgrades.

In retinal OCT imaging, clear visualization of delicate retinal layers is essential for diagnosing and monitoring progressive diseases such as age-related macular degeneration (AMD) [114], diabetic retinopathy [115], and glaucoma [116]. In AMD, for example, precise imaging of the retinal pigment epithelium and photoreceptor layers is crucial for identifying early signs of disease progression, such as drusen accumulation [117]. Similarly, in diabetic retinopathy, enhanced resolution allows for better identification of microaneurysms, retinal edema, and neovascularization—features that are often challenging to resolve with standard resolution [85]. Our method's ability to recover sub-pixel details could thus support earlier and more accurate detection of such pathologies, potentially improving treatment outcomes.

Furthermore, OCTA, which provides microvascular imaging of retinal and other tissues, could benefit greatly from this enhanced axial resolution. OCTA is increasingly used to detect vascular changes in conditions like diabetic retinopathy and glaucoma by visualizing capillary networks and flow dynamics [117] [118]. However, conventional OCTA resolution is often limited when detecting fine vascular structures or capillary dropout in ischemic areas [120]. Our super-resolution method, by improving image clarity and continuity, could aid in identifying subtle microvascular abnormalities, such as early capillary dropout or neovascularization, which are often early indicators of retinal diseases [120].

Additionally, our approach may be adaptable to neuro-ophthalmological applications where detailed OCT imaging is vital for monitoring optic nerve integrity in glaucoma and multiple

sclerosis [121]. Enhanced imaging of the retinal nerve fibre layer and ganglion cell layer could help in detecting early, progressive nerve damage, enabling more precise assessment of neurodegenerative diseases [122].

Although the proposed SR model was trained and evaluated using data from our laboratory SD-OCT system, its architecture is designed to generalize across different OCT platforms. The method operates directly on spectral interferograms and does not rely on system-specific calibration or paired high-resolution ground truth data. Therefore, it can be applied to spectral data acquired from clinical systems—such as those using narrow-linewidth SLDs—provided the raw spectrum is accessible and properly digitized. This compatibility makes the approach hardware-agnostic and adaptable to a variety of OCT configurations without retraining, offering a promising avenue for enhancing image quality in clinical settings.

4.5 Conclusion

Our study presents a self-supervised deep learning approach for training directly on OCT spectrum data, achieving enhanced super-resolution. Our results show improved PSNR and SSIM metrics, reduced speckle size, and recovered structural details, especially in boundary regions like the stratum corneum and stratum lucidum. It also preserved realistic speckle patterns and textures, highlighting spectrum-based training's potential to refine OCT image quality for more accurate diagnostics in dermatology, with applications extending to ophthalmology and neuro-ophthalmology.

Chapter 5. : OCT-Patch Bio-sensing

5.1 Introduction

Skin health has garnered increasing attention in recent years, as various internal and external factors, such as hormonal imbalances and cosmetic products, can alter the skin's composition and function [10]. These influences often lead to skin issues, such as inflammation, which manifest as changes in tissue structure and require medical attention for accurate diagnosis and treatment [9]. Non-invasive imaging techniques, particularly optical methods such as OCT, play a vital role in evaluating these conditions [12]. OCT has become a widely used tool in skin diagnostics, offering depth-resolved, high-resolution structural imaging. Initially developed in the 1990s for ophthalmology to visualize retinal layers, OCT has evolved significantly, advancing in speed, resolution, and imaging depth. Its applications have expanded beyond ophthalmology to fields such as dermatology, providing detailed views of skin layers and structures [1] [13] [85]. However, while OCT excels at capturing structural information, it remains limited in detecting biochemical changes essential for diagnosing certain skin conditions [13].

As OCT is traditionally limited to structural imaging, wearable hydrogel patches have emerged as a promising solution for real-time biochemical monitoring of skin conditions, detecting critical biomarkers such as pH, glucose, and lactate through sweat analysis. [55]. These biomarkers are essential in identifying and managing skin-related illnesses, including inflammatory conditions like dermatitis, psoriasis, and eczema, where biochemical shifts are early indicators of inflammation [11]. Despite the potential, no hydrogel patch has yet been integrated with OCT to enhance its diagnostic capability by adding biochemical insights, which would significantly advance non-invasive skin assessments.

In this study, we introduce the integration of SD-OCT [5] with a hydrogel patch to combine the strengths of both technologies. The hydrogel patch incorporates LC droplets, which are highly effective biosensors, especially for detecting molecular interactions at interfaces, making them ideal for monitoring biologically relevant parameters [57] [58] [59], [64]. pH, for instance, is crucial for skin health monitoring [122] [123] as shown in Figure 5-1 (a), and here, LC droplets are functionalized with phenylboronic acid (PBA) to respond to pH changes. As shown in Figure 5-1, when LC droplets in the patch encounter varying pH levels, their polarization shifts from a bipolar to a radial configuration as pH increases. This polarization change is reflected

as the refractive index change inside LC droplets and is captured in the OCT images as axial droplet imaging size change, reflecting real-time pH variations. We calibrated and validated the patch over a physiological pH range from 6.0 to 8.0, achieving an accuracy of ±0.2 pH, with imaging transverse and axial resolutions of 14.71 μm and 4.2 μm in patch respectively, while the LC particle sizes are no more than 5 μm. Applying the patch to human skin, we observed real-time changes in pH responses, allowing non-invasive biochemical monitoring.

We believe this dual-functionality could enable OCT imaging to concurrently provide critical biochemical data, enhancing diagnostic precision and monitoring for conditions such as inflammation. Additionally, our system addresses several limitations of existing commercial skin pH meters, offering improved comfort, sterility, and adaptability. Unlike conventional devices, it features soft, disposable patches for sensitive applications and the ability to measure mean pH over time. These advancements, coupled with the system's potential for multi-parameter sensing and AI-assisted calibration, establish it as a promising tool for more precise and versatile diagnostics.

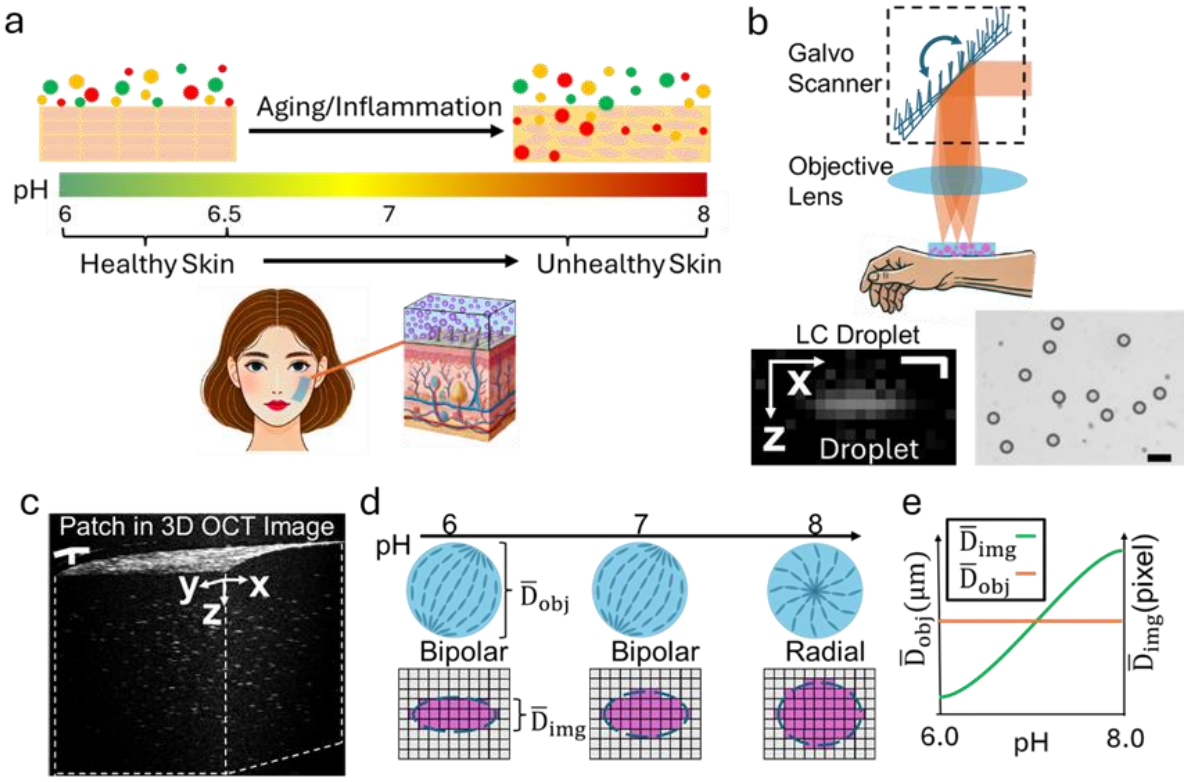

Figure 5-1. ***Concept of Liquid-Crystal Hydrogel Patch for Skin pH Sensing by OCT.*** ***(a)*** *Schematic illustrating pH as a factor in skin health and schematic for hydrogel patch pasted on face skin.* ***(b)*** *OCT image acquisition on hydrogel patch, zoom-in view on single LC droplet in cross-sectional OCT image (scale bars: 15 μm) and LC droplets in microscopy image (scale bar: 10 μm).* ***(c)*** *3-dimensonal (3-D) OCT image for hydrogel patch (scale*

*bars: 120 μm). **(d)** Sensing mechanism: LC droplet polarization and imaging size measurement for different pHs. **(e)** Average real droplet size $\overline{D}_{obj}$ and average droplet imaging size $\overline{D}_{img}$ measurement by different pH for sensing.*

5.2 Results

5.2.1 Sensing Mechanism Evaluation by Sodium Dodecyl Sulphate (SDS) Experiment

The LC molecules could form droplets when vibrating central-outwards. Bipolar and radial LC droplets are typically produced by coating their surfaces with PVA and SDS, respectively [125]. In subsequent contents, PVA-LC and SDS-LC droplets represents the PVA and SDS coated LC droplets respectively. Hence, the polarization of PVA-LC droplet will change from bipolar to radial stimulated by SDS with the polarizations illustrated in **Figure 5-2** (a). In our study, we assume all droplets are ideal 3-D spheres.

As shown in **Figure 5-2** (a). Illustrated by a light polarized along the LC director (e-ray, polarization direction is represented by blue arrow) sees extraordinary refractive index n_o, while that polarized perpendicular (o-ray, polarization direction is represented by pink arrow) to the LC director sees ordinary refractive index n_e. Then, if the light is polarized at a θ angle with respect to the LC director (represented by black arrow), it sees an effective refractive index n_{eff}, expressed as [64]:

$$n_{eff} = \frac{n_e n_o}{\sqrt{(n_e \sin\theta)^2 + (n_o \cos\theta)^2}}. \quad (5\text{-}1)$$

The overall refractive index of the droplet could be calculated by the average refractive index $\langle n_{eff} \rangle$ throughout the entire droplet as:

$$n_{overall} = \langle n_{eff} \rangle = \frac{1}{V} \int n_{eff}(r)\, dV, \quad (5\text{-}2)$$

where r is the LC position inside the droplet while the centre of the droplet is origin of the coordinate, and V is the droplet volume. It is suggested in [126] that the refractive indices n_o and n_e for our LC material are estimated as 1.5 and 1.7. Thereafter, the overall average refractive indexes for PVA-LC droplet (bipolar polarized) and SDS-LC droplet (radial polarized) are measured to be 1.628 and 1.546 by MatLab simulation.

Let C be v/v concentration of SDS, which is equivalent to the probability of SDS bonded PVA-LC droplets in the solution as occurrence of radial polarization, $P(radial)$. Assuming the spreading of the SDS into PVA-LC is even, then the overall refractive index of a droplet is:

$$n_{overall} = P(bipolar) \cdot n_{bipolar} + P(radial) \cdot n_{radial} \quad (5\text{-}3)$$

$$\equiv (1 - C) \cdot n_{bipolar} + C \cdot n_{radial},$$

where P($bipolar$) is the occurrence of bipolar polarization. In an image taken for the droplet along axial direction (z direction), the droplet imaging size (D_{img}) in pixel count has such relationship with the real droplet size (D_{obj}) as:

$$D_{img} = \frac{D_{obj}}{\delta z_{obj}} = \frac{D_{obj}}{\delta z_{air} \cdot n_{overall}}, \quad (5\text{-}4)$$

where δz_{air} is the axial resolution measured in air. Hence, we have:

$$D_{img} \propto \frac{1}{[(n_{radial} - n_{bipolar}) \cdot C + n_{bipolar}]}, \quad (5\text{-}5)$$

Since the signal intensity correlates with the reflectivity, which is also implied as the object refractive index overwhelming the environment, the measurement in **Figure 5-2** (b) tries to characterize this relationship. However, based on the results, the refractive index increase based on the increase on SDS concentration does not lead to a remarkable change on the average intensity. The difference on intensity caused by the concentration of SDS is not remarkable either. Hence, the intensity of the droplets is not an appropriate indicator to sense the environment change, which matches our theoretical analysis. The average droplet imaging size is then studied.

The average droplet imaging size is tried for sensing the environment change causing the polarization change in PVA-LC droplets while PVA-LC droplets are in aqueous solution (**Figure 5-2** (c)) and assembled in hydrogel (**Figure 5-2** (d)). In **Figure 5-2** (d), the SDS concentration is fixed, but the hydrogel containing the LC droplets is gradually immersed, allowing SDS to saturate into the hydrogel over time. This gradual saturation mimics the effect of increasing SDS concentration as more SDS interacts with the LC droplets over time. The fitting curves for **Figure 5-2** (c and d) are $y = \frac{33.94}{-0.40x + 100.01} + 2.14$ and $y = \frac{19.40}{-0.91x + 99.99} +$

2.43, which match our analytical model mentioned in Eq. (5-5). Since the concentration of SDS could never infinitely increase, there is a saturation level for both **Figure 5-2** (c and d).

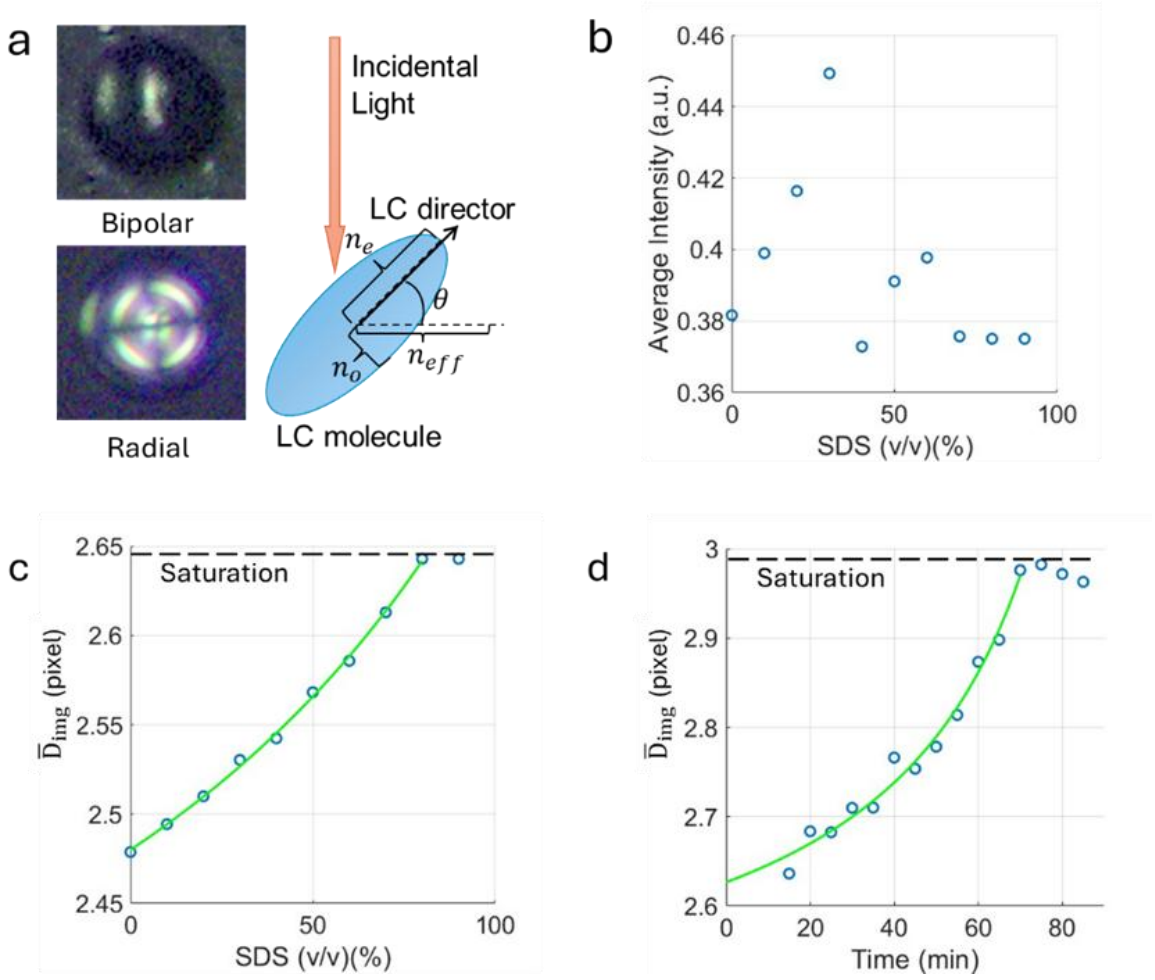

Figure 5-2. Mechanism and measurements on LC droplets. ***(a)*** *Polarization of different LC droplets and schematic of individual LC molecule under incidental light.* ***(b)*** *Normalized average intensity of LC droplets in OCT image for varying SDS v/v concentration in aqueous solution.* ***(c)*** $\bar{D}_{img}$ *measured in pixel for varying SDS v/v concentration in aqueous solution.* ***(d)*** $\bar{D}_{img}$ *measured in pixel in hydrogel when a fixed concentration of SDS is saturating into the hydrogel for a period.*

5.2.2 OCT Axial Resolution Impact on Sensing

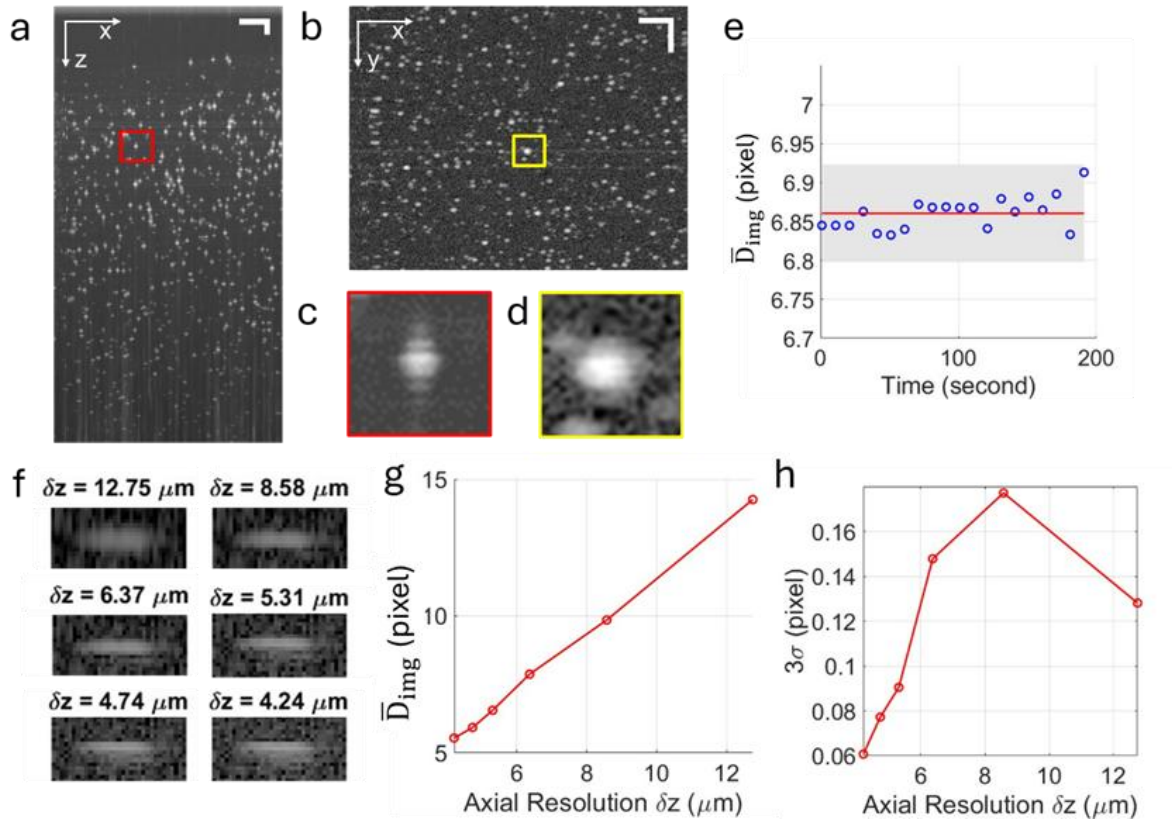

Figure 5-3. OCT images and measurement evaluations for LC droplets in an SDS 50% v/v solution and hydrogel patch *(a) Cross-sectional OCT image (scale bar: 120 μm). (b) En-face view showing LC droplets (scale bar: 120 μm). (c, d) Zoomed-in views of selected droplets highlighted in (a) and (b), respectively. (e) Repeated measurements of droplet diameter $\bar{D}_{img}$ at a fixed location to assess measurement stability. (f) Cross-sectional droplet views at different axial resolutions. (g) Average droplet diameter $\bar{D}_{img}$ plotted against axial resolution. (h) Corresponding 3σ values representing variation in size estimation.*

The OCT images of LC droplets in an SDS solution are shown in **Figure 5-3** (a-d). With a low sample power (7 μW), non-LC objects, such as background structures, are largely invisible compared to the LC droplets. In **Figure 5-3** (a), variations in droplet axial sizes are distinguishable. However, due to the axial resolution limit (4.2 μm), droplets smaller than 8.6 μm are challenging to discern, as per the Nyquist sampling theorem. **Figure 5-3** (b) similarly shows that droplets with transverse dimensions below 29.42 μm (twice the transverse resolution) are difficult to resolve. The small 3.42 μm scanning step size also causes an apparent size enlargement of smaller droplets due to oversampling.

As we focus on axial size for refractive index relevance, the cross-sectional view provides the necessary data. Comparing **Figure 5-3** (c) and (d), the single droplet appears differently in the

axial and transverse views: the transverse view shows a smooth intensity profile, while the axial view reveals multiple scattering effects from the LC molecules' strong reflectivity. For $\overline{D}_{img}$ assessment, we exclude the multiple scattering areas. Given these limitations for single-droplet evaluation, our method is more effective for assessing all LC droplets within a 3D OCT image.

During patch production, the LC droplets are limited to a diameter of no more than 5 μm. The axial resolution for LC droplets in our setup is approximately 4.2 μm (estimated by setting the refractive index to 1.6), which theoretically corresponds to a resolution of just one pixel in the image. Despite this, our results show that the droplet imaging size exceeds one pixel, and the size variation is measurable. In **Figure 5-3** (e), the mean and 3 times of standard deviation (σ) are measured as 6.86 and ± 0.06 based on the data variation measurement. This 3σ value characterize the measurement accuracy.

Moreover, since the LC droplet size is comparable to the axial resolution and can still be successfully imaged, it would be valuable to investigate whether droplets smaller than the axial resolution can also be effectively detected. Hereby, we degrade the axial resolution by narrowing the spectral width ($\Delta\lambda$) according to the relationship $\delta z = \frac{2\ln 2}{\pi}\frac{\lambda_c^2}{\Delta\lambda}$, where λ_c represents the central wavelength of the spectrum [5]. This step is achieved by applying narrower Gaussian windows on the spectrum. The resulting images are shown in **Figure 5-3** (f). As the axial resolution improves from 4.2 μm to significantly higher values (as seen in **Figure 5-3** (g)), the average droplet imaging size remains measurable, demonstrating an increase as the axial resolution decreases. This indicates that the technique remains effective even at lower resolutions. The high reflectivity of LC droplets, particularly when compared to their surrounding environment, ensures their visibility in the images, even at reduced axial resolution levels. Furthermore, based on **Figure 5-3** (h), the lower axial resolution will cause much higher 3σ value, the greatest detected 3σ in average droplet imaging size (0.18 pixels at $\delta z = 8.58\ \mu m$) will yield to a 34.5% measurement.

5.2.3 OCT with Patch Sensing for pH Change

The behaviour of LC droplets, when interacting with PBA, is highly sensitive to changes in pH due to the ionization states of the functional groups on the PVA-LC-PBA droplet. At lower (acidic) pH levels, the carboxyl groups ($-\mathrm{COOH}$) on the surface of the PVA-LC-PBA droplet remain protonated, leading to bipolar polarization within the droplet. When the pH increases

and the environment becomes more alkaline, the carboxyl groups deprotonate, transitioning into their ionized form. This deprotonation process disrupts the molecular alignment of the PVA-LC-PBA droplet, causing a noticeable change to radial polarization [126] [127]. The interaction between PBA and the LC molecules facilitates this transition, enhancing the sensitivity of the droplets to pH changes as shown in **Figure 5-4** (a).

Thereafter, Eq. (5-5) needs to be modified as the concentration of PVA-LC-PBA changes for the varying pH environment. Since the PVA-LC-PBA droplets are protonated with $-\mathrm{COOH}$, this model captures the asymmetry in droplet behaviour in response to acidic versus alkaline conditions. $\mathrm{pK_a}$, or the acid dissociation constant, is the pH at which half of the carboxyl groups are dissociated ($\mathrm{COOH} \leftrightarrow \mathrm{COO^-} + \mathrm{H^+}$). When pH equals $\mathrm{pK_a}$, there is an equal proportion of protonated ($-\mathrm{COOH}$) and deprotonated ($-\mathrm{COO^-}$) species. As the pH increases beyond the $\mathrm{pK_a}$, the $-\mathrm{COOH}$ groups dissociate, leading to an increase in the negative surface charge ($-\mathrm{COO^-}$). In acidic environments ($\mathrm{pH} < \mathrm{pK_a}$), the refractive index changes less due to the limited dissociation of $-\mathrm{COOH}$ groups and is only dominated by droplet polarization. Therefore, the use of $\mathrm{pH} - \mathrm{pK_a}$ reflects the observed experimental asymmetry, where droplet size and refractive index change more significantly in alkaline conditions [129]. Thus, substituting C in Eq. (5-5) with $C \propto \frac{1}{1+10^{pH-pK_a}}$ based on Henderson-Hasselbalch equation [130], then:

$$D_{img} \propto \frac{1}{\left[(n_{radial}-n_{bipolar})\cdot\frac{1}{1+10^{pH-pK_a}}+n_{bipolar}\right]}, \qquad (5\text{-}6)$$

For the calibration and testing of the LC-based hydrogel patch, we exposed the patch to controlled pH environments ranging from 6.0 to 8.0, with incremental steps of 0.2. This method was selected to capture the precise changes in polarization that occur in LC droplets as the pH environment shifts. Each pH level was maintained long enough for the LC droplets to respond fully, ensuring accurate data collection. OCT images were acquired at each pH increment, and the average droplet imaging size — previously identified as an indicator of polarization change — was measured to assess the LC response. The PVA-LC-PBA droplets are filtered to retain only those with a diameter of no more than 5 μm before making the hydrogel, making them more suitable for assembling into small biological structures [131].

The average droplet imaging size change due to pH changes are measured as a calibrator. Thereafter, a set of testers with preset pH values are also measured with the average droplet imaging size and calculated the measured pH based on the calibrator curve. Ultimately, the

measured pH values are compared with the preset pH to validate the method. Taking $3\sigma = \pm 0.06$ from **Figure 5-3** (e) measurement and based on [132], the measurement accuracy is carried out as $\frac{3\sigma}{E\left(\frac{dy}{dx}\right)} = \pm 0.231$, and $E\left(\frac{dy}{dx}\right)$ is the mean of $\frac{dy}{dx}$ of the fitting over the range that x varies between 6.0 and 8.0 measured as 0.260. When immersed in pH environment, the trend of average droplet imaging size change is measured in **Figure 5-4** (b) (Fitting equation: $y = 11.36\left(\frac{1.89-2.07}{1+10^{7.00-x}} + 2.07\right)^{-1}$), where the fitting is based on our analytical model in Eq. (5-6). Then in **Figure 5-4** (c), the measured pH values based on the fitting curve of the calibrator in **Figure 5-4** (b) are near to the preset pH values as within the 3σ range with root mean square error (RMSE) 0.190 within the accuracy range 0.231. The results align with the analytical relation in Eq. (5-6).

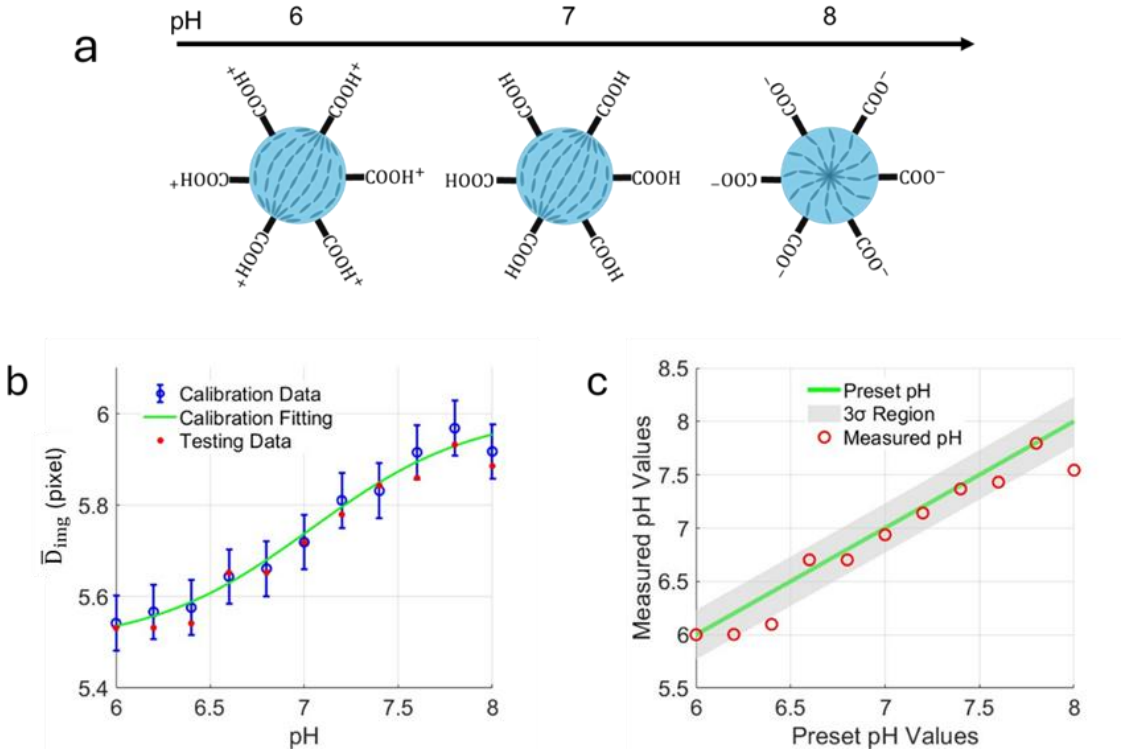

Figure 5-4. Patch pH sensing calibration and testing. ***(a)*** *Schematic for PVA-LC-PBA droplet in different pH environment.* ***(b)*** $\bar{D}_{img}$ *measured on hydrogel in different pH environment for both calibration and testing purpose.* ***(c)*** *Validation for testing data by* 3σ *region.*

5.2.4 OCT with Patch on-skin Sensing

While OCT faces resolution constraints in cellular imaging, our pH biosensor demonstrates excellent performance within a critical physiological range. Areas like the axillae, groin, toe interdigit, and anus, with pH values between 6.1 and 7.4, are prone to microbiome imbalances

that can trigger infections and eczematous reactions [133]. Our experiment, covering a pH range from 6.0 to 8.0, aligns closely with these values, validating the biosensor's effectiveness in relevant conditions. This validation supports the biosensor's intended diagnostic role for inflamed skin, where abnormal pH fluctuations — typically from 6 to 8, while healthy skin remains below this range [123]. The biosensor's sensitivity and accuracy suggest significant potential for monitoring pH-related skin conditions, expanding its relevance in targeted biomedical applications.

To evaluate the method's feasibility for real-world applications, PVA-LC-PBA droplets were incorporated into a hydrogel patch and imaged across 8 regions using OCT, as illustrated in **Figure 5-5** (a). In the forearm, the 8 scanned regions consistently showed a stable pH measurement around 6.3, which aligns with the typical pH of sweaty skin [134], as depicted in **Figure 5-5** (b). Mean measured for $\overline{D}_{img}$ and pH are 5.570 and 6.3 respectively. **Figure 5-5** (c) presents the average pH measurements for the forearm, axillae, groin and toe interdigit, all of which fall within the normal healthy pH range as referenced in [133]. Additionally, the patch was immersed in pure water as a control group for comparison.

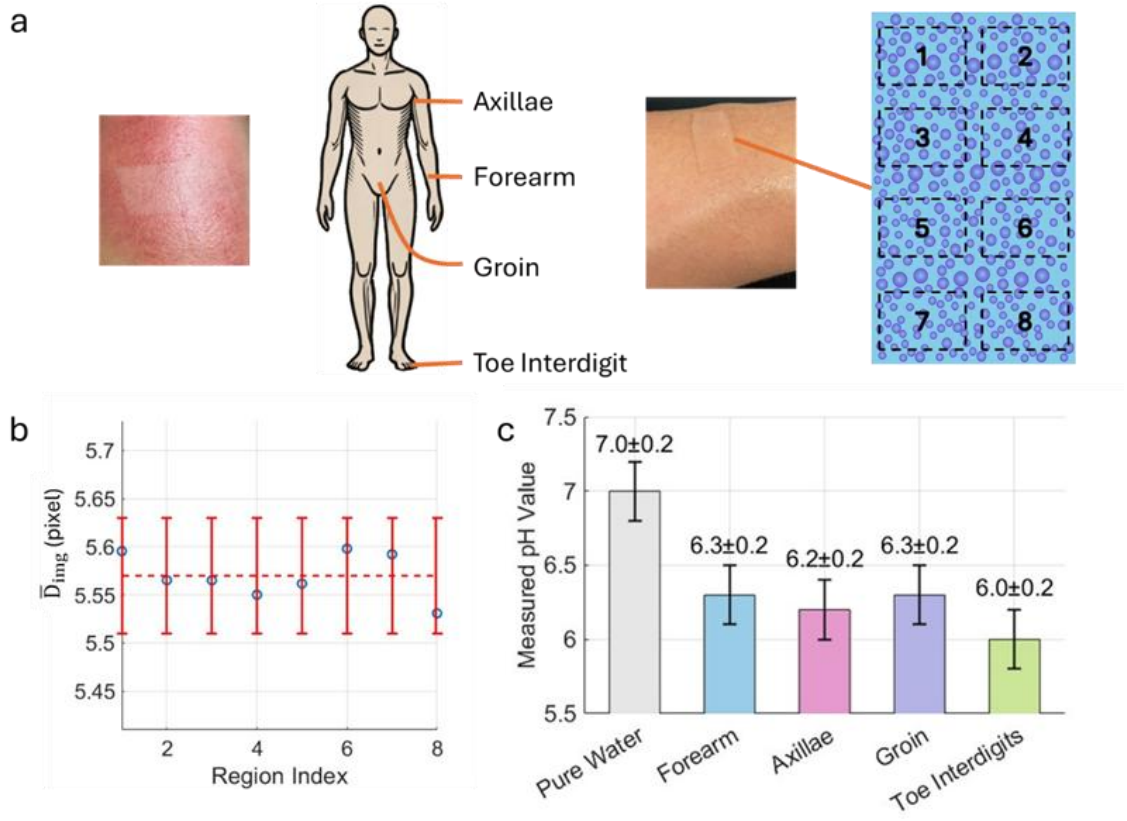

Figure 5-5. Patch-based Skin Sensing. (a) *Illustration of patch pasted on inflamed area and four body areas*

selected for pH measurement using a hydrogel patch, including application to a sweaty forearm and an inflamed region, with 8 designated regions on the patch for OCT imaging. ***(b)*** *Mean* $\overline{D}_{img}$ *values measured across all 8 regions on the patch for the sweaty forearm.* ***(c)*** *Average pH measurements recorded for each of the 4 body areas.*

5.3 Discussion and conclusion

This study combines OCT with an LC-based hydrogel patch to create a dual-function system that captures both structural and biochemical data. By leveraging LC droplets' sensitivity to environmental changes, we demonstrated that average droplet imaging size indicates LC polarization shifts due to SDS [135], enabling us to calibrate a pH-sensitive hydrogel patch for real-time pH detection. Remarkably, even droplets below OCT's axial resolution were measurable, showcasing this method's precision. This integration not only validates OCT for LC biosensing but also shows promise for wearable, real-time biochemical monitoring.

Compared to confocal microscopy, which typically captures only a small number of LC droplets within a single field of view, OCT enables imaging of a substantially larger area containing many more droplets. This allows for averaging across a broader sampling population, thereby reducing measurement uncertainty. Furthermore, while confocal microscopy requires the LC patch to be removed and carefully positioned under the objective lens, our OCT-based method supports a wearable configuration.

While this thesis focuses on pH sensing, the OCT–LC platform holds promise for detecting other analytes via refractive index changes in LC droplets. Prior studies have demonstrated glucose sensing using 5CB droplets [59], and cholesterol-modified LC droplets show responsiveness to pH, temperature, and glucose [136]. Proteins and metal ions can alter LC orientation at droplet interfaces [65] [136], providing another potential sensing mechanism. Additionally, LC droplets are known to respond to electric fields through electrostatic alignment changes; however, such applications typically require high field sensitivity and are currently limited to controlled environments [56] [138]. These sensing modalities were not experimentally validated in this study and are discussed as future directions. Furthermore, the effects of real-world variability—such as skin hydration, temperature shifts, and motion—on sensing performance were not systematically explored here, but are critical considerations for future development aimed at clinical translation.

The sensing mechanism in this study relies on refractive index and polarization changes within LC droplets, which are primarily modulated by pH in the current context. However, other

environmental factors—such as temperature, hydration level, or ionic strength—may also influence the refractive index of the surrounding hydrogel matrix or the LC alignment itself. These factors could introduce cross-sensitivities, potentially complicating the interpretation of results when used in variable physiological conditions. Although the present work focuses solely on pH detection, future efforts toward multi-parameter sensing could incorporate design strategies to decouple overlapping influences. These may include ratiometric imaging approaches, spectral decomposition, the use of orthogonal sensing elements, or dynamic calibration methods. Acknowledging and addressing these cross-sensitivities will be important for advancing the reliability and specificity of LC-based biosensors in complex biological environments.

The SDS validation experiment confirms that changes in surfactant concentration can alter the apparent imaging size of LC droplets, supporting the hypothesis that polarization changes affect the optical response captured by OCT. This mechanism also underlies the pH sensing behaviour of the PVA–LC–PBA droplets used in this study. Specifically, the presence of PBA introduces pH-sensitive binding interactions with hydroxyl or diol groups, which modify the surface anchoring conditions of the LC droplets. At higher pH values, deprotonation of PBA promotes stronger binding with vicinal diols in the PVA network, leading to alterations in the LC molecular orientation and consequently the birefringence and scattering profile. These polarization changes manifest as measurable differences in apparent droplet size in the OCT cross-sectional images. While this study primarily provides a theoretical and mechanistic explanation of this pH-polarization coupling, further experimental validation—such as polarized light microscopy or birefringence quantification—could provide deeper insight into the molecular-level reorientation dynamics and support the observed imaging results more directly. This is identified as an important direction for future work.

The current method is designed to detect average changes in apparent droplet imaging size over a defined volume, which effectively captures the ensemble response of a population of LC droplets within the hydrogel patch. Given the axial resolution of approximately 4.2 μm and the sub-resolution nature of individual LC droplets (typically <5 μm in diameter), resolving and interpreting the behaviour of single droplets remains challenging. Instead, the observed changes reflect a spatially averaged response, which is particularly suitable for monitoring global or regional pH shifts across the sensing area. However, this ensemble-based measurement inherently limits the ability to resolve highly localized pH variations or detect

heterogeneous responses among individual droplets. Variations in droplet size, orientation, or interaction with the surrounding matrix may also contribute to signal variability. While this averaging approach improves robustness and reduces the impact of noise, it also smooths out finer-scale responses. Future enhancements could involve improving spatial resolution through higher-resolution OCT systems or incorporating complementary imaging techniques that enable single-droplet analysis, allowing a more detailed investigation of local droplet behaviour and pH microenvironments.

Our method offers significant advantages over existing commercial skin pH meters, such as those produced by HORIBA, Cortex, and Courage + Khazaka [138] [139] [140] [141] [142]. While these commercial devices provide baseline functionality, their rigid designs, limited adaptability, and potential for cross-contamination present notable limitations that our approach effectively addresses. Unlike conventional meters with rigid probes that can cause discomfort or irritation on fragile or inflamed skin, our patches are soft and conformable, ensuring safe and comfortable use even in sensitive applications. Furthermore, the disposable design of the patches ensures sterility, eliminating the risk of cross-contamination inherent in reusable meters that require meticulous cleaning. This feature is particularly advantageous for clinical applications demanding high hygiene standards. Beyond comfort and sterility, our method employs statistical reliability by analysing plenty LC droplets within a confined area, enabling robust and reproducible measurements, even in localized or challenging testing scenarios like small wounds or inflamed regions. In contrast, commercial devices typically rely on single-point measurements, leading to potential inconsistencies. Additionally, our patch is capable of measuring the mean pH over a long period, providing valuable temporal insights into skin pH changes, whereas commercial devices are limited to capturing pH at a single moment in time. The adaptability of our system further extends its superiority, as it can be chemically tailored to detect additional parameters, such as glucose or temperature, beyond standard pH sensing, thereby expanding its utility in diagnostics and monitoring. The potential for integration with artificial intelligence enhances the system's ease of use by simplifying calibration, reducing the need for reference points, and ensuring consistent results, directly addressing operational inefficiencies associated with commercial meters. Collectively, these innovations position our methodology as a superior, versatile, and user-friendly alternative for both clinical and research applications.

5.4 Method

5.4.1 OCT System Setup

The homemade SD-OCT system use a light source (SUPERLUM M-T-850-HP) which provides illumination over a 170 nm spectral width centred at 850 nm. The light is guided by a 90:10 fibre coupler to the sample and reference arms. The collimated beam is dispersed by a 1500 lines/mm grating (PING-1500, Ibsen photonics) and focused by a multi-element camera lens onto a line camera (EV71YEM4CL2010-BA8, E2V). The total photon-to-electron conversion efficiency of the spectrometer was measured to be 0.75, which includes the diffraction efficiency of the grating and quantum efficiency (~47%) of the camera sensor. The total ranging depth is 1.74 mm and the roll-off is 4.06 dB/mm from DC to the -6 dB point. Spectra are digitized at 12-bit resolution and transferred to the computer through camera link cables and an image acquisition board (KBN-PCE-CL4-F, Bitflow).

The axial resolutions are measured as 2.55 μm in air. The transverse resolution is 14.71 μm. We employed an A-line rate of 20 kHz for imaging. There are 512 A-lines per B-frame and 400 B-frames per scan volume, so that the total acquisition time is 10.24 seconds (400 data is for each data set). With 3.42 μm transverse step size, FOV is 1.75 mm × 1.37 mm. Based on the signal detected by the spectrometer, the sensitivities are measured to be 107 dB. The 6 dB sensitivity roll-off in solution is measured as 0.55 mm (refractive index 1.33 for water as the low droplet solution is equivalent the overall refractive index approximately to water [144]). The total optical power incident on the sample is set to 7.5 μW, an atypically low power level chosen to prevent signal saturation due to the highly reflective nature of the LC droplets.

5.4.2 Fabrication of LC Droplets

The PVA-LC droplets were directly stimulated by SDS and imaged using OCT. Ten sets of LC droplets were prepared by dissolving 30 μL of 51 wt% 4′-pentyl-4-biphenylcarbonitrile (Sigma, 328 510) into varying volumes (0.1, 0.2, 0.3, 0.4, 0.5, 0.6, 0.7, 0.8, 0.9, 1.0 mL) of a 1 wt% PVA solution. The resulting mixtures underwent 1 minutes of sonication to facilitate the formation of LC droplets. Each of these 10 sets was then combined with corresponding volumes (0.9, 0.8, 0.7, 0.6, 0.5, 0.4, 0.3, 0.2, 0.1, 0 mL) of a 1 wt% SDS solution, and subsequently imaged.

Additionally, PVA-LC droplets were embedded within a hydrogel matrix for further imaging. In this process, 30 μL of 51 wt% 4′-pentyl-4-biphenylcarbonitrile was dissolved in 1 mL of a 1

wt% PVA solution and sonicated for 1 minutes to generate LC droplets. The mixture was then incorporated into a liquid hydrogel, which was allowed to solidify. The hydrogel, containing the PVA-LC droplets, was immersed in a 1 wt% SDS solution and imaged at 15 points, with a 5-minute interval between each sampling, starting 15 minutes after the immersion. Hence, the SDS solution could gradually saturate into the hydrogel and bind with PVA-LC droplets.

5.4.3 LC Droplets Fabrication for pH Experiment and Patch Production

The hydrogel, containing PVA-LC-PBA droplets, was prepared for testing in various pH environments to simulate biomedical applications. The PVA-LC-PBA droplets were fabricated by doping LC molecules with 0.25 wt% of 4′-n-hexylbiphenyl-4-carboxylic acid (Alfa Aesar, B21900.03) during the process. This doping was intended to enhance the droplets' responsiveness to environmental stimuli. The chiral doped PVA-LC droplets were produced by doping (S)-4-cyano-4′-(2-methylbutyl) biphenyl (Tokyo Chemical Industry, C2913) to the PVA-LC droplets.

To simulate the conditions these droplets would encounter within biological tissue, a series of 11 pH points, ranging from 6.0 to 8.0 with 0.2-step increments, were prepared. The buffer solutions were diluted using HORIBA 4.01 buffer for pH levels between 6.0 and 6.8, and HORIBA 10.01 buffer for levels between 7.2 and 8.0. Pure water was used for the pH 7.0 condition. The prepared hydrogel with PVA-LC-PBA droplets was placed in these environments to examine the droplet response and to observe how the assembly performs under conditions mimicking real biological systems.

5.4.4 Data Processing

Since SD-OCT is used, the signal acquired is spectrums. The spectrum data is inspected to observe any influence made by the environment stimulation. Thereafter, the spectrum data experience Fourier transform into OCT image data.

When a 3-D OCT image is obtained, there are thousands of PVA-LC droplets included. In each individual B-scan images (scan in x-z plane), LC droplets are included at the centres of fixed-size frames by searching the local maximum signal intensity. The positions of the same droplet in successive B-scans are noted so that the single droplet will be included within a single 3-D sub-cropped image by the frames applied. Since the axial resolution is more optimal than the lateral resolution, the droplets included in the frames are measured along the central axial direction by counting the number of pixels that represent the axial diameter of the droplet as

droplet imaging size $\overline{D}_{img}$.

Chapter 6. : Conclusion and Future Work

6.1 Conclusion

In this thesis, we have made significant strides in advancing the fields of OCT imaging and biosensing, bridging the gap between foundational research and practical biomedical and sensing applications. Our innovative methodologies demonstrate the transformative potential of combining advanced imaging techniques, deep learning, and material science to address complex challenges in these domains.

To address the critical challenge of AVG in OCTA, we developed a dual-beam OCT system that effectively decouples AVG contributions to decorrelation signals. By carefully selecting the spot sizes of the dual beams, our approach demonstrated significant improvements in measurement precision and reliability. Validation through phantom experiments and in-vivo imaging of skin vasculature revealed a substantial reduction in AVG-induced artifacts, enhancing the accuracy of blood flow velocimetry and providing valuable insights for clinical OCTA applications.

We also introduced a self-supervised deep learning framework to achieve super-resolution in OCT imaging, independent of AVG decoupling. By training directly on spectral fringe data, this method preserved both magnitude and phase information, resulting in substantial improvements in image quality. Key metrics such as PSNR and SSIM were significantly enhanced, speckle size was reduced, and fine structural details—particularly in challenging regions like the stratum corneum and stratum lucidum—were recovered. These advancements underscore the potential of spectrum-based training to refine OCT imaging, enabling more precise, non-invasive diagnostics across fields such as dermatology, ophthalmology, and neuro-ophthalmology.

Extending the scope of our work to biosensing, we developed a hybrid OCT -patch system that integrates structural and biochemical sensing capabilities. This platform utilized the sensitivity of LC droplets embedded in the patch to environmental changes, enabling accurate biochemical information, e.g. pH, detection through droplet size calibration. Notably, this system demonstrated the capability to measure droplets even below OCT's axial resolution limit, showcasing its exceptional sensitivity. Beyond pH sensing, the platform's versatility extends to detecting refractive index changes due to glucose, proteins, ions, and electric fields,

highlighting its potential for wearable, real-time biochemical monitoring.

The novel integration of these advancements is particularly significant for skin diagnostics, providing high-resolution, non-invasive methods for visualizing and quantifying skin structures and detecting subtle biochemical changes. These methods hold immense promise for improving early detection, monitoring, and treatment of dermatological conditions while extending their utility to other biomedical and engineering challenges. By addressing long-standing limitations in OCT imaging and biosensing, this thesis lays a robust foundation for transformative applications in biomedical imaging, material science, and interdisciplinary innovation.

6.2 Future Work

The advancements presented in this thesis open new avenues for further exploration and development across multiple domains. Each of the contributions has significant potential to be expanded and refined for broader applications.

For the dual-beam OCT system, future work could focus on extending its application to retinal imaging, where accurate blood flow measurements and velocity gradient decoupling are critical for diagnosing and managing retinal vascular diseases. By optimizing the dual-beam setup for ocular use, such as adapting the system for smaller field-of-view requirements and higher sensitivity, this method could enable precise blood flow analysis in delicate retinal vessels. This advancement would be instrumental in improving the understanding and treatment of conditions like diabetic retinopathy and age-related macular degeneration, where vascular abnormalities play a key role. In addition to applying this method to retinal imaging, future work may focus on optimizing flow measurement algorithms that account for varying vessel angles, developing automatic segmentation of vessel layers, and integrating the dual-beam system with multimodal ophthalmic imaging tools. Hardware miniaturization and motion-robust scanning strategies may also be pursued to facilitate clinical integration.

The super-resolution framework, leveraging spectral fringe data for training, also holds great promise for retinal applications. Enhancing axial resolution in retinal imaging could reveal microstructural details critical for diagnosing early-stage diseases, such as glaucoma and macular degeneration. Integrating this deep learning-based approach with real-time imaging workflows could provide ophthalmologists with unprecedented diagnostic precision while maintaining the non-invasive nature of OCT imaging. Future research could explore iterative

training methods and hardware acceleration to enable real-time super-resolution imaging in clinical settings. To move beyond axial enhancement in static B-scans, the framework may be expanded to include temporal stability in dynamic OCTA volumes and learning from multi-contrast inputs (e.g., structural + flow). Domain adaptation techniques can be explored to enable generalizability across different tissue types or OCT systems, while maintaining real-time capability through lightweight, deployable model designs.

For the OCT-patch biosensing platform, future work could expand beyond pH sensing to detect a broader range of biochemical and environmental factors. By tailoring LC droplet compositions and hydrogel properties, the platform could be adapted for detecting glucose, proteins, metal ions, or even environmental toxins. Innovations in LC material science, combined with the precision of OCT imaging, could further enhance the system's sensitivity and specificity. Additionally, developing wearable or implantable biosensing devices based on this platform could enable continuous, real-time monitoring for personalized medicine, with applications ranging from diabetes management to wound healing and inflammation tracking. Future iterations could incorporate multiple LC droplet types patterned within one patch to enable multi-analyte detection. Research may also explore integrating optical filters or polarization-resolved OCT to enhance readout specificity. Developing strategies to correct for environmental variations—such as temperature compensation models—will be important to improve reliability in real-world applications. Ultimately, creating a soft, biocompatible wearable platform with wireless data transmission would position the system for personalized medicine and chronic disease monitoring.

Together, these future directions represent exciting opportunities to enhance the utility and impact of OCT imaging and biosensing, contributing to advances in ophthalmology, dermatology, personalized medicine, and environmental sensing. By continuing to bridge innovative methodologies with practical applications, this work has the potential to transform diagnostics and monitoring across a variety of critical fields.

Author's Publications

Journal Articles:

- Manuscript revision in progress: " Liquid Crystal Droplet Patch for Skin PH Sensing by Optical Coherence Tomography," with the intention to submit to ACS Nano. (**Zhengyang Xu**, Guocheng Fang, Ningyuan Nie, Xi Chen, Kan Lin, Yu-Cheng Chen)
- **Zhengyang Xu**, Yuting Gao, Xi Chen, Kan Lin, Linbo Liu, and Yu-Cheng Chen, "Axial Super-Resolution in Optical Coherence Tomography Images via Spectrum-Based Self-Supervised Training," *IEEE Trans. Comput. Imaging*, vol. 11, pp. 497–505, 2025, doi: 10.1109/tci.2025.3555134.
- **Zhengyang Xu**, Yukun Wang, Xi Chen, Kan Lin, and Linbo Liu, "Dual beam optical coherence tomography angiography for decoupling axial velocity gradient," Sci Rep, vol. 14, no. 1, p. 19464, Aug. 2024, doi: 10.1038/s41598-024-68924-4.
- Manuscript revision in progress: " High-Speed Spectrally Encoded Optical Coherence Tomography Angiography Enabled by Deep Learning," with the intention to submit to IEEE Transactions on Image Processing. (**Zhengyang Xu,** Po-Hao Tseng, Yuting Gao, Yukun Wang, Xi Chen, Kan Lin, Linbo Liu, Yu-Cheng Chen*)
- Yukun Wang, Si Chen, Kan Lin, Xi Chen, **Zhengyang Xu**, Shiliang Lou, Xin Ge, Guangming Ni, Xiaojun Yu, Jianhua Mo, Quanquan Mu, Linbo Liu, "Multi-channel spectral-domain optical coherence tomography using single spectrometer," Chin. Opt. Lett., vol. 21, no. 5, p. 051102, 2023, doi: 10.3788/COL202321.051102.
- Yukun Wang, Si Chen, Xi Chen, **Zhengyang Xu**, Kan Lin, Linlin Shi, Quanquan Mu, Linbo Liu, "Coaxial Bright and Dark Field Optical Coherence Tomography," IEEE Trans. Biomed. Eng., 2024, doi: 10.1109/TBME.2024.3355174.

Conference Proceedings

- **Zhengyang Xu**, Yukun Wang, Xi Chen, Kan Lin, and Linbo Liu, “Dual-resolution axial velocity gradient elimination,” in Dynamics and Fluctuations in Biomedical Photonics XXI, SPIE, Mar. 2024, p. PC128410N. doi: 10.1117/12.3005210.

Bibliography

[1] L. An and R. K. Wang, "In vivo volumetric imaging of vascular perfusion within human retina and choroids with optical micro-angiography," *Opt. Express*, vol. 16, no. 15, p. 11438, July 2008, doi: 10.1364/OE.16.011438.

[2] R. F. Spaide, J. G. Fujimoto, N. K. Waheed, S. R. Sadda, and G. Staurenghi, "Optical coherence tomography angiography," *Prog. Retin. Eye Res.*, vol. 64, pp. 1–55, May 2018, doi: 10.1016/j.preteyeres.2017.11.003.

[3] Y. Jia *et al.*, "Split-spectrum amplitude-decorrelation angiography with optical coherence tomography," *Opt. Express*, vol. 20, no. 4, p. 4710, Feb. 2012, doi: 10.1364/OE.20.004710.

[4] J. G. Fujimoto, C. Pitris, S. A. Boppart, and M. E. Brezinski, "Optical Coherence Tomography: An Emerging Technology for Biomedical Imaging and Optical Biopsy," *Neoplasia N. Y. N*, vol. 2, no. 1–2, pp. 9–25, Jan. 2000.

[5] W. Drexler and J. G. Fujimoto, Eds., *Optical coherence tomography: technology and applications*. in Biological and medical physics, biomedical engineering. Berlin: Springer, 2008.

[6] R. Leitgeb, C. Hitzenberger, and A. Fercher, "Performance of fourier domain vs time domain optical coherence tomography," *Opt. Express*, vol. 11, no. 8, p. 889, Apr. 2003, doi: 10.1364/OE.11.000889.

[7] M. Wojtkowski, R. Leitgeb, A. Kowalczyk, T. Bajraszewski, and A. F. Fercher, "In vivo human retinal imaging by Fourier domain optical coherence tomography," *J. Biomed. Opt.*, vol. 7, no. 3, pp. 457–463, July 2002, doi: 10.1117/1.1482379.

[8] J. F. de Boer, B. Cense, B. H. Park, M. C. Pierce, G. J. Tearney, and B. E. Bouma, "Improved signal-to-noise ratio in spectral-domain compared with time-domain optical coherence tomography," *Opt. Lett.*, vol. 28, no. 21, pp. 2067–2069, Nov. 2003, doi: 10.1364/OL.28.002067.

[9] B. E. Kim and D. Y. Leung, "Significance of Skin Barrier Dysfunction in Atopic Dermatitis," *Allergy Asthma Immunol. Res.*, vol. 10, no. 3, p. 207, Jan. 2018, doi: 10.4168/aair.2018.10.3.207.

[10] H. Hashizume, "Skin Aging and Dry Skin," *J. Dermatol.*, vol. 31, no. 8, pp. 603–609, Aug. 2004, doi: 10.1111/j.1346-8138.2004.tb00565.x.

[11] J. van Smeden and J. A. Bouwstra, "Stratum Corneum Lipids: Their Role for the Skin Barrier Function in Healthy Subjects and Atopic Dermatitis Patients," *Curr. Probl. Dermatol.*, vol. 49, pp. 8–26, 2016, doi: 10.1159/000441540.

[12] V. D. Mandel and M. Ardigò, "Non-Invasive Diagnostic Techniques in Dermatology," *J. Clin. Med.*, vol. 12, no. 3, p. 1081, Jan. 2023, doi: 10.3390/jcm12031081.

[13] M. C. Pierce, J. Strasswimmer, B. H. Park, B. Cense, and J. F. de Boer, "Advances in optical coherence tomography imaging for dermatology," *J. Invest. Dermatol.*, vol. 123, no. 3, pp. 458–463, Sept. 2004, doi: 10.1111/j.0022-202X.2004.23404.x.

[14] "Optical Coherence Tomography/Ophthalmology: OCT angiography: A new approach with 'gold standard' capabilities and more," Laser Focus World. Accessed: July 04, 2024. [Online]. Available: https://www.laserfocusworld.com/detectors-imaging/article/16551488/optical-coherence-tomography-ophthalmology-oct-angiography-a-new-approach-with-gold-standard-capabilities-and-more

[15] J. A. Izatt, M. D. Kulkarni, S. Yazdanfar, J. K. Barton, and A. J. Welch, "In vivo bidirectional color Doppler flow imaging of picoliter blood volumes using optical coherence tomography," *Opt. Lett.*, vol. 22, no. 18, p. 1439, Sept. 1997, doi: 10.1364/OL.22.001439.

[16] Z. Chen *et al.*, “Noninvasive imaging of in vivo blood flow velocity using optical Doppler tomography,” *Opt. Lett. Vol 22 Issue 14 Pp 1119-1121*, July 1997, doi: 10.1364/OL.22.001119.
[17] R. K. Wang and S. Hurst, “Mapping of cerebro-vascular blood perfusion in mice with skin and skull intact by Optical Micro-AngioGraphy at 1.3μm wavelength,” *Opt. Express Vol 15 Issue 18 Pp 11402-11412*, Sept. 2007, doi: 10.1364/OE.15.011402.
[18] W. J. Choi *et al.*, “Characterizing relationship between optical microangiography signals and capillary flow using microfluidic channels,” *Biomed. Opt. Express*, vol. 7, no. 7, p. 2709, July 2016, doi: 10.1364/BOE.7.002709.
[19] J. Xu, S. Song, Y. Li, and R. K. Wang, “Complex-based OCT angiography algorithm recovers microvascular information better than amplitude- or phase-based algorithms in phase-stable systems,” *Phys. Med. Biol.*, vol. 63, no. 1, p. 015023, Dec. 2017, doi: 10.1088/1361-6560/aa94bc.
[20] T. Schmoll, H. Bagherinia, and H. Ren, “OCTA flow signal enhancement by reducing residual structural signal,” p. 1.
[21] E. Moult *et al.*, “Ultrahigh-Speed Swept-Source OCT Angiography in Exudative AMD,” *Ophthalmic Surg. Lasers Imaging Retina*, vol. 45, no. 6, pp. 496–505, 2014, doi: 10.3928/23258160-20141118-03.
[22] W. Choi *et al.*, “Choriocapillaris and Choroidal Microvasculature Imaging with Ultrahigh Speed OCT Angiography,” *PLOS ONE*, vol. 8, no. 12, p. e81499, Dec. 2013, doi: 10.1371/journal.pone.0081499.
[23] I. Grulkowski *et al.*, “Retinal, anterior segment and full eye imaging using ultrahigh speed swept source OCT with vertical-cavity surface emitting lasers,” *Biomed. Opt. Express*, vol. 3, no. 11, pp. 2733–2751, Nov. 2012, doi: 10.1364/BOE.3.002733.
[24] R. F. Spaide, “Optical Coherence Tomography Angiography Signs of Vascular Abnormalization With Antiangiogenic Therapy for Choroidal Neovascularization,” *Am. J. Ophthalmol.*, vol. 160, no. 1, pp. 6–16, July 2015, doi: 10.1016/j.ajo.2015.04.012.
[25] K. Ghasemi Falavarjani, M. Al-Sheikh, H. Akil, and S. R. Sadda, “Image artefacts in swept-source optical coherence tomography angiography,” *Br. J. Ophthalmol.*, vol. 101, no. 5, pp. 564–568, May 2017, doi: 10.1136/bjophthalmol-2016-309104.
[26] E. D. Cole *et al.*, “The Definition, Rationale, and Effects of Thresholding in OCT Angiography,” *Ophthalmol. Retina*, vol. 1, no. 5, pp. 435–447, 2017, doi: 10.1016/j.oret.2017.01.019.
[27] A. Sellam, F. Coscas, A. Glacet-Bernard, A. Miere, G. J. Coscas, and E. H. Souied, “Qualitative and quantitative follow-up of patients with retinal vein occlusion using Optical Coherence Tomography Angiography,” *Invest. Ophthalmol. Vis. Sci.*, vol. 57, no. 12, pp. 5474–5474, Sept. 2016.
[28] J. Tokayer, Y. Jia, A.-H. Dhalla, and D. Huang, “Blood flow velocity quantification using split-spectrum amplitude-decorrelation angiography with optical coherence tomography,” *Biomed. Opt. Express*, vol. 4, no. 10, p. 1909, Oct. 2013, doi: 10.1364/BOE.4.001909.
[29] J. P. Su *et al.*, “Calibration of optical coherence tomography angiography with a microfluidic chip,” *J. Biomed. Opt.*, vol. 21, no. 08, p. 1, Aug. 2016, doi: 10.1117/1.JBO.21.8.086015.
[30] J. Yang *et al.*, “Hematocrit dependence of flow signal in optical coherence tomography angiography,” *Biomed. Opt. Express*, vol. 8, no. 2, p. 776, Feb. 2017, doi: 10.1364/BOE.8.000776.
[31] X. Wei, T. T. Hormel, S. Pi, Y. Guo, Y. Jian, and Y. Jia, “High dynamic range optical coherence tomography angiography (HDR-OCTA),” *Biomed. Opt. Express*, vol. 10, no. 7, p. 3560, July 2019, doi: 10.1364/BOE.10.003560.

[32] J. Lee, W. Wu, J. Y. Jiang, B. Zhu, and D. A. Boas, “Dynamic light scattering optical coherence tomography,” p. 16, 2012.
[33] B. K. Huang and M. A. Choma, “Resolving directional ambiguity in dynamic light scattering-based transverse motion velocimetry in optical coherence tomography,” *Opt. Lett.*, vol. 39, no. 3, p. 521, Feb. 2014, doi: 10.1364/OL.39.000521.
[34]S. Chen *et al.*, “Spectrally extended line field optical coherence tomography angiography,” *Opto-Electron. Adv.*, vol. 8, no. 5, pp. 240293–240293, 2025, doi: 10.29026/oea.2025.240293.
[35] Y. LeCun, Y. Bengio, and G. Hinton, “Deep learning,” *Nature*, vol. 521, no. 7553, pp. 436–444, May 2015, doi: 10.1038/nature14539.
[36] I. Goodfellow, Y. Bengio, and A. Courville, *Deep learning*. in Adaptive computation and machine learning. Cambridge, Massachusetts: The MIT Press, 2016.
[37] B. Dipert, “Using Convolutional Neural Networks for Image Recognition,” Edge AI and Vision Alliance. Accessed: Aug. 05, 2024. [Online]. Available: https://www.edge-ai-vision.com/2015/11/using-convolutional-neural-networks-for-image-recognition/
[38] D. Liu, “A Practical Guide to ReLU,” Medium. Accessed: Aug. 05, 2024. [Online]. Available: https://medium.com/@danqing/a-practical-guide-to-relu-b83ca804f1f7
[39] A. Krizhevsky, I. Sutskever, and G. E. Hinton, “ImageNet classification with deep convolutional neural networks,” *Commun. ACM*, vol. 60, no. 6, pp. 84–90, May 2017, doi: 10.1145/3065386.
[40] Y. Lecun, L. Bottou, Y. Bengio, and P. Haffner, “Gradient-based learning applied to document recognition,” *Proc. IEEE*, vol. 86, no. 11, pp. 2278–2324, Nov. 1998, doi: 10.1109/5.726791.
[41] K. N. Haque, “What is Convolutional Neural Network — CNN (Deep Learning),” Medium. Accessed: July 14, 2025. [Online]. Available: https://nafizshahriar.medium.com/what-is-convolutional-neural-network-cnn-deep-learning-b3921bdd82d5
[42] “Feedforward vs Backpropagation ANN.” Accessed: Aug. 05, 2024. [Online]. Available: https://www.linkedin.com/pulse/feedforward-vs-backpropagation-ann-saffronedge1
[43] H. Wang *et al.*, “Deep learning enables cross-modality super-resolution in fluorescence microscopy,” *Nat. Methods*, vol. 16, no. 1, pp. 103–110, Jan. 2019, doi: 10.1038/s41592-018-0239-0.
[44] I. J. Goodfellow *et al.*, “Generative adversarial nets,” in *Proceedings of the 27th International Conference on Neural Information Processing Systems - Volume 2*, in NIPS’14. Cambridge, MA, USA: MIT Press, Dec. 2014, pp. 2672–2680.
[45] “Overview of GAN Structure | Machine Learning,” Google for Developers. Accessed: July 14, 2025. [Online]. Available: https://developers.google.com/machine-learning/gan/gan_structure
[46] Y. Li, B. Sixou, and F. Peyrin, “A Review of the Deep Learning Methods for Medical Images Super Resolution Problems,” *IRBM*, vol. 42, no. 2, pp. 120–133, Apr. 2021, doi: 10.1016/j.irbm.2020.08.004.
[47] K. de Haan, Z. S. Ballard, Y. Rivenson, Y. Wu, and A. Ozcan, “Resolution enhancement in scanning electron microscopy using deep learning,” *Sci. Rep.*, vol. 9, no. 1, p. 12050, Aug. 2019, doi: 10.1038/s41598-019-48444-2.
[48] X. Wang *et al.*, “ESRGAN: Enhanced Super-Resolution Generative Adversarial Networks,” Sept. 17, 2018, *arXiv*: arXiv:1809.00219. doi: 10.48550/arXiv.1809.00219.
[49] Y. Huang *et al.*, “Simultaneous denoising and super-resolution of optical coherence tomography images based on generative adversarial network,” *Opt. Express*, vol. 27, no. 9, p. 12289, Apr. 2019, doi: 10.1364/OE.27.012289.

[50] Z. Yuan, D. Yang, Z. Yang, J. Zhao, and Y. Liang, "Digital refocusing based on deep learning in optical coherence tomography," *Biomed. Opt. Express*, vol. 13, no. 5, p. 3005, May 2022, doi: 10.1364/BOE.453326.
[51] Z. Yuan, D. Yang, H. Pan, and Y. Liang, "Axial Super-Resolution Study for Optical Coherence Tomography Images Via Deep Learning," *IEEE Access*, vol. 8, pp. 204941–204950, 2020, doi: 10.1109/ACCESS.2020.3036837.
[52] Y. Ling, Z. Dong, X. Li, Y. Gan, and Y. Su, "Deep learning empowered highly compressive SS-OCT via learnable spectral–spatial sub-sampling," *Opt. Lett.*, vol. 48, no. 7, p. 1910, Apr. 2023, doi: 10.1364/OL.484500.
[53] T. T. Yu, D. Ma, J. Cole, M. Jin Ju, M. Faisal Beg, and M. V. Sarunic, "Spectral Bandwidth Recovery of Optical Coherence Tomography Images using Deep Learning," in *2021 12th International Symposium on Image and Signal Processing and Analysis (ISPA)*, Zagreb, Croatia: IEEE, Sept. 2021, pp. 67–71. doi: 10.1109/ISPA52656.2021.9552122.
[54] Z. Yuan, D. Yang, W. Wang, J. Zhao, and Y. Liang, "Self super-resolution of optical coherence tomography images based on deep learning," *Opt. Express*, vol. 31, no. 17, pp. 27566–27581, Aug. 2023, doi: 10.1364/OE.495530.
[55] L. Guo *et al.*, "Portable Photoacoustic Analytical System Combined with Wearable Hydrogel Patch for pH Monitoring in Chronic Wounds," *Anal. Chem.*, vol. 96, no. 28, pp. 11595–11602, July 2024, doi: 10.1021/acs.analchem.4c02472.
[56] Z. Wang, T. Xu, A. Noel, Y.-C. Chen, and T. Liu, "Applications of liquid crystals in biosensing," *Soft Matter*, vol. 17, no. 18, pp. 4675–4702, 2021, doi: 10.1039/D0SM02088E.
[57] Z. Wang *et al.*, "Bio-electrostatic sensitive droplet lasers for molecular detection," *Nanoscale Adv.*, vol. 2, no. 7, pp. 2713–2719, 2020, doi: 10.1039/D0NA00107D.
[58] J.-H. Jang and S.-Y. Park, "pH-responsive cholesteric liquid crystal double emulsion droplets prepared by microfluidics," *Sens. Actuators B Chem.*, vol. 241, pp. 636–643, Mar. 2017, doi: 10.1016/j.snb.2016.10.118.
[59] J. Kim, M. Khan, and S.-Y. Park, "Glucose Sensor using Liquid-Crystal Droplets Made by Microfluidics," *ACS Appl. Mater. Interfaces*, vol. 5, no. 24, pp. 13135–13139, Dec. 2013, doi: 10.1021/am404174n.
[60] L. Zhou, Q. Kang, O. Hu, and L. Yu, "Ultrasensitive detection of glutathione based on liquid crystals in the presence of γ-glutamyl transpeptidase," *Anal. Chim. Acta*, vol. 1040, pp. 187–195, Dec. 2018, doi: 10.1016/j.aca.2018.08.029.
[61] G.-R. Han and C.-H. Jang, "Liquid crystal sensor for the detection of acetylcholine using acetylcholinesterase immobilized on a nanostructured polymeric surface," *Colloid Polym. Sci.*, vol. 293, no. 10, pp. 2771–2779, Oct. 2015, doi: 10.1007/s00396-015-3648-y.
[62] N. ul Amin, H. M. Siddiqi, Y. Kun Lin, Z. Hussain, and N. Majeed, "Bovine Serum Albumin Protein-Based Liquid Crystal Biosensors for Optical Detection of Toxic Heavy Metals in Water," *Sensors*, vol. 20, no. 1, Art. no. 1, Jan. 2020, doi: 10.3390/s20010298.
[63] A. Capocefalo, E. Quintiero, C. Conti, N. Ghofraniha, and I. Viola, "Droplet Lasers for Smart Photonic Labels," *ACS Appl. Mater. Interfaces*, vol. 13, no. 43, pp. 51485–51494, Nov. 2021, doi: 10.1021/acsami.1c14972.
[64] S. Xu, Y. Li, Y. Liu, J. Sun, H. Ren, and S.-T. Wu, "Fast-Response Liquid Crystal Microlens," *Micromachines*, vol. 5, no. 2, Art. no. 2, June 2014, doi: 10.3390/mi5020300.
[65] "OCT-Based Velocimetry for Blood Flow Quantification," in *High Resolution Imaging in Microscopy and Ophthalmology*, Cham: Springer International Publishing, 2019, pp. 161–179. doi: 10.1007/978-3-030-16638-0_7.

[66] N. Uribe-Patarroyo and B. E. Bouma, “Velocity gradients in spatially resolved laser Doppler flowmetry and dynamic light scattering with confocal and coherence gating,” *Phys. Rev. E*, vol. 94, no. 2, p. 022604, Aug. 2016, doi: 10.1103/PhysRevE.94.022604.
[67] R. Maltais-Tariant, M. Dehaes, and C. Boudoux, “Exact measurement of transverse flow velocity using few-mode optical coherence tomography,” in *Optical Coherence Tomography and Coherence Domain Optical Methods in Biomedicine XXVII*, SPIE, Mar. 2023, p. PC123670G. doi: 10.1117/12.2652633.
[68] M. Wan *et al.*, “Dual-beam delay-encoded all fiber Doppler optical coherence tomography for *in vivo* measurement of retinal blood flow,” *Chin. Opt. Lett.*, vol. 20, no. 1, Art. no. 1, Jan. 2022, doi: 10.3788/COL202220.011701.
[69] Y. Kim, N. Lippok, and B. J. Vakoc, “Multi-beam OCT imaging based on an integrated, free-space interferometer,” *Biomed. Opt. Express*, vol. 12, no. 1, pp. 100–109, Jan. 2021, doi: 10.1364/BOE.408703.
[70] Y. Wang *et al.*, “Multi-channel spectral-domain optical coherence tomography using single spectrometer,” *Chin. Opt. Lett.*, vol. 21, no. 5, p. 051102, 2023, doi: 10.3788/COL202321.051102.
[71] T. Lister, P. A. Wright, and P. H. Chappell, “Optical properties of human skin,” *J. Biomed. Opt.*, vol. 17, no. 9, p. 090901, Sept. 2012, doi: 10.1117/1.JBO.17.9.090901.
[72] X. Liu *et al.*, “Cmos Image Sensors Dynamic Range and Snr Enhancement via Statistical Signal Processing,” Accessed: June 08, 2024. [Online]. Available: https://www.semanticscholar.org/paper/Cmos-Image-Sensors-Dynamic-Range-and-Snr-via-Signal-Liu-Horowitz/3695505307a0b8fd21f4a8fd6d4384662d25b12b
[73] “IEC 60825-1:2014 | IEC Webstore.” Accessed: Apr. 17, 2023. [Online]. Available: https://webstore.iec.ch/publication/3587
[74] A. S. Nam, B. Braaf, and B. J. Vakoc, “Using the dynamic forward scattering signal for optical coherence tomography based blood flow quantification,” *Opt. Lett.*, vol. 47, no. 12, p. 3083, June 2022, doi: 10.1364/OL.455475.
[75] S. H. Yun, G. J. Tearney, J. F. de Boer, and B. E. Bouma, “Motion artifacts in optical coherence tomography with frequency-domain ranging,” *Opt. Express*, vol. 12, no. 13, pp. 2977–2998, June 2004.
[76] C. Dai, X. Liu, H. F. Zhang, C. A. Puliafito, and S. Jiao, “Absolute Retinal Blood Flow Measurement With a Dual-Beam Doppler Optical Coherence Tomography,” *Investig. Opthalmology Vis. Sci.*, vol. 54, no. 13, p. 7998, Dec. 2013, doi: 10.1167/iovs.13-12318.
[77] T.-W. Kim *et al.*, “Imaging of the Lamina Cribrosa in Glaucoma: Perspectives of Pathogenesis and Clinical Applications,” *Curr. Eye Res.*, vol. 38, no. 9, pp. 903–909, Sept. 2013, doi: 10.3109/02713683.2013.800888.
[78] M. J. Girard, N. G. Strouthidis, C. R. Ethier, and J. M. Mari, “Shadow removal and contrast enhancement in optical coherence tomography images of the human optic nerve head,” *Invest. Ophthalmol. Vis. Sci.*, vol. 52, no. 10, pp. 7738–7748, 2011.
[79] J. S. Kim *et al.*, “Retinal nerve fibre layer thickness measurement reproducibility improved with spectral domain optical coherence tomography,” *Br. J. Ophthalmol.*, vol. 93, no. 8, pp. 1057–1063, Aug. 2009, doi: 10.1136/bjo.2009.157875.
[80] M. F. Kraus *et al.*, “Motion correction in optical coherence tomography volumes on a per A-scan basis using orthogonal scan patterns,” *Biomed. Opt. Express*, vol. 3, no. 6, pp. 1182–1199, 2012.
[81] J. Cheng, J. A. Lee, G. Xu, Y. Quan, E. P. Ong, and D. W. Kee Wong, “Motion Correction in Optical Coherence Tomography for Multi-modality Retinal Image Registration,” in *Proceedings of the Ophthalmic Medical Image Analysis Third International Workshop*, Athens, Greece: University of Iowa, Oct. 2016, pp. 65–72. doi: 10.17077/omia.1048.

[82] M. Choma, M. Sarunic, C. Yang, and J. Izatt, “Sensitivity advantage of swept source and Fourier domain optical coherence tomography,” *Opt. Express*, vol. 11, no. 18, p. 2183, Sept. 2003, doi: 10.1364/oe.11.002183.
[83] R. K. Wang, L. An, P. Francis, and D. J. Wilson, “Depth-resolved imaging of capillary networks in retina and choroid using ultrahigh sensitive optical microangiography,” *Opt. Lett.*, vol. 35, no. 9, p. 1467, May 2010, doi: 10.1364/ol.35.001467.
[84] M. P. de Sivry-Houle, S. B. Beaudoin, S. Brais-Brunet, M. Dehaes, N. Godbout, and C. Boudoux, “All-fiber few-mode optical coherence tomography using a modally-specific photonic lantern,” *Biomed. Opt. Express*, vol. 12, no. 9, pp. 5704–5719, Aug. 2021, doi: 10.1364/BOE.428101.
[85] abbas habibi, M. Emamverdi, maryam ashrafkhorasani, M. Gupta Nittala, and S. R. Sadda, “Reflectivity of the Retinal Pigment Epithelium in Aging and Early Age-Related Macular Degeneration.,” *Invest. Ophthalmol. Vis. Sci.*, vol. 64, no. 8, p. 2143, June 2023.
[86] J. Liao, S. Yang, T. Zhang, C. Li, and Z. Huang, “Fast optical coherence tomography angiography image acquisition and reconstruction pipeline for skin application,” *Biomed. Opt. Express*, vol. 14, no. 8, p. 3899, Aug. 2023, doi: 10.1364/BOE.486933.
[87] L. Liu *et al.*, “Imaging the subcellular structure of human coronary atherosclerosis using micro–optical coherence tomography,” *Nat. Med.*, vol. 17, no. 8, pp. 1010–1014, Aug. 2011, doi: 10.1038/nm.2409.
[88] W. Drexler, U. Morgner, R. K. Ghanta, F. X. Kärtner, J. S. Schuman, and J. G. Fujimoto, “Ultrahigh-resolution ophthalmic optical coherence tomography,” *Nat. Med.*, vol. 7, no. 4, pp. 502–507, Apr. 2001, doi: 10.1038/86589.
[89] R. M. Werkmeister *et al.*, “Ultrahigh-resolution OCT imaging of the human cornea,” *Biomed. Opt. Express*, vol. 8, no. 2, pp. 1221–1239, Jan. 2017, doi: 10.1364/BOE.8.001221.
[90] B. Povazay *et al.*, “Visible light optical coherence tomography,” in *Coherence Domain Optical Methods in Biomedical Science and Clinical Applications VI*, SPIE, June 2002, pp. 90–94. doi: 10.1117/12.470466.
[91] X. Shu, L. J. Beckmann, and H. F. Zhang, “Visible-light optical coherence tomography: a review,” *J. Biomed. Opt.*, vol. 22, no. 12, p. 121707, Dec. 2017, doi: 10.1117/1.JBO.22.12.121707.
[92] S. P. Chong, M. Bernucci, H. Radhakrishnan, and V. J. Srinivasan, “Structural and functional human retinal imaging with a fiber-based visible light OCT ophthalmoscope,” *Biomed. Opt. Express*, vol. 8, no. 1, pp. 323–337, Jan. 2017, doi: 10.1364/BOE.8.000323.
[93] S. Pi *et al.*, “Angiographic and structural imaging using high axial resolution fiber-based visible-light OCT,” *Biomed. Opt. Express*, vol. 8, no. 10, pp. 4595–4608, Sept. 2017, doi: 10.1364/BOE.8.004595.
[94] L. Yue, H. Shen, J. Li, Q. Yuan, H. Zhang, and L. Zhang, “Image super-resolution: The techniques, applications, and future,” *Signal Process.*, vol. 128, pp. 389–408, Nov. 2016, doi: 10.1016/j.sigpro.2016.05.002.
[95] Y. Rivenson, Z. Göröcs, H. Günaydin, Y. Zhang, H. Wang, and A. Ozcan, “Deep learning microscopy,” *Optica*, vol. 4, no. 11, pp. 1437–1443, Nov. 2017, doi: 10.1364/OPTICA.4.001437.
[96] X. Yu *et al.*, “Self-supervised Blind2Unblind deep learning scheme for OCT speckle reductions,” *Biomed. Opt. Express*, vol. 14, no. 6, p. 2773, June 2023, doi: 10.1364/BOE.481870.
[97] X. Yu, C. Ge, M. Li, M. Z. Aziz, J. Mo, and Z. Fan, “Multiscale denoising generative adversarial network for speckle reduction in optical coherence tomography images,” *J. Med. Imaging*, vol. 10, no. 2, p. 024006, Mar. 2023, doi: 10.1117/1.JMI.10.2.024006.

[98] X. Yu, M. Li, C. Ge, P. P. Shum, J. Chen, and L. Liu, "A generative adversarial network with multi-scale convolution and dilated convolution res-network for OCT retinal image despeckling," *Biomed. Signal Process. Control*, vol. 80, p. 104231, Feb. 2023, doi: 10.1016/j.bspc.2022.104231.
[99] X. Yu *et al.*, "CGNet-assisted Automatic Vessel Segmentation for Optical Coherence Tomography Angiography," *J. Biophotonics*, vol. 15, no. 10, p. e202200067, Oct. 2022, doi: 10.1002/jbio.202200067.
[100] B. Qiu *et al.*, "N2NSR-OCT : Simultaneous denoising and super-resolution in optical coherence tomography images using semisupervised deep learning," *J. Biophotonics*, vol. 14, no. 1, p. e202000282, Jan. 2021, doi: 10.1002/jbio.202000282.
[101] K. Liang *et al.*, "Resolution enhancement and realistic speckle recovery with generative adversarial modeling of micro-optical coherence tomography," *Biomed. Opt. Express*, vol. 11, no. 12, p. 7236, Dec. 2020, doi: 10.1364/BOE.402847.
[102] W. Lee, H. S. Nam, J. Y. Seok, W.-Y. Oh, J. W. Kim, and H. Yoo, "Deep learning-based image enhancement in optical coherence tomography by exploiting interference fringe," *Commun. Biol.*, vol. 6, no. 1, p. 464, Apr. 2023, doi: 10.1038/s42003-023-04846-7.
[103] Y. Zhang *et al.*, "Neural network-based image reconstruction in swept-source optical coherence tomography using undersampled spectral data," *Light Sci. Appl.*, vol. 10, no. 1, p. 155, July 2021, doi: 10.1038/s41377-021-00594-7.
[104] M. Abdel-Basset, N. Moustafa, and H. Hawash, *Deep Learning Approaches for Security Threats in IoT Environments*, 1st ed. Wiley, 2022. doi: 10.1002/9781119884170.
[105] R. Zhang, P. Isola, A. A. Efros, E. Shechtman, and O. Wang, "The Unreasonable Effectiveness of Deep Features as a Perceptual Metric," in *2018 IEEE/CVF Conference on Computer Vision and Pattern Recognition*, Salt Lake City, UT: IEEE, June 2018, pp. 586–595. doi: 10.1109/CVPR.2018.00068.
[106] D. Ramos, J. Franco-Pedroso, A. Lozano-Diez, and J. Gonzalez-Rodriguez, "Deconstructing Cross-Entropy for Probabilistic Binary Classifiers," *Entropy*, vol. 20, no. 3, Art. no. 3, Mar. 2018, doi: 10.3390/e20030208.
[107] *Safety of laser products / Part 1, Equipment classification and requirements = Sécurité des appareils lasers. Partie 1 = Classification des matériels et exigences / IEC Commission Electronique Internationale*, Edition 3.0, 2014-05. Geneva: IEC, 2014.
[108] K. Simonyan and A. Zisserman, "Very Deep Convolutional Networks for Large-Scale Image Recognition," Apr. 10, 2015, *arXiv*: arXiv:1409.1556. Accessed: Sept. 27, 2023. [Online]. Available: http://arxiv.org/abs/1409.1556
[109] G. Lamouche, C.-E. Bisaillon, S. Vergnole, and J. P. Monchalin, "On the speckle size in optical coherence tomography," presented at the Biomedical Optics (BiOS) 2008, J. A. Izatt, J. G. Fujimoto, and V. V. Tuchin, Eds., San Jose, CA, Feb. 2008, p. 684724. doi: 10.1117/12.761862.
[110] Y. Piederriere, J. Le Meur, J. Cariou, J. F. Abgrall, and M. T. Blouch, "Particle aggregation monitoring by speckle size measurement; application to blood platelets aggregation," *Opt. Express*, vol. 12, no. 19, p. 4596, 2004, doi: 10.1364/OPEX.12.004596.
[111] B. Považay *et al.*, "Enhanced visualization of choroidal vessels using ultrahigh resolution ophthalmic OCT at 1050 nm," *Opt. Express*, vol. 11, no. 17, pp. 1980–1986, Aug. 2003, doi: 10.1364/OE.11.001980.
[112] R. A. Leitgeb *et al.*, "Ultrahigh resolution Fourier domain optical coherence tomography," *Opt. Express*, vol. 12, no. 10, pp. 2156–2165, May 2004, doi: 10.1364/OPEX.12.002156.
[113] M. Wojtkowski, V. J. Srinivasan, T. H. Ko, J. G. Fujimoto, A. Kowalczyk, and J. S. Duker, "Ultrahigh-resolution, high-speed, Fourier domain optical coherence tomography

and methods for dispersion compensation," *Opt. Express*, vol. 12, no. 11, pp. 2404–2422, May 2004, doi: 10.1364/OPEX.12.002404.
[114] J. Ma, R. Desai, P. Nesper, M. Gill, A. Fawzi, and D. Skondra, "Optical Coherence Tomographic Angiography Imaging in Age-Related Macular Degeneration," *Ophthalmol. Eye Dis.*, vol. 9, p. 1179172116686075, Mar. 2017, doi: 10.1177/1179172116686075.
[115] Y. Zhu *et al.*, "Different Scan Protocols Affect the Detection Rates of Diabetic Retinopathy Lesions by Wide-Field Swept-Source Optical Coherence Tomography Angiography," *Am. J. Ophthalmol.*, vol. 215, pp. 72–80, July 2020, doi: 10.1016/j.ajo.2020.03.004.
[116] Y. Shiga, T. Nishida, J. W. Jeoung, A. Di Polo, and B. Fortune, "Optical coherence tomography and optical coherence tomography angiography: essential tools for detecting glaucoma and disease progression," *Front. Ophthalmol.*, vol. 3, July 2023, doi: 10.3389/fopht.2023.1217125.
[117] J. Ambati and B. J. Fowler, "Mechanisms of Age-Related Macular Degeneration," *Neuron*, vol. 75, no. 1, pp. 26–39, July 2012, doi: 10.1016/j.neuron.2012.06.018.
[118] J. Chua *et al.*, "Optical coherence tomography angiography of the retina and choroid in systemic diseases," *Prog. Retin. Eye Res.*, vol. 103, p. 101292, Nov. 2024, doi: 10.1016/j.preteyeres.2024.101292.
[119] R. N. Weinreb, T. Aung, and F. A. Medeiros, "The Pathophysiology and Treatment of Glaucoma: A Review," *JAMA*, vol. 311, no. 18, p. 1901, May 2014, doi: 10.1001/jama.2014.3192.
[120] Y. Kaizu *et al.*, "Optical Coherence Tomography Angiography Reveals Spatial Bias of Macular Capillary Dropout in Diabetic Retinopathy," *Investig. Opthalmology Vis. Sci.*, vol. 58, no. 11, p. 4889, Oct. 2017, doi: 10.1167/iovs.17-22306.
[121] T. Garcia, G. Bonnay, A. Tourbah, and C. Arndt, "Optical Coherence Tomography in Neuro-Ophthalmology," in *Optical Coherence Tomography*, M. Kawasaki, Ed., InTech, 2013. doi: 10.5772/53510.
[122] J. Britze and J. L. Frederiksen, "Optical coherence tomography in multiple sclerosis," *Eye*, vol. 32, no. 5, p. 884, Feb. 2018, doi: 10.1038/s41433-017-0010-2.
[123] M.-H. Schmid-Wendtner and H. C. Korting, "The pH of the skin surface and its impact on the barrier function," *Skin Pharmacol. Physiol.*, vol. 19, no. 6, pp. 296–302, 2006, doi: 10.1159/000094670.
[124] M. Lukić, I. Pantelić, and S. D. Savić, "Towards Optimal pH of the Skin and Topical Formulations: From the Current State of the Art to Tailored Products," *Cosmetics*, vol. 8, no. 3, Art. no. 3, Sept. 2021, doi: 10.3390/cosmetics8030069.
[125] H.-L. Liang, R. Zentel, P. Rudquist, and J. Lagerwall, "Towards tunable defect arrangements in smectic liquid crystal shells utilizing the nematic–smectic transition in hybrid-aligned geometries," *Soft Matter*, vol. 8, no. 20, pp. 5443–5450, May 2012, doi: 10.1039/C2SM07415J.
[126] J. Li, "Refractive Indices Of Liquid Crystals And Their Applications In Display And Photonic Devices," 2005, [Online]. Available: https://stars.library.ucf.edu/etd/4460
[127] S. Xie *et al.*, "Label-free optical sensor based on liquid crystal sessile droplet array for penicillin G determination," *Colloids Surf. Physicochem. Eng. Asp.*, vol. 644, p. 128728, July 2022, doi: 10.1016/j.colsurfa.2022.128728.
[128] N. Nie and Y.-C. Chen, "Bioadhesive Hydrogel Flexible Laser for Sweat Sensing based on Liquid Crystal Microdroplets".
[129] F. Reyes-Ortega, "3 - pH-responsive polymers: properties, synthesis and applications," in *Smart Polymers and their Applications*, M. R. Aguilar and J. San Román, Eds., Woodhead Publishing, 2014, pp. 45–92. doi: 10.1533/9780857097026.1.45.

[130] D. D. Ebbing and S. D. Gammon, *General chemistry*, 9th ed. Boston, Mass.: Houghton Mifflin Co., 2007.
[131] H. Omidian and S. D. Chowdhury, "Advancements and Applications of Injectable Hydrogel Composites in Biomedical Research and Therapy," *Gels*, vol. 9, no. 7, p. 533, June 2023, doi: 10.3390/gels9070533.
[132] B. Zhou, K. Fan, T. Li, G. Luan, and L. Kong, "A biocompatible hydrogel-coated fiber-optic probe for monitoring pH dynamics in mammalian brains in vivo," *Sens. Actuators B Chem.*, vol. 380, p. 133334, Apr. 2023, doi: 10.1016/j.snb.2023.133334.
[133] E. Proksch, "pH in nature, humans and skin," *J. Dermatol.*, vol. 45, no. 9, pp. 1044–1052, 2018, doi: 10.1111/1346-8138.14489.
[134] N. C. Gomes, E. G. De Campos, and B. S. De Martinis, "Sweat as an Alternative Matrix in Forensic Toxicology," in *Encyclopedia of Forensic Sciences, Third Edition*, Elsevier, 2023, pp. 719–725. doi: 10.1016/B978-0-12-823677-2.00218-X.
[135] M. Hassan Akhtar *et al.*, "Advances in pH Sensing: From Traditional Approaches to Next-Generation Sensors in Biological Contexts," *Chem. Rec.*, vol. 24, no. 7, p. e202300369, 2024, doi: 10.1002/tcr.202300369.
[136] H.-G. Lee, S. Munir, and S.-Y. Park, "Cholesteric Liquid Crystal Droplets for Biosensors," *ACS Appl. Mater. Interfaces*, vol. 8, no. 39, pp. 26407–26417, Oct. 2016, doi: 10.1021/acsami.6b09624.
[137] H. J. Kim and C.-H. Jang, "Liquid crystal-based capillary sensory platform for the detection of bile acids," *Chem. Phys. Lipids*, vol. 204, pp. 10–14, Apr. 2017, doi: 10.1016/j.chemphyslip.2017.02.003.
[138] M. Humar, M. Ravnik, S. Pajk, and I. Muševič, "Electrically tunable liquid crystal optical microresonators," *Nat. Photonics*, vol. 3, no. 10, pp. 595–600, Oct. 2009, doi: 10.1038/nphoton.2009.170.
[139] "Cosmetics pH Meter PCE-PH20P-ICA incl. ISO calibration certificate | PCE Instruments." Accessed: Nov. 21, 2024. [Online]. Available: https://www.pce-instruments.com/english/measuring-instruments/test-meters/ph-meter-ph-tester-pce-instruments-cosmetics-ph-meter-pce-ph20p-ica-incl.-iso-calibration-certificate-det_5856697.htm
[140] "Home," Precision Instruments Manufacturer Singapore | Hanna Instruments. Accessed: Nov. 21, 2024. [Online]. Available: https://hannasingapore.com/
[141] M.-T. I. I. all rights reserved, "pH Meters for Cosmetics." Accessed: Nov. 21, 2024. [Online]. Available: https://www.mt.com/us/en/home/products/Laboratory_Analytics_Browse/pH-meter/pH-meters/cosmetic-ph-meter.html
[142] "Skin-pH-Meter PH 905 | pH-Measurement on Skin and Scalp." Accessed: Nov. 21, 2024. [Online]. Available: https://medelink.ca/research-devices/probes/sub-page-skin-ph-meter-ph905/?utm_source=chatgpt.com
[143] "LAQUA - Skin pH Meter," Delfin Technologies. Accessed: Nov. 21, 2024. [Online]. Available: https://delfintech.com/products/laquaact/
[144] J. R. Rumble, Ed., *CRC handbook of chemistry and physics*, 102nd edition 2021-2022. Boca Raton London New York: CRC Press, 2021.